Nonlinear Circuit Models for EH Applications Including Multiple Scales

Politecnico di Bari

Department of Electrical and Information Engineering
ELECTRICAL AND INFORMATION ENGINEERING
Ph.D. Program
SSD: ING-IND/31– ELECTRICAL ENGINEERING

Final Dissertation

Nonlinear Circuit Models for EH Applications Including Multiple Scales

---

by
Montegiglio Pasquale

Supervisor:

Prof. Giuseppe Acciani

Coordinator of Ph.D. Program:
Prof. Alfredo Grieco

Course n°31, 01/11/2015-31/10/2018

Politecnico
di Bari

Department of Electrical and Information Engineering
ELECTRICAL AND INFORMATION ENGINEERING
Ph.D. Program
SSD: ING-IND/31–ELECTRICAL ENGINEERING

Final Dissertation

Nonlinear Circuit Models for EH Applications Including Multiple Scales

---

by
Montegiglio Pasquale

Referees:

Prof. Vikram Pakrashi

Prof. Stefan Seelecke

Supervisor:

Prof. Giuseppe Acciani

Coordinator of Ph.D Program:

Prof. Alfredo Grieco

firma

Course n°31, 01/11/2015-31/10/2018

Abstract

This thesis focuses on modeling the dynamic behavior of piezoelectric energy harvester devices. Nonlinearities arising from different aspects, such as material and geometrical effects, are taken into account. Classical reduced-order modeling approaches have been enhanced by including effects of ferroelastic and ferroelectric hysteresis and large deformations, yielding to effective circuit representations that allow for an intuitive insight in the energy transduction processes characterizing the considered class of devices. Nonlinearity sources have been assessed in a separate way. A physics-based model has been employed in order to reproduce hysteretic dynamics of PZT crystal domains. This provides an insight on how, through an engineered crystal design, material nonlinearities can be exploited in order to improve generation performances of piezoceramic-based harvesters. Moreover, an effective hybrid computational framework is proposed for modeling geometric nonlinear effects on the response of flexible PVDF-based harvesters under large deformations. The procedure, experimentally validated, significantly reduce the computational effort for nonlinear dynamic multiscale analysis, while preserving a satisfactory accuracy.

Acknowledgements

I would like to express my deep gratitude to my supervisor Professor Dr. Eng. Giuseppe Acciani, for the expert guidance and the gracious encouragement provided during my Ph.D. studies.

I also need to show my gratitude to the external referee Professors Dr. Eng. Vikram Pakrashi, Dr. Eng. Stefan Seelecke and the Committee Members for their relevant role.

A special thanks go to Dr. Eng. Claudio Maruccio for the friendship and the stimulating cooperation established in these years, which I sincerely appreciate. His advice and support have been paramount in preparing this dissertation.

My appreciation also extend to Dr. Eng. Gianluca Rizzello and his lovely wife Eng. Filomena Simone for making exceptional, at both professional and personal levels, my experience at the ZeMA Laboratory - where Professor Seelecke generously hosted me as a visiting research scholar for seven exciting months.

Finally, I wish to thank my family members for the unconditional support and the encouragement provided. I will always be in their debt.

Contents

List of Figures

List of Tables

1

Introduction

1.1 Motivation

In the last decades, miniaturization and increase of device density according to Moore law (2) has driven to a significant reduction of electronics energy consumption. At the same time, energy harvesting from environmental sources has attracted growing attention, leading to technologies and fabrication methods characterized by high energy efficiency (3). Nowadays, the combination of electronics miniaturization and the increase of energy conversion factors make perpetual devices a real perspective, with a huge impact on IoT applications and smart monitoring grids (4). Innovative devices can be fabricated by coupling piezoelectric and semiconducting properties: nanogenerators (5, 6, 7), piezoelectric field effect transistors (5), piezoelectric diodes (8), piezoelectric chemical sensors (9), and piezo-phototronic devices (10, 11). Furthermore, the integration of the mechanical actuation in flexible electronic systems, through micro and nano piezoelectric devices, is a challenging aspect of interfacing human and electronic components, with important applications in bioengineering (12). Beside technical improvements in device performances and fabrication processes, modeling represent a crucial aspect in developing and optimizing the overall system (13). Energy Harvesters (EHs), in fact, must be designed as elements interacting with the ambient energy source. In this perspective, advanced modeling of each component of an EH (input/energy source, generator, processing unit, energy storage, output/DC power) is of major importance (14). Often, Generalized Kirchhoffian Network (GKN) models are employed to assess the dynamical response of this kind of devices (15). However, this approaches ignore most of the effects mechanically driven at the micro and macro scale. In this framework, the integration of multiphysics and multiscale simulations (16, 17, 18) into GKN system

simulators can fill the gap between different disciplines: solid mechanics, control theory, electrotechnics and electronics. This thesis is an attempt in this direction, where the focus is on EHs based on piezoceramics and piezopolymers. Nonlinearities arising from different aspects, such as material and geometrical effects, are taken into account in the simulations through the identification of nonlinear circuit components. Moreover, computational time for nonlinear dynamic multiscale analyses is reduced, gaining a big picture about energy performances driven by micro and macro scale features and variables.

1.2 Thesis outlines

This thesis is divided into five chapters, as follows:

Chapter 1 motivates the necessity of the research, outlining objectives and structure of this document.

Chapter 2 provides a detailed overview of linear piezoelectricity theory, as an essential background for nonlinear methods and models discussed in the following chapters. Fundamental laws describing the electrostatic and linear elastic problem are first assessed separately. Moreover, the thermodynamic framework in which smart materials modeling techniques have been developed is presented, through a short summary of thermodynamic potentials. This gives the basis for the subsequent inclusion of hysteretic behaviors in the constitutive relations of the material. The derivation of the constitutive equations for a piezoelectric material is then reported, along with a rigorous reduction to the unidirectional case. Finally, equations governing the piezoelectric problem, in both strong and weak forms, are reported as a preliminary step toward the extension to the nonlinear formulation.

Chapter 3 presents the derivation of a multi-scale electromechanically coupled model for piezoceramics EHs. It is able to reproduce effects of hysteresis on the overall device dynamic performances. A physics-based free energy model has been employed for reproducing the switching of crystal domains (material mesoscopic scale) under applied electric and strain fields. The multiscale feature allows for including crystal mesoscopic dynamics in the evolution of macroscopic variables describing the behavior of the considered devices. A

circuit representation of the resulting model is also provided, as a tool for effectively visualizing and interpreting the role of the material mesoscopic evolution on the energy transduction process. Results of numerical analyses are reported for two case studies, highlighting the role of material nonlinearities by activating or suppressing mesoscopic dynamics in the model.

Chapter 4 presents an effective hybrid computational framework aimed at modeling the role of geometric nonlinearities (due to large deformations) on the response of flexible PDVF based EHs. The proposed approach employs reduced-order modeling techniques enhanced by the inclusion of lumped parameters taking into account the evolution of macroscopic quantities in the physical domain, which is provided by static nonlinear FE analyses. A circuit representation of the resulting reduced-order model is also presented. A large parametric investigation is reported, showing the role of material and geometrical parameters in the nonlinear response of two type of devices. Experimental validation is also provided.

Chapter 5 reports concluding remarks and comments on the future work.

2

Modeling piezoelectric solids: governing equations and theoretical aspects

As a preliminary step to the inclusion of nonlinear features into modeling piezoelectric material behaviors, equations governing the responses of EH devices under the assumption of linear elastic behavior are here recalled, in a general thermodynamic setting. In the first part of this chapter, a short review of the electromagnetism fundamental laws is reported. The final aim is to show the governing equations of the electrostatic problem, which is of interest for the applications reported in this thesis. In the second part, a detailed derivation of general equations governing the mechanical equilibrium is given. It is here noticed that provided equations are of general validity in both small and large strain problems. Since the piezoelectric constitutive equations are derived from the definition of suitable thermodynamic potentials - which quantify energies determining the material equilibrium state - a short summary of thermodynamic potentials is reported in the third part of the chapter. This results in a general framework that allows for including, in a natural way, hysteretic behaviors in the constitutive relations of the material. In the final part of the chapter, after introducing the assumption of linear elastic constitutive equations for the piezoelectric material, both the *strong* and *weak* forms of the coupled differential equations governing the electromechanical problem are presented.

2.1 Electromagnetism fundamental laws

2.1.1 Maxwell's equations

As an essential support in the comprehension and modeling of electromagnetic phenomena, a brief review of the well known Maxwell's Equations (MEs) is hereafter reported. MEs unify results previously achieved by Gauss, Ampere and Faraday in the description of electrostatic and electromagnetic phenomena. They consists in four Partial Derivative Equations (PDEs) that, along with the definition of the dielectric displacement vector $\overline{D}$ and the magnetic induction $\overline{H}$, describe the static and the dynamic behavior of both the electric and the magnetic field ($\overline{E}$ and $\overline{B}$ respectively) in the most general possible conditions (i.e. presence of moving charge distributions in polarized or magnetizable media).

The Maxwell's equations consists of the following laws:

- the Gauss's law;
- the Faraday's law;
- the Gauss's law for the magnetic field;
- the Ampere-Maxwell law.

2.1.1.1 The Gauss's law in the vacuum space

Let us consider a continuous charge distribution in the vacuum space characterized by a volumetric density $\rho_e = \rho_e(x, y, z)$. Let S be a closed surface (*gaussian* surface) in the tree-dimensional space. The Gauss's law states that the flux of the electric field $\overline{E}$ through S is given by the ratio of the electrical charge inside the considered surface to the vacuum permittivity ε_0:

$$\oint_S \overline{E} \cdot \overline{\mathrm{d}S} = \frac{1}{\varepsilon_0} \int_{Vol} \rho_e \mathrm{d}Vol \ , \tag{2.1}$$

where the integral in the right-hand side represents the total charge (q_e) within S and $\overline{\mathrm{d}S}$ is a vector normal to the infinitesimal area $\mathrm{d}S$ (having magnitude $\mathrm{d}S$).

Equation 2.1 can be written in a differential form, expressing the relationship between the electric field gradient and charge density ρ_e in local terms:

$$\overline{\nabla} \cdot \overline{E} = \frac{\partial E_x}{\partial x} + \frac{\partial E_y}{\partial y} + \frac{\partial E_z}{\partial z} = \frac{\rho_e}{\varepsilon_0} \ , \tag{2.2}$$

where it has been denoted by $\overline{\nabla}$ the *gradient vector*:

$$\overline{\nabla} = \left[\frac{\partial}{\partial x}, \frac{\partial}{\partial y}, \frac{\partial}{\partial z}\right]^T \ . \tag{2.3}$$

PDE 2.2 expresses a property of the electric field that must be satisfied in any point of the space. The electric field components cannot change in an arbitrary way: their derivatives with respect to spatial coordinates are interrelated in a way that depends on the charge density in the considered point. Moreover, equation 2.2 states that in any point of the space where no charge exists ($\rho_e = 0$), the divergence of $\overline{E}$ must be equal to zero.

2.1.1.2 The Faraday's law of induction

The Faraday's law of induction makes use of the *magnetic flux* (Φ_B) through a generic surface S_Γ having the wire loop Γ as a boundary:

$$\Phi_B = \int_{S_\Gamma} \overline{B} \cdot \overline{\mathrm{d}S}_\Gamma \ , \tag{2.4}$$

where we denoted as $\overline{B}$ the magnetic field.

The law expresses the electromotive force (ε_f) induced on Γ as a function of the rate of change of the magnetic flux through S_Γ:

$$\varepsilon_f = -\frac{\mathrm{d}}{\mathrm{d}t}\Phi_B \ . \tag{2.5}$$

Since the Electromotive Force (EMF) can be defined as the circular integral of the electric field along Γ:

$$\varepsilon_f = \oint_\Gamma \overline{E} \cdot \overline{\mathrm{d}l} \ , \tag{2.6}$$

through 2.4 and 2.6, it is possible to recast 2.5 in the following integral form:

$$\oint_\Gamma \overline{E} \cdot \overline{\mathrm{d}l} = -\frac{\mathrm{d}}{\mathrm{d}t} \int_{S_\Gamma} \overline{B} \cdot \overline{\mathrm{d}S_\Gamma} \ . \tag{2.7}$$

The differential form of the Faraday's law is expressed by the following PDE:

$$\overline{\nabla} \times \overline{E} = -\frac{\partial \overline{B}}{\partial t} \ , \tag{2.8}$$

which states that the curl of $\overline{E}$, evaluated in a generic point, is equal to the time derivative of $\overline{B}$ evaluated in the same point, with opposite sign.

2.1.1.3 The Gauss's law for the magnetic field

The Gauss's law for the magnetic field states that the flux of a magnetic field $\overline{B}$ through a closed surface S is always equal to zero:

$$\oint_S \overline{B} \cdot \overline{\mathrm{d}S} = 0 \ . \tag{2.9}$$

The integral relation 2.9 has the following differential expression:

$$\overline{\nabla} \cdot \overline{B} = 0 \ . \tag{2.10}$$

The null divergence condition (2.10) for the magnetic field, implies that $\overline{B}$ is an incompressible (*solenoidal*) vector field. Condition (2.10) rules out the existence of magnetic monopoles.

2.1.1.4 The Ampere-Maxwell law

The Ampere-Maxwell law represents the extension of the Ampere's law to regimes characterized by non-stationary currents ($\partial \rho_e / \partial t \neq 0$). Let us consider, in the vacuum space, a loop wire γ and an arbitrary surface S_γ having γ as a boundary.

According to the Ampere's law, the circular integral of the magnetic field $\overline{B}$ along γ is given by the product of the vacuum permeability (μ_0) to the current i enclosed by the loop wire γ:

$$\oint_\gamma \overline{B} \cdot \overline{\mathrm{d}l} = \mu_0 i = \mu_0 \int_{S_\gamma} \overline{j} \cdot \overline{\mathrm{d}S} \ , \tag{2.11}$$

where current i is defined as the flux of the current density $\overline{j}$ through S_γ.

Equation 2.11 can be expressed in the differential form as follows:

$$\overline{\nabla} \times \overline{B} = \mu_0 \overline{j} \ . \tag{2.12}$$

The Ampere law, as expressed in 2.11 and 2.12, is in agreement with the charge conservation principle only in the case of static conditions. If, in fact, we apply the divergence operator to both sides of (2.12), it results:

$$\overline{\nabla} \cdot \overline{\nabla} \times \overline{B} = \mu_0 \overline{\nabla} \cdot \overline{j} \ , \tag{2.13}$$

where the left-hand side term is always equal to zero ($\overline{\nabla} \cdot \overline{\nabla} \times \overline{B} \equiv 0$) but, in general, the right-hand side is not.

The charge continuity equation, in fact, states that:

$$\overline{\nabla} \cdot \overline{j} = -\frac{\partial \rho_e}{\partial t} \ , \tag{2.14}$$

from which results that $\overline{j}$ is solenoidal (i.e., $\overline{\nabla} \cdot \overline{j} = 0$) only in static conditions (i.e., $\rho_e = \text{const.}$).

If we express - through the Gauss's law (2.2) - the charge density ρ_e as a function of the electric field, it results that:

$$\frac{\partial \rho_e}{\partial t} = \varepsilon_0 \frac{\partial}{\partial t} \overline{\nabla} \cdot \overline{E} = \varepsilon_0 \overline{\nabla} \cdot \frac{\partial \overline{E}}{\partial t} \ . \tag{2.15}$$

By substituting 2.15 in 2.12, we obtain:

$$\overline{\nabla} \cdot \left(\overline{j} + \varepsilon_0 \frac{\partial \overline{E}}{\partial t} \right) = 0 \ , \tag{2.16}$$

which introduces a new charge density vector $\overline{j}_{tot} = \overline{j} + \varepsilon_0 \frac{\partial \overline{E}}{\partial t}$ whose divergence is always equal to zero (i.e., $\overline{j}_{tot}$ is solenoidal) and, therefore, can be introduced in (2.12) in order to extend its validity to the non-stationary case.

The flux of vector $\overline{j}_{tot}$ through S_γ gives a current that consists in two terms:

$$i_{tot} = \int_{S_\gamma} \overline{j}_{tot} \cdot \overline{\mathrm{d}S} = \int_{S_\gamma} \left(\overline{j} + \varepsilon_0 \frac{\partial \overline{E}}{\partial t} \right) \cdot \overline{\mathrm{d}S} = i + i_s \ , \tag{2.17}$$

where i_s denotes the *displacement current*.

By considering $\overline{j}_{tot}$, in place of $\overline{j}$, in equation 2.12, the differential form of the Ampere-Maxwell law in the vacuum space can be written as follows:

$$\overline{\nabla} \times \overline{B} = \mu_0 \left(\overline{j} + \varepsilon_0 \frac{\partial \overline{E}}{\partial t} \right) \ . \tag{2.18}$$

2.1.2 Polarization density vector

Differently from the case of conductors, dielectrics present no loosely bound, or free, electrons that may drift through the material. Therefore, an externally applied electric field produces practically no current flows within the material. However, other interactions with the atomic structure occurs, generating *dipole moments*.

With reference to Fig. 2.1-a, let us consider a neutral system of two point charges ($\pm q_e$) immersed in an electric field ($\overline{E}$). Under the effect of the coulombian force exerted by $\overline{E}$, charges tends to separate, reaching an equilibrium configuration characterized by a relative distance d. The dipole moment ($\overline{p}_o$) associated to the

system in this new equilibrium configuration can be evaluated by the following expression:

$$\overline{p}_o = q_e \overline{d} \ , \tag{2.19}$$

where vector $\overline{d}$ represents the position of the positive charge with respect to the negative one.

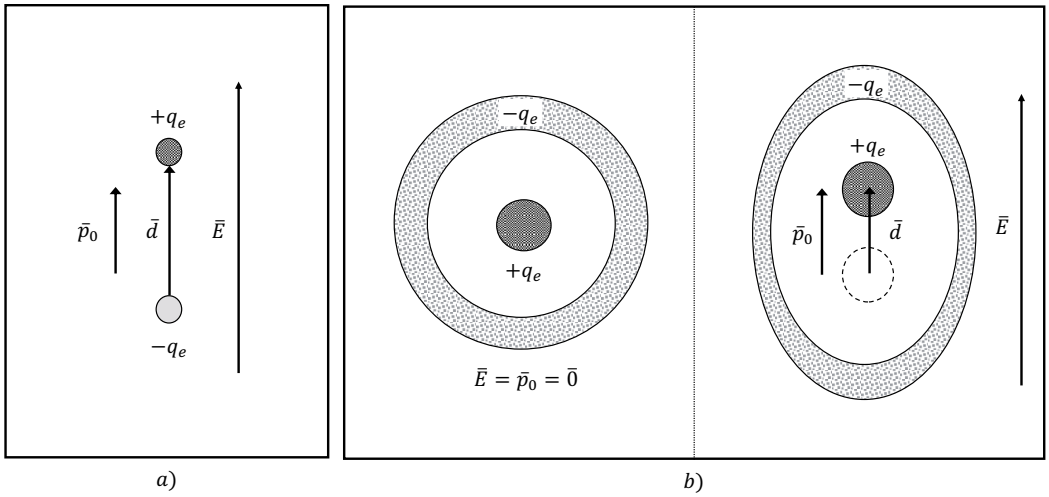

Figure 2.1: Dipole moment $\overline{p}_o$ due to the applied electric field $\overline{E}$. a) case of a two point charge system; b) effect of $\overline{E}$ on an atomic structure.

The concept of dipole moment, introduced for the case of two point charges, can be extended to the atomic structure: with reference to Fig. 2.1-b, under the effect of $\overline{E}$ the deformation of the electron cloud around the nucleus results in a relative distance d between the barycenters of negative and positive charges.

The reasoning is similar for the molecular structure of a generic dielectric material. A single molecule, in fact, can be considered as a system defined by a globally neutral spatial distribution of charges. If we denote by q_t the total charge of such a system, it must result:

$$q_t = \int \rho_e(x,y,z) \ dVol = \int \rho_e^+ \ dVol + \int \rho_e^- \ dVol = q_e + (-q_e) = 0 \ . \tag{2.20}$$

Molecules can be grouped in two categories: *non-polar* and *polar* molecules. The former present a symmetric distribution of positive and negative charges, resulting in a null dipole moment; the latter are characterized by a non-symmetric structure that produces an inherent non-zero dipole moment.

Therefore, two different polarization mechanisms can be distinguished for a dielectric material:

- *deformation polarization*: it occurs when the electric field $\overline{E}$ acts on a non-polar molecule. In this case, the positive charges of the molecule tends to move in the same direction of the electric field, while negative charge move in the opposite direction. This results in a deformed charge distribution producing the separation of positive and negative charge barycenters.

- *orientation polarization*: it occurs when the electric field $\overline{E}$ acts on a molecule presenting an inherent dipole moment. In this case the molecule is subjected to a torque that aims at aligning its dipole moment according to $\overline{E}$. It is worth to highlight that in a specimen of matter consisting in polar molecules, single dipole moments are randomly oriented unless an external electric field is applied.

Regardless of the mechanism involved in the polarization process, by denoting as d_b the distance separating the barycenters of positive and negative ions of a single molecule under the effect of $\overline{E}$, the relative dipole moment can be evaluated as:

$$^{1}\ \bar{p} = q_e \bar{d_b}\ . \tag{2.21}$$

The *polarization density* vector $\overline{P}$ takes into account this phenomenon by averaging it on the volume of the material:

$$\overline{P} = N\overline{p}\ , \tag{2.22}$$

where N is the number of molecules per unit volume.

With reference to *normal* (19) and isotropic dielectric material, fields $\overline{P}$ and $\overline{E}$ are in the following relationship:

$$\overline{P} = \varepsilon_0(\varepsilon_r - 1)\overline{E} = \varepsilon_0 \chi \overline{E}\ , \tag{2.23}$$

where constants ε_r and χ represent the relative permittivity and the o electric susceptibility, respectively. Relation 2.23 describes the dependence of the polarization

[1] Note that expression 2.21 is no more valid for distributions resulting in a global charge different from zero (19).

density vector on the electric field for *isotropic* dielectrics. The following matrix equation stands for anisotropic dielectric materials:

$$\begin{bmatrix} P_x \\ P_y \\ P_z \end{bmatrix} = \varepsilon_0 \begin{bmatrix} \chi_{11} & \chi_{12} & \chi_{13} \\ \chi_{21} & \chi_{22} & \chi_{23} \\ \chi_{31} & \chi_{32} & \chi_{33} \end{bmatrix} \begin{bmatrix} E_x \\ E_y \\ E_z \end{bmatrix} , \tag{2.24}$$

which clarifies that χ is no more a scalar quantity but a second order tensor.

Since linear modeling is the primary focus of this chapter, the case of *ferroelectric* materials, which present a complex nonlinear relationship between $\overline{E}$ and $\overline{P}$, is not addressed here.

2.1.3 Polarization charges

Polarization $\overline{P}$ induces charge distributions on the surface of a dielectric material characterized by a density σ_{e_b} defined, in any point, as:

$$\sigma_{e_b} = \overline{P} \cdot \overline{n} , \tag{2.25}$$

where $\overline{n}$ is the unit vector normal to the surface in the considered point.

In case of non-uniform polarization, a charge distribution in the volume of the material also appears, which is characterized by a density ρ_{e_b}:

$$\rho_{e_b} = -\overline{\nabla} \cdot \overline{P} . \tag{2.26}$$

From 2.26 it can be inferred that volumetric charge density ρ_{e_b} resulting for the case of uniform polarization is equal to zero. Therefore, if $\overline{\nabla} \cdot \overline{P} = 0$, polarization charges are distributed only on the surface of the dielectric material. Charges relative to distributions 2.25 and 2.26 are referred to as *bonded* charges, in contrast with *free* charges present in conductors.

2.1.4 Electric displacement vector

The electric displacement (or *electric induction*) vector is defined as follows:

$$\overline{D} = \varepsilon_0 \overline{E} + \overline{P} . \tag{2.27}$$

Similarly to what has been reported for the polarization vector in the previous subsection, expressions of $\overline{D}$ for the case of linear, isotropic and anisotropic dielectric material are hereafter reported:

- *isotropic dielectric material*: by substituting 2.23 in 2.27, it results

$$\overline{D} = \varepsilon_0 \overline{E} + \varepsilon_0 \chi \overline{E} = \varepsilon_0 (1 + \chi) \overline{E} = \varepsilon_0 \varepsilon_r \overline{E} = \varepsilon \overline{E} \ , \tag{2.28}$$

  where it has been denoted by $\varepsilon = \varepsilon_0 \varepsilon_r$ the absolute dielectric constant of the considered material.

- *anisotropic dielectric*: by considering 2.24 it results

$$\begin{bmatrix} D_x \\ D_y \\ D_z \end{bmatrix} = \varepsilon_0 \begin{bmatrix} 1 + \chi_{11} & \chi_{12} & \chi_{13} \\ \chi_{21} & 1 + \chi_{22} & \chi_{23} \\ \chi_{31} & \chi_{32} & 1 + \chi_{33} \end{bmatrix} \begin{bmatrix} E_x \\ E_y \\ E_z \end{bmatrix} . \tag{2.29}$$

2.1.5 Gauss's law for a dielectric medium

The Gauss's law, which has been previously introduced for the vacuum space, can be extended to the case of dielectric medium by considering both free charges (q_e) and bonded charges (q_{e_b}) as sources for the total electric field $\overline{E}$:

$$\oint_S \overline{E} \cdot \overline{\mathrm{d}S} = \frac{q_e + q_{e_b}}{\varepsilon_0} \ . \tag{2.30}$$

Equation 2.30 can be expressed, in differential form, as follows:

$$\overline{\nabla} \cdot \overline{E} = \frac{\rho_e + \rho_{e_b}}{\varepsilon_0} \ . \tag{2.31}$$

By substituting 2.26 in 2.31, it results:

$$\varepsilon_0 \overline{\nabla} \cdot \overline{E} = \rho_e - \overline{\nabla} \cdot \overline{P} \Rightarrow \overline{\nabla} \cdot (\varepsilon_0 \overline{E} + \overline{P}) = \rho_e \ , \tag{2.32}$$

which represents the differential form of the Gauss's law in presence of dielectric medium:

$$\overline{\nabla} \cdot \overline{D} = \rho_e \ . \tag{2.33}$$

The integral form of 2.33 is given by the following:

$$\oint_S \overline{D} \cdot \overline{dS} = q_e \ . \tag{2.34}$$

From equation 2.34 it can be inferred that the flux of vector $\overline{D}$ through the arbitrary closed surface S is only function of the free charge enclosed by the surface and do not depends on bonded charges q_{e_b}.

2.1.6 Magnetic polarization vector

A qualitative interpretation of physical phenomena related to the magnetization of matter is provided by Bohr's atomic model. According to this simplified model, electrons travel around the nucleus in circular orbits. These orbits can be assumed as infinitesimal loop wires in which a current i_e flows:

$$i_e = \frac{\mathrm{d}q_e}{\mathrm{d}t} = -\frac{e\omega}{2\pi} \ , \tag{2.35}$$

where e is the electron charge and ω is the electron angular velocity.

Through the Ampere's equivalence principle (19) an electron circular orbits can be assumed as a magnetic dipole characterized by a magnetic moment equal to:

$$\mathrm{d}\overline{m} = i_e \overline{\mathrm{d}S} \ , \tag{2.36}$$

where $\overline{dS}$ is the normal vector to the loop wire planar surface, whose direction depends on i_e (through the *right-hand rule*).

Generally, the overall effect of the electrons orbit is such that a null magnetic dipole is observed. When an external magnetic field is applied, perturbations in the electron motion occur, determining a magnetic moment for the atom, which counteract to the external perturbation. The process is similar to the deformation polarization for dielectrics[1]. Concluding, atoms or molecules subjected to a magnetic field $\overline{B}$ react by assuming a magnetic moment $\overline{m}$ oriented accordingly with $\overline{B}$. Similarly to the case of dielectric polarization, the *magnetization* vector can be introduced as:

$$\overline{M} = N\overline{m} \ , \tag{2.37}$$

where N represents the number of molecules per unit volume.

2.1.7 Magnetization currents

The following current densities can be associated to the magnetic dipole moment density $\overline{M}$:

$$\bar{j}_{m_{sup}} = \overline{M} \times \overline{n} \ , \tag{2.38}$$

[1] Asymmetries in the molecular structure of certain materials can result in an inherit magnetic moment. In these cases, the application of an external magnetic field produces a partial orientation of magnetic dipoles, according to the external magnetic field.

$$\overline{j}_{m_{vol}} = \overline{\nabla} \times \overline{M} \ . \tag{2.39}$$

Equation (2.38) refers to a surface current density ($\overline{n}$ represents the outward pointing unit normal vector with respect to the specimen surface). Current density defined by (2.39) refers to currents located in the volume of the considered material.

Magnetization currents allow for considering the magnetic field generated by the magnetized material as the field produced by a surface current distribution with density $\overline{j}_{m_{sup}}$ and a volumetric current distribution with density $\overline{j}_{m_{vol}}$.

2.1.8 Magnetic field strength

According to reasonings similar to the ones leading to the introduction of the electric displacement vector $\overline{D}$, the following auxiliary vector field can be introduced for describing magnetization phenomena:

$$\overline{H} = \frac{\overline{B}}{\mu_0} - \overline{M} \ . \tag{2.40}$$

For an isotropic, homogeneous, linear material the relationship between $\overline{M}$ and $\overline{H}$ is given by the following:

$$\overline{M} = \chi_m \overline{H} \ , \tag{2.41}$$

where the magnetic susceptibility (χ_m) is a constant. With reference to materials for which (2.41) is true, the following linear relationship between $\overline{B}$ and $\overline{H}$ can be derived from (2.40):

$$\overline{B} = \mu_0 \left(\overline{H} + \overline{M}\right) = \mu_0 \left(1 + \chi_m\right) \overline{H} = \mu_0 \mu_r \overline{H} = \mu \overline{H} \ , \tag{2.42}$$

where μ_r and μ are the material relative magnetic permittivity and magnetic permittivity, respectively.

As previously highlighted for dielectrics, parameter μ is a scalar quantity for isotropic materials, otherwise it is defined as a second order tensor[1].

[1] A discussion on *ferromagnetics*, which are materials characterized by a nonlinear, hysteretic $\overline{B}$-$\overline{H}$ characteristics, is out of the scope of this thesis.

2.1.9 Generalized Ampere-Maxwell law

It is now possible to provide a formulation of the Ampere-Maxwell theorem that accounts for all possible sources of magnetic effects. Three different kind of sources are involved:

- conduction currents, distributed with density $\overline{j}$;
- magnetization currents, distributed with density $\overline{j}_{m_{vol}}$;
- polarization currents, distributed with density $\overline{j}_P = \frac{\partial \overline{P}}{\partial t}$,

therefore, the total charge density $\overline{j}_{tot}$ can be written as follows:

$$\overline{j}_{tot} = \overline{j} + \overline{j}_{m_{vol}} + \overline{j}_P = \overline{j} + \overline{\nabla} \times \overline{M} + \frac{\partial \overline{P}}{\partial t} \ . \tag{2.43}$$

According to the charge continuity equation, it must be:

$$\overline{\nabla} \cdot \overline{j}_{tot} + \frac{\partial \rho_{tot}}{\partial t} = 0 \ , \tag{2.44}$$

where the total charge density $\rho_{tot} = \rho_e + \rho_{e_b}$ consists of a term related to the free charge q_e and a term related to the polarization charge q_{e_b}. Equation (2.44) can be recast as follows:

$$\overline{\nabla} \cdot \left(\overline{j} + \overline{\nabla} \times \overline{M} + \frac{\partial \overline{P}}{\partial t} \right) + \frac{\partial \left(\rho_e + \rho_{e_b} \right)}{\partial t} = 0 \ , \tag{2.45}$$

By substituting (2.31) in (2.45), it results:

$$\overline{\nabla} \cdot \left(\overline{j} + \overline{\nabla} \times \overline{M} + \frac{\partial}{\partial t} \left(\varepsilon_0 \overline{E} + \overline{P} \right) \right) = 0 \ . \tag{2.46}$$

The argument of the divergence operator in (2.46) is a solenoidal current density $\overline{j}'$ that, by taking into account (2.27), is defined by:

$$\overline{j}' = \overline{j} + \overline{\nabla} \times \overline{M} + \overline{j}_D \ , \tag{2.47}$$

where quantity $\overline{j}_D$ denotes the the *displacement current* density:

$$\overline{j}_D = \frac{\partial \overline{D}}{\partial t} \ . \tag{2.48}$$

By rewriting the Ampere-Maxwell law (2.12) considering current density $\overline{j}'$, it results that:

$$\overline{\nabla} \times \left(\frac{\overline{B}}{\mu_0} - \overline{M} \right) = \overline{j} + \frac{\partial \overline{D}}{\partial t} \ , \tag{2.49}$$

which, taking into account (2.40), provides the generalized Ampere-Maxwell theorem:

$$\overline{\nabla} \times \overline{H} = \overline{j} + \frac{\partial \overline{D}}{\partial t} \ . \tag{2.50}$$

2.1.10 Formulation of the electrostatic problem

In previous subsections we reported the fundamental law of electromagnetism, which allows for describing electromagnetic phenomena in the most general conditions. From an engineering point of view, it is useful to distinguish two main *domains* of interest (20):

- *high frequency domain*, it involves the study of electromagnetic radiations. The high rate of change characterizing these phenomena makes particularly relevant the contribution due to the displacement currents, which cannot be neglected;

- *low frequency domain*, it comprises all applications for which the contribution of displacement currents can be neglected.

For the low frequency domain ($\overline{j}_D \approx \overline{0}$), Maxwell equations can be recast, along with the definition of auxiliary vectors $\overline{D}$ and $\overline{H}$, as follows:

$$\begin{aligned}
&\overline{\nabla} \cdot \overline{D} = \rho \ , \\
&\overline{\nabla} \times \overline{E} = -\frac{\partial \overline{B}}{\partial t} \ , \\
&\overline{\nabla} \cdot \overline{B} = 0 \ , \\
&\overline{\nabla} \times \overline{H} = \overline{j} \ , \\
&\overline{D} = \varepsilon_0 \overline{E} + \overline{P} \ , \\
&\overline{B} = \mu_0 \overline{H} + \overline{M} \ .
\end{aligned} \tag{2.51}$$

Moreover, in *quasi-static* conditions can be further simplified and subdivided into two independent set of equations, describing separately electrostatic and magnetostatic phenomena. For the electrostatic domain it results:

$$\begin{aligned} &\overline{\nabla} \cdot \overline{D} = \rho \ , \\ &\overline{\nabla} \times \overline{E} = \overline{0} \ , \\ &\overline{D} = \varepsilon_0 \overline{E} + \overline{P} \ . \end{aligned} \tag{2.52}$$

The second of (2.52), states the conservative nature of the electric filed $\overline{E}$. As a consequence, the electric field can be expressed as the gradient of a scalar potential φ:

$$\overline{E} = -\overline{\nabla}\varphi \ . \tag{2.53}$$

The following boundary conditions must be reported for $\overline{E}$ and $\overline{D}$, which must be considered on separation surfaces between different materials (19):

$$\begin{aligned} &\left(\overline{D}_2 - \overline{D}_1\right) \cdot \overline{n} = \sigma_e \ , \\ &\left(\overline{E}_2 - \overline{E}_1\right) \times \overline{n} = \overline{0} \ , \end{aligned} \tag{2.54}$$

where $\overline{n}$ is the unit normal vector of the separation surface, pointing from medium 1 to medium 2.

2.2 The mechanical problem

2.2.1 Navier's equations

Let us consider a continuum body having volume Vol and surface S, which is subjected to volume forces $\overline{F}_V$ and surface forces $\overline{p}_m$.

Assuming the body in an equilibrium condition, following equations must be satisfied:

$$\int_{Vol} \overline{F}_V \mathrm{d}Vol + \int_S \overline{p}_m \mathrm{d}S = \overline{0} \ , \tag{2.55}$$

$$\int_{Vol} \overline{r} \times \overline{F}_V \mathrm{d}Vol + \int_S \overline{r} \times \overline{p}_m \mathrm{d}S = \overline{0} \ , \tag{2.56}$$

where $\overline{r}$ represent the position vector of the infinitesimal volume $\mathrm{d}Vol$.

Let us now focus on an infinitesimal cubic volume of the considered body, having sides parallel to the axes of the cartesian reference system.

In order to be in equilibrium, this infinitesimal portion of the material must be under the effect of forces preventing translational and rotational motions: *tension vector* $\bar{t}_x$ acts on the face of the cube that is normal to X axis and, in a similar way, vectors $\bar{t}_y$ and $\bar{t}_z$ act on faces normal to Y axis and Z axis respectively. Therefore the tensional state in a specific spatial point P is given by:

$$\begin{aligned} \bar{t}_x &= \sigma_{xx}\hat{\imath} + \sigma_{xy}\hat{\jmath} + \sigma_{xz}\hat{k} \ , \\ \bar{t}_y &= \sigma_{yx}\hat{\imath} + \sigma_{yy}\hat{\jmath} + \sigma_{yz}\hat{k} \ , \\ \bar{t}_z &= \sigma_{zx}\hat{\imath} + \sigma_{zy}\hat{\jmath} + \sigma_{zz}\hat{k} \ . \end{aligned} \tag{2.57}$$

Let us consider a tetrahedral volume surrounding point P having tree sides that are parallel to axes X, Y and Z and only one oblique face with a normal versor defined by:

$$\overline{n}_\alpha = n_x\hat{\imath} + n_y\hat{\jmath} + n_z\hat{k} \ . \tag{2.58}$$

This infinitesimal tetrahedral volume is under the effect of tensions $-\bar{t}_x$, $-\bar{t}_y$, $-\bar{t}_z$ and $-\bar{t}_\alpha$, therefore, by assuming as negligible the effect of volume forces, the translational equilibrium states that:

$$\mathrm{d}\Gamma_\alpha\bar{t}_\alpha - \mathrm{d}\Gamma_x\bar{t}_x - \mathrm{d}\Gamma_y\bar{t}_y - \mathrm{d}\Gamma_z\bar{t}_z = \overline{0} \ , \tag{2.59}$$

where $\mathrm{d}\Gamma_\alpha$, $\mathrm{d}\Gamma_x$, $\mathrm{d}\Gamma_y$ and $\mathrm{d}\Gamma_z$ are the areas related to faces normal to the $\overline{n}_\alpha$ vector and the X, Y, Z axes respectively. By considering the following geometric relations:

$$\mathrm{d}\Gamma_x = n_x\mathrm{d}\Gamma_\alpha \ , \qquad \mathrm{d}\Gamma_y = n_y\mathrm{d}\Gamma_\alpha \ , \qquad \mathrm{d}\Gamma_z = n_z\mathrm{d}\Gamma_\alpha \ , \tag{2.60}$$

equation 2.59 can be recast as:

$$\bar{t}_\alpha = \bar{t}_x n_x + \bar{t}_y n_y + \bar{t}_z n_z \ . \tag{2.61}$$

By introducing 2.57 in 2.61, it results:

$$\begin{aligned} \bar{t}_\alpha = {} & \big(\sigma_{xx}n_x + \sigma_{yx}n_y + \sigma_{zx}n_z\big)\hat{\imath} + \big(\sigma_{xy}n_x + \sigma_{yy}n_y + \sigma_{zy}n_z\big)\hat{\jmath} \\ & + \big(\sigma_{xz}n_x + \sigma_{yz}n_y + \sigma_{zz}n_z\big)\hat{k}. \end{aligned} \tag{2.62}$$

If it is denoted by $[\,\sigma\,]$ the Cauchy tensor (21):

$$[\,\sigma\,] = \begin{bmatrix} \sigma_{xx} & \sigma_{xy} & \sigma_{xz} \\ \sigma_{yx} & \sigma_{yy} & \sigma_{yz} \\ \sigma_{zx} & \sigma_{zy} & \sigma_{zz} \end{bmatrix} \ , \tag{2.63}$$

equation 2.62 can be rewritten, in compact form, as follows:

$$\overline{t}_\alpha = [\,\sigma\,]^T\,\overline{n}_\alpha\ . \tag{2.64}$$

From equation (2.64) it can be inferred how the Cauchy tensor is a transformation that applied to the generic unit vector $\overline{n}_\alpha$, by using just the components of vectors $\overline{t}_x$, $\overline{t}_y$ and $\overline{t}_z$, gives as a result the vector $\overline{t}_\alpha$.

Let us now consider an arbitrary portion Vol' of the volume Vol, which has a closed, regular surface Ω as a boundary. The translational and rotational equilibrium relations on this new domain can be written as follows:

$$\int_{Vol'} \overline{F}_V \mathrm{d}Vol + \int_\Omega [\,\sigma\,]^T\,\overline{n}\mathrm{d}\Omega = \overline{0}\ , \tag{2.65}$$

$$\int_{Vol'} \overline{r}\times\overline{F}_V \mathrm{d}Vol + \int_\Omega \overline{r}\times\left[\,\sigma\,\right]^T\,\overline{n}\mathrm{d}\Omega = \overline{0}\ , \tag{2.66}$$

where $\overline{n}$ represents the unit vector normal to the surface Ω. Vectorial equation (2.65) is equivalent to the following tree scalar relations:

$$\begin{aligned}
&\int_{Vol'} F_{V_x}\mathrm{d}Vol + \int_\Omega \left(\sigma_{xx}n_x + \sigma_{yx}n_y + \sigma_{zx}n_z\right)\mathrm{d}\Omega = 0\ ,\\
&\int_{Vol'} F_{V_y}\mathrm{d}Vol + \int_\Omega \left(\sigma_{xy}n_x + \sigma_{yy}n_y + \sigma_{zy}n_z\right)\mathrm{d}\Omega = 0\ ,\\
&\int_{Vol'} F_{V_z}\mathrm{d}Vol + \int_\Omega \left(\sigma_{xz}n_x + \sigma_{yz}n_y + \sigma_{zz}n_z\right)\mathrm{d}\Omega = 0\ .
\end{aligned} \tag{2.67}$$

It is possible to convert surface integrals in (2.67) into volume integrals by applying the divergence theorem. Therefore, it results what follows:

$$\begin{aligned}
&\int_{Vol'} \left(F_{V_x} + \frac{\partial\sigma_{xx}}{\partial x} + \frac{\partial\sigma_{yx}}{\partial y} + \frac{\partial\sigma_{zx}}{\partial z}\right)\mathrm{d}Vol = 0,\\
&\int_{Vol'} \left(F_{V_y} + \frac{\partial\sigma_{xy}}{\partial x} + \frac{\partial\sigma_{yy}}{\partial y} + \frac{\partial\sigma_{zy}}{\partial z}\right)\mathrm{d}Vol = 0,\\
&\int_{Vol'} \left(F_{V_z} + \frac{\partial\sigma_{xz}}{\partial x} + \frac{\partial\sigma_{yz}}{\partial y} + \frac{\partial\sigma_{zz}}{\partial z}\right)\mathrm{d}Vol = 0.
\end{aligned} \tag{2.68}$$

Since volume Vol' has been arbitrarily chosen, arguments of integrals reported in equations (2.68) must be equal to zero. Therefore, the following equilibrium

equations can be obtained:

$$\begin{aligned} F_{V_x} + \frac{\partial \sigma_{xx}}{\partial x} + \frac{\partial \sigma_{yx}}{\partial y} + \frac{\partial \sigma_{zx}}{\partial z} = 0 \ , \\ F_{V_y} + \frac{\partial \sigma_{xy}}{\partial x} + \frac{\partial \sigma_{yy}}{\partial y} + \frac{\partial \sigma_{zy}}{\partial z} = 0 \ , \\ F_{V_z} + \frac{\partial \sigma_{xz}}{\partial x} + \frac{\partial \sigma_{yz}}{\partial y} + \frac{\partial \sigma_{zz}}{\partial z} = 0 \ . \end{aligned} \tag{2.69}$$

From rotational equilibrium equation (2.66) and (2.69) the symmetry of the Cauchy tensor can be proved by achieving the following equalities:

$$\begin{aligned} \sigma_{xy} = \sigma_{yx} \ , \\ \sigma_{xz} = \sigma_{zx} \ , \\ \sigma_{yz} = \sigma_{zy} \ . \end{aligned} \tag{2.70}$$

Symmetry properties of tensor $[\,\sigma\,]$ allows for representing the tensional state of the considered material sample through a vector of six components:

$$[\,\sigma\,] = \begin{bmatrix} \sigma_{xx} & \sigma_{xy} & \sigma_{xz} \\ \sigma_{yx} & \sigma_{yy} & \sigma_{yz} \\ \sigma_{zx} & \sigma_{zy} & \sigma_{zz} \end{bmatrix} = \begin{bmatrix} \sigma_{11} & \sigma_{12} & \sigma_{13} \\ \sigma_{21} & \sigma_{22} & \sigma_{23} \\ \sigma_{31} & \sigma_{32} & \sigma_{33} \end{bmatrix} \ , \tag{2.71}$$

which, according to the *Vogit's notation*, is equivalent to the following vector:

$$\overline{\sigma} = \begin{bmatrix} \sigma_{xx} \\ \sigma_{yy} \\ \sigma_{zz} \\ \sigma_{yz} \\ \sigma_{xz} \\ \sigma_{xy} \end{bmatrix} = \begin{bmatrix} \sigma_{11} \\ \sigma_{22} \\ \sigma_{33} \\ \sigma_{23} \\ \sigma_{13} \\ \sigma_{12} \end{bmatrix} . \tag{2.72}$$

Equilibrium equations (2.69) can be recast in a compact form (20):

$$[\,\partial\,]^T\,\overline{\sigma} + \overline{F}_V = \overline{0} \ , \tag{2.73}$$

where the differential operator $[\,\partial\,]$ has been introduced:

$$[\,\partial\,]^T = \begin{bmatrix} \dfrac{\partial}{\partial x} & 0 & 0 & 0 & \dfrac{\partial}{\partial z} & \dfrac{\partial}{\partial y} \\ 0 & \dfrac{\partial}{\partial y} & 0 & \dfrac{\partial}{\partial z} & 0 & \dfrac{\partial}{\partial x} \\ 0 & 0 & \dfrac{\partial}{\partial z} & \dfrac{\partial}{\partial y} & \dfrac{\partial}{\partial x} & 0 \end{bmatrix} . \tag{2.74}$$

Navier's equations extend the static equilibrium condition expressed by (2.73) to the dynamic case, through the inclusion of inertial effects:

$$[\,\partial\,]^T\,\overline{\sigma} + \overline{F}_V = \rho\overline{a}\ , \tag{2.75}$$

where ρ is the density of the considered body and $\overline{a}$ denotes its acceleration.

2.2.2 Strain-displacement relations

Let us denote by $\mathscr{B}$ a continuum, characterized by an initial undeformed configuration $\mathscr{C}_0$. With reference to $\mathscr{C}_0$, the position in space of each point of $\mathscr{B}$ is represented through a vector $\overline{r}$, defined in a cartesian reference system $O; X, Y, Z$.

If a deformation of $\mathscr{B}$ occurs, transforming the body from $\mathscr{C}_0$ to a new deformed configuration $\mathscr{C}$, each point undergo to a displacement $\overline{\eta}$ that is given by the following expression:

$$\overline{\eta} = u(x,y,z)\,\hat{\imath} + v(x,y,z)\,\hat{\jmath} + w(x,y,z)\,\hat{k}\ . \tag{2.76}$$

It is assumed that functions u, v and w - defining the displacement vector components - along with their first order derivatives are continuous and sufficiently regular in the considered domain. This amounts to assuming that transformation $\mathscr{C}_0\mathscr{C}$ do not involve compenetration or fracture phenomena.

Let denote by A and B two generic points of $\mathscr{B}$. Displacements they undergo due to $\mathscr{C}_0\mathscr{C}$ transformation are given by:

$$\begin{aligned} \overline{\eta}_A &= u_A(x,y,z)\,\hat{\imath} + v_A(x,y,z)\,\hat{\jmath} + w_A(x,y,z)\,\hat{k}\ , \\ \overline{\eta}_B &= u_B(x,y,z)\,\hat{\imath} + v_B(x,y,z)\,\hat{\jmath} + w_B(x,y,z)\,\hat{k}\ . \end{aligned} \tag{2.77}$$

Therefore, if we denote by A' and B' the final positions of the considered points, it results that:

$$\begin{aligned} \overline{r}_{A'} &= \overline{r}_A + \overline{\eta}_A\ , \\ \overline{r}_{B'} &= \overline{r}_B + \overline{\eta}_B\ . \end{aligned} \tag{2.78}$$

The relative distance of the two points in the deformed configuration is than given by:

$$\overline{r}_{B'} - \overline{r}_{A'} = (\overline{r}_B - \overline{r}_A) + (\overline{\eta}_B - \overline{\eta}_A) \ . \tag{2.79}$$

By assuming points A and B infinitesimally close, in case of infinitesimal displacements, Equation (2.79) assumes the following form:

$$\overline{dr'} = \overline{dr} + \overline{d\eta} \ , \tag{2.80}$$

resulting in the following scalar equations:

$$\begin{aligned} dx' &= dx + du \ , \\ dy' &= dy + dv \ , \\ dz' &= dz + dw \ . \end{aligned} \tag{2.81}$$

Infinitesimal displacement components can be written has follows:

$$\begin{aligned} du &= \frac{\partial u}{\partial x}dx + \frac{\partial u}{\partial y}dy + \frac{\partial u}{\partial z}dz \ , \\ dv &= \frac{\partial v}{\partial x}dx + \frac{\partial v}{\partial y}dy + \frac{\partial v}{\partial z}dz \ , \\ dw &= \frac{\partial w}{\partial x}dx + \frac{\partial w}{\partial y}dy + \frac{\partial w}{\partial z}dz \ . \end{aligned} \tag{2.82}$$

By substituting (2.82) in (2.81), the following expressions can be obtained:

$$\begin{aligned} dx' &= \left(1 + \frac{\partial u}{\partial x}\right) dx + \frac{\partial u}{\partial y}dy + \frac{\partial u}{\partial z}dz \ , \\ dy' &= \frac{\partial v}{\partial x}dx + \left(1 + \frac{\partial v}{\partial y}\right) dy + \frac{\partial v}{\partial z}dz \ , \\ dz' &= \frac{\partial w}{\partial x}dx + \frac{\partial w}{\partial y}dy + \left(1 + \frac{\partial w}{\partial z}\right) dz \ , \end{aligned} \tag{2.83}$$

which lead to the definition of the *deformation gradient* as the following matrix:

$$[\,F_d\,] = [\,I\,] + [\,H_\eta\,] = \begin{bmatrix} \left(1 + \dfrac{\partial u}{\partial x}\right) & \dfrac{\partial u}{\partial y} & \dfrac{\partial u}{\partial z} \\ \dfrac{\partial v}{\partial x} & \left(1 + \dfrac{\partial v}{\partial y}\right) & \dfrac{\partial v}{\partial z} \\ \dfrac{\partial w}{\partial x} & \dfrac{\partial w}{\partial y} & \left(1 + \dfrac{\partial w}{\partial z}\right) \end{bmatrix} \ . \tag{2.84}$$

Matrix $\left[\,H_\eta\,\right]$ in (2.84) is called *displacement gradient.*

Through the deformation gradient, equations (2.83) can be recast in the following compact notation:

$$\overline{dr'} = [\,F_d\,]\,\overline{dr}\ . \tag{2.85}$$

If vector $\overline{\eta}$ describes, for each point of the considered body, the transformation from the initial configuration $\mathscr{C}_0$ to the final one $\mathscr{C}$, informations about the deformative state of the body can be also deduced from the change in the relative distance between points A and B before and after the transformation.

In $\mathscr{C}_0$ the initial infinitesimal distance between A and B can be written as follows:

$$dl_0^2 = (x_B - x_A)^2 + (y_B - y_A)^2 + (z_B - z_A)^2 = \overline{dr}^T\overline{dr}\ , \tag{2.86}$$

whereas, in $\mathscr{C}$ it results:

$$dl^2 = \left(x'_B - x'_A\right)^2 + \left(y'_B - y'_A\right)^2 + \left(z'_B - z'_A\right)^2 = \overline{dr'}^T\overline{dr'}\ . \tag{2.87}$$

By considering (2.85), the change in the distance of the two considered point can be expressed as follows:

$$\begin{aligned} dl^2 - dl_0^2 &= \overline{dr'}^T\overline{dr'} - \overline{dr}^T\overline{dr} \\ &= \left(\left[\,F_d\,\right]\overline{dr}\right)^T\left[\,F_d\,\right]\overline{dr} - \overline{dr}^T\overline{dr} \\ &= [dr]^T\,\overline{F}_d^T\,[\,F_d\,]\,\overline{dr} - \overline{dr}^T\overline{dr} \\ &= \overline{dr}^T\left([\,F_d\,]^T\,[\,F_d\,] - [\,I\,]\right)\overline{dr} \\ &= 2\overline{dr}^T\,[\,E\,]\,\overline{dr}\ , \end{aligned} \tag{2.88}$$

where tensor $[\,E\,]$ defines the *Green-Lagrange deformation* tensor (20):

$$[\,E\,] = \frac{1}{2}\left([\,F_d\,]^T\,[\,F_d\,] - [\,I\,]\right) \tag{2.89}$$

By considering (2.84), the Green-Lagrange tensor can be rewritten as follows:

$$\begin{aligned} [\,E\,] &= \frac{1}{2}\left(([\,I\,] + [\,H_\eta\,])^T\,([\,I\,] + [\,H_\eta\,]) - [\,I\,]\right) \\ &= \frac{1}{2}\left([\,H_\eta\,] + [\,H_\eta\,]^T\right) + \frac{1}{2}\,[\,H_\eta\,]^T\,[\,H_\eta\,]\ . \end{aligned} \tag{2.90}$$

With reference to the right-hand side of equation (2.90), it can be seen that tensor $[\,E\,]$ consists in two terms: the first one accounts for small deformations (case 1); the second one accounts for large deformations (case 2).

Now, it is observed that for case 1 a further simplification is possible, leading to the definition of the small strain tensor $[\,\epsilon\,]$:

$$[\,E\,] \approx \frac{1}{2}\left([\,H_\eta\,] + \left([\,H_\eta\,]^T\right)\right) = \begin{bmatrix} \dfrac{\partial u}{\partial x} & \dfrac{1}{2}\left(\dfrac{\partial v}{\partial x} + \dfrac{\partial u}{\partial y}\right) & \dfrac{1}{2}\left(\dfrac{\partial w}{\partial x} + \dfrac{\partial u}{\partial z}\right) \\ \dfrac{1}{2}\left(\dfrac{\partial u}{\partial y} + \dfrac{\partial v}{\partial x}\right) & \dfrac{\partial v}{\partial y} & \dfrac{1}{2}\left(\dfrac{\partial w}{\partial y} + \dfrac{\partial v}{\partial z}\right) \\ \dfrac{1}{2}\left(\dfrac{\partial u}{\partial z} + \dfrac{\partial w}{\partial x}\right) & \dfrac{1}{2}\left(\dfrac{\partial v}{\partial z} + \dfrac{\partial w}{\partial y}\right) & \dfrac{\partial w}{\partial z} \end{bmatrix} = [\,\epsilon\,] \ . \tag{2.91}$$

By introducing the Vogit's notation and employing symmetry properties, the deformation tensor $[\,\epsilon\,]$:

$$[\,\epsilon\,] = \begin{bmatrix} \epsilon_{xx} & \frac{1}{2}\epsilon_{xy} & \frac{1}{2}\epsilon_{xz} \\ \frac{1}{2}\epsilon_{yx} & \epsilon_{yy} & \frac{1}{2}\epsilon_{yz} \\ \frac{1}{2}\epsilon_{zx} & \frac{1}{2}\epsilon_{zy} & \epsilon_{zz} \end{bmatrix} = \begin{bmatrix} \epsilon_{11} & \frac{1}{2}\epsilon_{12} & \frac{1}{2}\epsilon_{13} \\ \frac{1}{2}\epsilon_{21} & \epsilon_{22} & \frac{1}{2}\epsilon_{23} \\ \frac{1}{2}\epsilon_{31} & \frac{1}{2}\epsilon_{32} & \epsilon_{33} \end{bmatrix} \tag{2.92}$$

can be expressed in a vectorial form:

$$\overline{\epsilon} = \begin{bmatrix} \epsilon_{xx} \\ \epsilon_{yy} \\ \epsilon_{zz} \\ \epsilon_{yz} \\ \epsilon_{xz} \\ \epsilon_{xy} \end{bmatrix} = \begin{bmatrix} \epsilon_{11} \\ \epsilon_{22} \\ \epsilon_{33} \\ \epsilon_{23} \\ \epsilon_{13} \\ \epsilon_{12} \end{bmatrix} . \tag{2.93}$$

The relationship between linear strains and relative displacements can be derived from (2.91):

$$\begin{gathered} \epsilon_{xx} = \frac{\partial u}{\partial x}, \qquad \varepsilon_{yy} = \frac{\partial v}{\partial y}, \qquad \epsilon_{zz} = \frac{\partial w}{\partial z}, \\ \epsilon_{yz} = \frac{\partial w}{\partial y} + \frac{\partial v}{\partial z}, \qquad \epsilon_{xz} = \frac{\partial w}{\partial x} + \frac{\partial u}{\partial z}, \qquad \epsilon_{xy} = \frac{\partial v}{\partial x} + \frac{\partial u}{\partial y} \ . \end{gathered} \tag{2.94}$$

which, in a compact form can be recast as follows:

$$\overline{\epsilon} = [\,\partial\,]\,\overline{\eta} \ . \tag{2.95}$$

2.3 Thermodynamic framework

2.3.1 Internal energy

The first and second laws of thermodynamics for closed systems are summarized in the following:

$$\mathrm{d}U = \delta W + \delta Q \ , \tag{2.96}$$

$$\mathrm{d}S = \frac{\delta Q}{T} + \delta S_i \ , \quad \delta S_i \geq 0 \ . \tag{2.97}$$

Quantities U and S represent system internal energy and entropy, respectively, and are state functions (i.e., they depend only on the current system state, and not on previous history). This is denoted by the fact that their changes are exact integrals, denoted as $\mathrm{d}U$ and $\mathrm{d}S$. Quantities δW and δQ are incremental work and heat exchanged between system and environment, with the convention that they are positive when entering the system and negative when being extracted by the system. Term δS_i represents the incremental irreversible entropy production, which is always nonnegative, and accounts for all dissipative phenomena occurring in the system, i.e., friction or electrical resistances which convert work into heat in an irreversible way. Macroscopic increment in work, heat, and irreversible entropy production between two generic states x_0 and x_1 can be computed as follows:

$$\begin{aligned} W(x_1) - W(x_0) &= \int_{x_0}^{x_1} \delta W \ , \\ Q(x_1) - Q(x_0) &= \int_{x_0}^{x_1} \delta Q \ , \\ S_i(x_1) - S_i(x_0) &= \int_{x_0}^{x_1} \delta S_i \ , \end{aligned} \tag{2.98}$$

for any $x_0(t_0)$ and $x_1(t_1)$ such that $t_1 \geq t_0$. Differently from U and S, W, Q, and S_i are not state functions, and depend on the particular trajectory of the system between x_0 and x_1. Finally, T is the system temperature, which is always a positive number.

By substituting (2.97) in (2.96), the following expression is obtained:

$$\mathrm{d}U = \delta W + T\mathrm{d}S - T\delta S_i \leq \delta W + T\mathrm{d}S \ , \quad \delta S_i \geq 0 \ , \tag{2.99}$$

and, for the ideal case in which no dissipations occur ($\delta S_i = 0$):

$$\mathrm{d}U = \delta W + T\mathrm{d}S \ , \quad \delta S_i = 0 \ . \tag{2.100}$$

Based in the nature of the work done on the system, general equations (2.99) and (2.100) can be better characterized. As an example, for the case of an electro-mechanical system two work contributions must be accounted: the mechanical work done by a force $\overline{F}$ causing a change in deformation $\delta\overline{\eta}$, and the electrostatic work done by voltage v causing a change in the charge q_e. Therefore:

$$\delta W = \overline{F}^T \delta\overline{\eta} + v\delta q_e \ . \tag{2.101}$$

Generally, the incremental work can be written as follows:

$$\delta W = \overline{e}^T \delta\overline{q} \ , \tag{2.102}$$

where $\overline{e}$ and $\overline{q}$ represent vectors of *effort* and *generalized displacement* variables, respectively. Efforts are normally intensive variables (i.e., they do not depend on the system size), whereas generalized displacements are extensive variables (i.e., they increase as the system size increases).

By replacing general expression (2.102) in (2.99) and (2.100), it is possible to recast the incremental internal energy as follows:

$$\mathrm{d}U = \overline{e}^T \delta\overline{q} + T\mathrm{d}S - T\delta S_i \leq \overline{e}^T \delta\overline{q} + T\mathrm{d}S \ , \quad \delta S_i \geq 0 \ , \tag{2.103}$$

$$\mathrm{d}U = \overline{e}^T \delta\overline{q} + T\mathrm{d}S \ , \quad \delta S_i = 0 \ , \tag{2.104}$$

for the irreversible and reversible case, respectively.

As a state function, U can be written as a function of *state variables*. With reference to the right-hand sides of both (2.103) and (2.104), these state variables are the ones appearing in the differentials terms. In order to highlight this dependence, we can rewrite U as follows:

$$U = U\left(\overline{q},\ S\right) \ . \tag{2.105}$$

The differential of (2.105) is given by the following expression:

$$\mathrm{d}U\left(\overline{q},\ S\right) = \left(\frac{\partial U}{\partial \overline{q}}\right)^T \delta\overline{q} + \frac{\partial U}{\partial S}\mathrm{d}S \ . \tag{2.106}$$

By substituting (2.106) in (2.103) and (2.104) and collecting terms relative to the same state variable differential, the following relations can be obtained:

$$\left(\frac{\partial U}{\partial \overline{q}} - \overline{e}\right)^T \delta\overline{q} + \left(\frac{\partial U}{\partial S} - T\right) \mathrm{d}S = -T\delta S_i \leq 0 \ , \quad \delta S_i \geq 0 \ , \tag{2.107}$$

$$\left(\frac{\partial U}{\partial \overline{q}} - \overline{e}\right)^T \delta\overline{q} + \left(\frac{\partial U}{\partial S} - T\right) \mathrm{d}S = 0 \ , \quad \delta S_i = 0 \ . \tag{2.108}$$

Once a function $U(\overline{q},\ S)$ has been chosen, it is possible to compute $\overline{e}$ and T as a function of $\overline{q}$ and S in such a way that relationships (2.107) and (2.108) hold for the irreversible and reversible cases, respectively. For the reversible case, a common choice consists of choosing $\overline{e}$ and T so that terms multiplying the differentials are canceled. Therefore, by choosing the following relations:

$$\begin{cases} \overline{e} = \frac{\partial U(\overline{q},\ S)}{\partial \overline{q}} \\ T = \frac{\partial U(\overline{q},\ S)}{\partial S} \end{cases} \ , \tag{2.109}$$

equation (2.108) is immediately satisfied. For the irreversible case (2.107), the left-hand side must be a non-positive, rather than zero. To let this be consistent, a typical choice is the following:

$$\begin{cases} \overline{e} = \frac{\partial U(\overline{q},\ S)}{\partial \overline{q}_j} + \overline{\zeta} \\ T = \frac{\partial U(\overline{q},\ S)}{\partial S} \end{cases} \ , \tag{2.110}$$

for some functions $\overline{\zeta} = (\zeta_1, ..., \zeta_N)^T$ to be defined. By replacing (2.110) in (2.107), it results:

$$\overline{\zeta}^T \delta\overline{q} = T\delta S_i \geq 0 \ . \tag{2.111}$$

Functions $\overline{\zeta}$ are then chosen in such a way the left-hand side of (2.111) always holds. A conventional choice, although not general, consists in selecting these functions as damping terms depending on the time derivatives of generalized displacements, as follows:

$$\overline{\zeta} = [\,b\,]\dot{\overline{q}} \ , \tag{2.112}$$

where it as been denoted as $[\,b\,]$ a diagonal square matrix of positive constant coefficients. This is motivated by the fact that $\overline{\zeta}$ describes additional friction terms, which normally are proportional to time derivatives of generalized displacements

(e.g., generalized displacement is position, damping is proportional to velocity; generalized displacement is charge, damping is proportional to current). Choice (2.112), results in the following statement:

$$\left([\,b\,]\dot{\overline{q}}\right)^T \delta\overline{q} = T\delta S_i \geq 0 \ . \tag{2.113}$$

Finally, by dividing both terms of (2.113) by dt, it results:

$$\left([\,b\,]\dot{\overline{q}}\right)^T \dot{\overline{q}} = \dot{\overline{q}}^T [\,b\,]^T \dot{\overline{q}} = T\dot{S}_i \geq 0 \ , \tag{2.114}$$

which always holds, since $\dot{\overline{q}}^T [\,b\,]^T \dot{\overline{q}}$ is a quadratic form. This is in agreement with physics, in which irreversible entropy production, related to dissipation, is often proportional to the square of derivatives of generalized displacements (e.g., mechanical viscous dissipations are proportional to the square of velocity, electrical Joule dissipations are proportional to the square of the current). Finally, note that at equilibrium conditions all time derivatives are zero, including also $\dot{\overline{q}}$. Therefore, at equilibrium, the irreversible model (2.110)coincides with the reversible one (2.109). In general, every choice of functions $\overline{\zeta}$ must satisfy the fact that $\overline{\zeta} = \overline{0}$ at equilibrium. This implies that no irreversible entropy is produced at equilibrium, thus no dissipations occurs.

2.3.2 Helmholtz free energy

One limitation of the above theory is that it relies on a thermodynamic potential U that is expressed as a function of S. This might be a limitation, since S is not a measurable quantity. The employed derivative rule would be way more effective on a different energy function, depending on T - which is easily measurable, instead of S. In order to address this issue, the following thermodynamical potential, denoted as Helmholtz free energy, has been introduced:

$$\Psi = U - TS \ . \tag{2.115}$$

Mathematically, (2.115) is called a Legendre transformation. Note that Ψ is a state function, since it is obtained as a combination of state functions. By differentiating (2.115), we obtain:

$$\Psi = \mathrm{d}U - S\mathrm{d}T - T\mathrm{d}S \ . \tag{2.116}$$

By substituting (2.116) in (2.99) and (2.100), it results:

$$\mathrm{d}\Psi = \overline{e}^T \delta\overline{q} - S\mathrm{d}T - T\delta S_i \leq \overline{e}^T \delta\overline{q} - S\mathrm{d}T \ , \quad \delta S_i \geq 0 \ , \tag{2.117}$$

$$\mathrm{d}\Psi = \overline{e}^T \delta\overline{q} - S\mathrm{d}T \ , \quad \delta S_i = 0 \ . \tag{2.118}$$

Note that, if we work with Ψ rather than U, the term proportional to $\mathrm{d}S$ has now become proportional to $\mathrm{d}T$. This fact suggest that the Helmholtz free energy can be chosen as a function of $\overline{q}$ and T:

$$\Psi = \Psi\left(\overline{q},\ T\right) \ . \tag{2.119}$$

As a consequence:

$$\mathrm{d}\Psi = \left(\frac{\partial\Psi}{\partial\overline{q}}\right)^T \delta\overline{q} + \frac{\partial\Psi}{\partial T}\mathrm{d}T \ . \tag{2.120}$$

By replacing (2.120) in (2.117) and (2.118), it can be obtained:

$$\left(\frac{\partial\Psi}{\partial\overline{q}} - \overline{e}\right)^T \delta\overline{q} + \left(\frac{\partial\Psi}{\partial T} + S\right)\mathrm{d}T = -T\delta S_i \leq 0 \ , \quad \delta S_i \geq 0 \ , \tag{2.121}$$

$$\left(\frac{\partial\Psi}{\partial\overline{q}} - \overline{e}\right)^T \delta\overline{q} + \left(\frac{\partial\Psi}{\partial T} + S\right)\mathrm{d}T = 0 \ , \quad \delta S_i = 0 \ . \tag{2.122}$$

Therefore, it results that a possible choice to let (2.122) hold is:

$$\begin{cases} \overline{e} = \frac{\partial\Psi(\overline{q},\ T)}{\partial\overline{q}} \\ S = -\frac{\partial\Psi(\overline{q},\ T)}{\partial T} \end{cases} \ , \tag{2.123}$$

whereas for the irreversible case (2.121) it can be chosen what follows:

$$\begin{cases} \overline{e} = \frac{\partial\Psi(\overline{q},\ T)}{\partial\overline{q}} + \overline{\zeta} \\ S = -\frac{\partial\Psi(\overline{q},\ T)}{\partial T} \end{cases} \ , \tag{2.124}$$

provided that $\overline{\zeta}$ are chosen so that the following inequality holds:

$$\overline{\zeta}^T \delta\overline{q} = T\delta S_i \geq 0 \ . \tag{2.125}$$

It is worth to stress that the major advantages of (2.123)-(2.124) is that Ψ depends on $\overline{q}$ and T, which are all measurable variables, therefore it can be constructed from experiments. Once Ψ is known, S and $\overline{e}$ can be computed, and eventually U can be reconstructed by inverting equation (2.115).

It must be noted that equations (2.117)-(2.118)become particularly relevant for isothermal processes, in which T is constant. This case commonly occurs in electromechanical systems in which thermal dynamics can be neglected. Under this assumption, $\mathrm{d}T = 0$, therefore (2.117)-(2.118) can be rewritten as:

$$\mathrm{d}\Psi = \overline{e}^T \delta\overline{q} - T\delta S_i \leq \overline{e}^T \delta\overline{q} \ , \quad \delta S_i \geq 0 \ , \tag{2.126}$$

$$\mathrm{d}\Psi = \overline{e}^T \delta\overline{q} \ , \quad \delta S_i = 0 \ . \tag{2.127}$$

Equations (2.126)-(2.127) have a very interesting interpretation. In particular, in the reversible case (2.127), it can be seen that the change in Helmholtz free energy equals the work done on the system. As a consequence, all the work is stored as Helmholtz free energy. This means that the maximum amount of work that can be extracted from the system coincides exactly with the Helmholtz free energy previously stored. In the irreversible case (2.126), on the other hand, the energy is non-larger than the work done on the system. This means that part of the work performed on the system is stored as Helmholtz free-energy, and part is dissipated through heat, resulting in an irreversible entropy production. Therefore, in the attempt to extract some work from the system, only part of it can be recovered as a useful work, while some of it will be irreversibly lost due to friction phenomena. The Helmholtz free energy represents then a means to quantify the useful energy in a system, i.e., the maximum amount that can be extracted in the form of work, in the isothermal case.

2.3.3 Gibbs free energy

By using a reasoning similar to the one which led to Helmholtz free energy density, it is also possible to define other thermodynamic potentials via more involved Legendre transformations. One example is the following one:

$$G = U - TS - \overline{e}^T \overline{q} = \Psi - \overline{e}^T \overline{q} \ , \tag{2.128}$$

which is clearly a state function. The differential of the Gibbs free energy is given by the following expression:

$$\mathrm{d}G = \mathrm{d}U - T\mathrm{d}S - S\mathrm{d}T - \overline{e}^T \mathrm{d}\overline{q} - \overline{q}^T \mathrm{d}\overline{e} = \mathrm{d}\Psi - \overline{e}^T \mathrm{d}\overline{q} - \overline{q}^T \mathrm{d}\overline{e} \ . \tag{2.129}$$

By replacing (2.129) in (2.103)-(2.104), it results:

$$\mathrm{d}G = -\overline{q}^T \delta\overline{e} - S\mathrm{d}T - T\delta S \leq -\overline{q}^T \delta\overline{e} - S\mathrm{d}T \ , \quad \delta S_i \geq 0 \ , \tag{2.130}$$

$$\mathrm{d}G = -\overline{q}^T \delta\overline{e} - S\mathrm{d}T \ , \quad \delta S_i = 0 \ . \tag{2.131}$$

Equations (2.130)-(2.131) suggest that G can be written as a function of $\overline{e}$ and T, as follows:

$$G = G\left(\overline{e},\ T\right) \ , \tag{2.132}$$

Therefore:

$$\mathrm{d}G = \left(\frac{\partial G}{\partial \overline{e}}\right)^T \delta\overline{e} + \frac{\partial G}{\partial T}\mathrm{d}T \ . \tag{2.133}$$

By replacing (2.133) in (2.130)-(2.131), it results:

$$\left(\frac{\partial G}{\partial \overline{e}} - \overline{q}\right)^T \delta\overline{e} + \left(\frac{\partial G}{\partial T} + S\right)\mathrm{d}T = -T\delta S_i \leq 0 \ , \quad \delta S_i \geq 0 \ , \tag{2.134}$$

$$\left(\frac{\partial G}{\partial \overline{e}} - \overline{q}\right)^T \delta\overline{e} + \left(\frac{\partial G}{\partial T} + S\right)\mathrm{d}T = 0 \ , \quad \delta S_i = 0 \ . \tag{2.135}$$

A possible choice to let (2.134) hold is:

$$\begin{cases} \overline{q} = -\frac{\partial G(\overline{e},\ T)}{\partial \overline{e}} \\ S = -\frac{\partial G(\overline{e},\ T)}{\partial T} \end{cases} \ , \tag{2.136}$$

whereas for (2.135) it is possible to choose:

$$\begin{cases} \overline{q} = -\frac{\partial G(\overline{e},\ T)}{\partial \overline{e}} - \overline{\zeta} \\ S = -\frac{\partial G(\overline{e},\ T)}{\partial T} \end{cases} \ , \tag{2.137}$$

provided that functions $\overline{\zeta}$ are chosen in such a way that the following inequality holds:

$$\overline{\zeta}^T \delta\overline{e} = T\delta S_i \geq 0 \ . \tag{2.138}$$

Potential G appears as a convenient choice for the cases in which the energy is more conveniently expressed as a function of efforts, rather than generalized displacements. This might be the case, for instance, for an elastic energy expressed as a function of a force rather than a deformation or an electrostatic energy expressed

as a function of a voltage rather than a charge. Potential G appears as useful for systems in which we can control the efforts and keep them constant, e.g., constant force, constant voltage, etc. This is in general easier than keeping the generalized displacements constant. In fact, in this case, it results $\mathrm{d}\overline{e} = \overline{0}$. If, in addition, also the temperature is kept as constant, $\mathrm{d}T = 0$. This implies that (2.130)-(2.131) can be written as follows:

$$\mathrm{d}G = -T\delta S_i \leq 0 \ , \quad \delta S_i \geq 0 \ , \tag{2.139}$$

$$\mathrm{d}G = 0 \ , \quad \delta S_i = 0 \ . \tag{2.140}$$

Therefore, if the efforts and the temperature are constant, potential G decreases for irreversible systems, and remains constant for reversible systems. In general, since $\mathrm{d}S_i$ is zero at equilibrium, G decreases until an equilibrium state is reached, and then remains constant. Since in general it is easier to keep efforts constant than generalized displacements, G appears as more suitable to study convergence to equilibrium of systems with fixed boundary conditions, since in this case an equilibrium state can be simply stated as a minimum of G.

2.3.4 From free energy to free energy density

Let now consider equation (2.127) - valid for isothermal and reversible systems - and specialize it for an electro-mechanical system like the one depicted in Fig. 2.2. System consists of a block of an electro-active material with initial geometry L_1, L_2, L_3. In order to simplify the discussion, we assume the elastic and electric behavior of the system as unidirectional, in the range of small deformations. A vertical force $\overline{F} = [0, 0, F_3]^T$ acts on the system, as depicted in Fig. 2.2, producing a strain ϵ_3 along the same direction. Moreover, it is assumed that the only non-null component of the electric field in the space occupied by the material block is directed along axis 3 ($\overline{E} = [0, 0, E_3]^T$). Voltage v is measured between the electrodes. A free charge q_e is distributed on the electrodes with density $\sigma_e = D_3$.

With reference to the considered system, the Helmholtz free energy differential can be written as follows:

$$\mathrm{d}\Psi = F_3\delta l_3 + v\delta q_e \ . \tag{2.141}$$

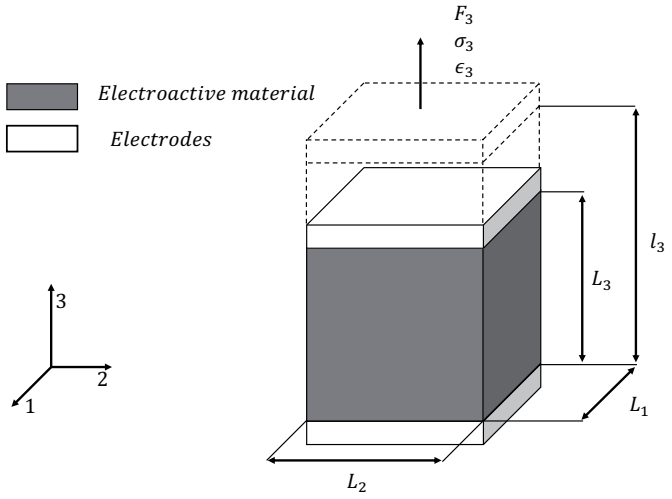

Figure 2.2: Electromechanical system consisting of an active material with electrodes applied. Initial block geometry is characterized by sides L_1, L_2, L_3. Voltage v is applied between he electrodes. Free charge q_e is distributed on the electrodes, with density $\sigma_e = D_3$.

By dividing the Helmholtz free energy by the volume (Vol), it is possible to obtain the Helmholtz free energy density ψ:

$$\psi = \frac{\Psi}{Vol} \ . \tag{2.142}$$

Under the assumption of small deformations, by dividing both sides of (2.141) by volume $L_1 L_2 L_3$, and by defining the following quantities:

$$\begin{aligned} \epsilon_3 &= \frac{l_3 - L_3}{L_3} \ , \\ \sigma_3 &= \frac{F_3}{L_1 L_2} \ , \\ \sigma_e &= \frac{q_e}{L_1 L_2} \ , \\ E_3 &= \frac{v}{L_3} \ , \end{aligned} \tag{2.143}$$

it is possible to write the differential of ψ as follows:

$$\mathrm{d}\psi = \sigma_3 \delta\epsilon_3 + E_3 \delta\sigma_e \ . \tag{2.144}$$

Therefore, if ψ is parametrized as a function of strain and charge density:

$$\psi = \psi\left(\epsilon_3, \sigma_e\right) \ , \tag{2.145}$$

by differentiating ψ it results:

$$\mathrm{d}\psi = \frac{\partial \psi}{\partial \epsilon_3}\delta\epsilon_3 + \frac{\partial \psi}{\partial \sigma_e}\delta\sigma_e \ . \tag{2.146}$$

By substituting (2.146) in (2.144), it resutls:

$$\left(\frac{\partial \psi}{\partial \epsilon_3} - \sigma_3\right)\delta\epsilon_3 + \left(\frac{\partial \psi}{\partial \sigma_e} - E_3\right)\delta\sigma_e = 0 \ . \tag{2.147}$$

Therefore, mechanical stress and electric field can be evaluated as follows:

$$\begin{cases} \sigma_3 = \frac{\partial \psi}{\partial \epsilon_3} \\ E_3 = \frac{\partial \psi}{\partial \sigma_e} \end{cases} \ . \tag{2.148}$$

Working with quantities normalized with respect to geometry, such as free energy density, strain, stress, electrical displacement, and electric field is commonly done when working with smart material applications. This requires that the Helmholtz free energy density is explicitly reparametrized as a function of the normalized intensive variables. The same reasoning can be applied to any thermodynamic potential, depending on the most convenient choice of coordinates to describe a system. Of course, the same holds true for any other thermodynamic potential, which can be normalized with respect to volume to obtain the corresponding energy density. The work and heat terms on the right-hand side of the equations are normalized accordingly.

The generalization form of (2.144) to the non-isothermal, multi-directional case assumes the following expression:

$$\mathrm{d}\psi = \overline{\sigma}^T \delta\overline{\epsilon} + \overline{E}^T \delta\overline{D} - s\mathrm{d}T \ , \tag{2.149}$$

where it as been employed the Vogit vectorial form for both stress and strain tensors and $s = \frac{S}{Vol}$.

2.3.5 Electric enthalpy density

In previous subsections, a summary on thermodynamic state functions as been reported, with the aim of presenting the general framework in which modeling techniques for systems based on smart materials have been developed. We have seen how constitutive relations can be derived starting from the choice of an opportunely parametrized thermodynamic potential, in case of both conservative and non-conservative systems.

In order to describe the thermo-electric evolution of a system based on piezoelectric materials, a useful choice in terms of thermodynamic potential is represented by the following state function density:

$$g' = \psi - \overline{E}^T \overline{D} \ . \tag{2.150}$$

The differential of g' can be evaluated as follows:

$$\mathrm{d}g' = \mathrm{d}\psi - \overline{E}^T \delta\overline{D} - \overline{D}^T \delta\overline{E} \ . \tag{2.151}$$

By substituting (2.149) in (2.151), it results:

$$\mathrm{d}g' = \overline{\sigma}^T \delta\overline{\epsilon} - \overline{D}\delta\overline{E} - s\mathrm{d}T \ , \tag{2.152}$$

from which results that g' has been parametrized with respect to strain, electric field and temperature. Under the assumption of isothermal systems ($\mathrm{d}T = 0$), equation (2.152) assumes the following form:

$$\mathrm{d}g' = \mathrm{d}h = \overline{\sigma}^T \delta\overline{\epsilon} - \overline{D}\delta\overline{E} \ , \tag{2.153}$$

which defines the differential of another thermodynamic potential, known as *electric enthalpy* density h:

$$h = u - \overline{E}^T \overline{D} \ . \tag{2.154}$$

In (2.154), quantity u denotes the internal energy density of the system.

Since h has been parametrized with respect to the stress tensor and the electric field, it results that:

$$\mathrm{d}h = \left(\frac{\partial h}{\partial \overline{\epsilon}}\right)^T \delta\overline{\epsilon} + \left(\frac{\partial h}{\partial \overline{E}}\right)^T \delta\overline{E} \ , \tag{2.155}$$

which, considering the Vogit vectorial form of the stress tensor, can be written in the extended form as follows:

$$\begin{aligned} \mathrm{d}h = \quad & \frac{\partial h}{\partial \epsilon_{11}}\delta\epsilon_{11} + \frac{\partial h}{\partial \epsilon_{22}}\delta\epsilon_{22} + \frac{\partial h}{\partial \epsilon_{33}}\delta\epsilon_{33} \\ & + \frac{\partial h}{\partial \epsilon_{23}}\delta\epsilon_{23} + \frac{\partial h}{\partial \epsilon_{13}}\delta\epsilon_{13} + \frac{\partial h}{\partial \epsilon_{12}}\delta\epsilon_{12} \\ & + \frac{\partial h}{\partial E_1}\delta E_1 + \frac{\partial h}{\partial E_2}\delta E_2 + \frac{\partial h}{\partial E_3}\delta E_3 \ . \end{aligned} \tag{2.156}$$

By comparing (2.155) with (2.153), it results that:

$$\begin{cases} \sigma_{ij} = \dfrac{\partial h}{\partial \epsilon_{ij}} \ , \\ D_r = -\dfrac{\partial h}{\partial E_r} \ . \end{cases} \tag{2.157}$$

Equations (2.157) can be recast, in a more compact form, as follows:

$$\begin{cases} \overline{\sigma} = \dfrac{\partial h}{\partial \overline{\epsilon}} \ , \\ \overline{D} = -\dfrac{\partial h}{\partial \overline{E}} \ . \end{cases} \tag{2.158}$$

Equations (2.158) suggest for h the role of thermodynamic potential from which obtain, through the derivative rule, the stress tensor and the electric displacement vector.

2.4 Linear Piezoelasticity

2.4.1 Series development for the electric enthalpy density

In the previous subsection we introduced the electric enthalpy density function (h) for an electromechanical system. Function h has been parametrized with reference to the stress tensor ($\overline{\epsilon}$) and the electric field vector ($\overline{E}$):

$$h = h\left(\epsilon_{11}, \epsilon_{22}, \epsilon_{33}, \epsilon_{23}, \epsilon_{13}, \epsilon_{12}, E_1, E_2, E_3\right) \ . \tag{2.159}$$

The Maclaurin series development of h about the origin, i.e. about the initial undeformed configuration of the considered system, with null electric field:

$$\begin{aligned} \overline{\epsilon}_0 &= [0,0,0,0,0,0]^T \ , \\ \overline{E}_0 &= [0,0,0]^T \ , \end{aligned} \tag{2.160}$$

takes the form reported in the following:

$$\begin{aligned} h = {} & h(0,0) + \left.\frac{\partial h}{\partial \epsilon_{11}}\right|_{(0,0)} \epsilon_{11} + \left.\frac{\partial h}{\partial \epsilon_{22}}\right|_{(0,0)} \epsilon_{22} + \left.\frac{\partial h}{\partial \epsilon_{33}}\right|_{(0,0)} \epsilon_{33} \\ & + \left.\frac{\partial h}{\partial \epsilon_{23}}\right|_{(0,0)} \epsilon_{23} + \left.\frac{\partial h}{\partial \epsilon_{13}}\right|_{(0,0)} \epsilon_{13} + \left.\frac{\partial h}{\partial \epsilon_{12}}\right|_{(0,0)} \epsilon_{12} \\ & + \left.\frac{\partial h}{\partial E_1}\right|_{(0,0)} E_1 + \left.\frac{\partial h}{\partial E_2}\right|_{(0,0)} E_2 + \left.\frac{\partial h}{\partial E_3}\right|_{(0,0)} E_3 \\ & + \frac{1}{2}\left(\left.\frac{\partial h}{\partial \epsilon_{11}}\right|_{(0,0)} \epsilon_{11} + \left.\frac{\partial H}{\partial \epsilon_{22}}\right|_{(0,0)} \epsilon_{22} + \left.\frac{\partial H}{\partial \epsilon_{33}}\right|_{(0,0)} \epsilon_{33} \right. \\ & + \left.\frac{\partial H}{\partial \epsilon_{23}}\right|_{(0,0)} \epsilon_{23} + \left.\frac{\partial H}{\partial \epsilon_{13}}\right|_{(0,0)} \epsilon_{13} + \left.\frac{\partial H}{\partial \epsilon_{12}}\right|_{(0,0)} \epsilon_{12} \\ & \left. + \left.\frac{\partial H}{\partial E_1}\right|_{(0,0)} E_1 + \left.\frac{\partial H}{\partial E_2}\right|_{(0,0)} E_2 + \left.\frac{\partial H}{\partial E_3}\right|_{(0,0)} E_3 \right)^{(2)} + \dots \end{aligned} , \tag{2.161}$$

where the symbolic power represents the second order derivative operator. Under the assumption of sufficiently small deformations and low electric field, it is possible to neglect terms of order higher than two in (2.161), without this resulting in significant errors.

Since, as clarified in previous sections, components of both stress tensor and electric field can be deduced by derivatives of h, we can safely assume a constant null value for h in the origin. Therefore:

$$h\,(0,0) = 0\ . \tag{2.162}$$

Moreover, first order terms in (2.161) represent stress tensor components and electric displacement components, which can be considered equal to zero in the

origin:

$$\begin{aligned}
\left.\frac{\partial h}{\partial \epsilon_{11}}\right|_{(0,0)} &= \sigma_{m_{11}}(0,0) = 0 \ , \\
\left.\frac{\partial h}{\partial \epsilon_{22}}\right|_{(0,0)} &= \sigma_{m_{22}}(0,0) = 0 \ , \\
\left.\frac{\partial h}{\partial \epsilon_{33}}\right|_{(0,0)} &= \sigma_{m_{33}}(0,0) = 0 \ , \\
\left.\frac{\partial h}{\partial \epsilon_{23}}\right|_{(0,0)} &= \sigma_{m_{23}}(0,0) = 0 \ , \\
\left.\frac{\partial h}{\partial \epsilon_{13}}\right|_{(0,0)} &= \sigma_{m_{13}}(0,0) = 0 \ , \\
\left.\frac{\partial h}{\partial \epsilon_{12}}\right|_{(0,0)} &= \sigma_{m_{12}}(0,0) = 0 \ , \\
-\left.\frac{\partial h}{\partial E_1}\right|_{(0,0)} &= D_1(0,0) = 0 \ , \\
-\left.\frac{\partial h}{\partial E_2}\right|_{(0,0)} &= D_2(0,0) = 0 \ , \\
-\left.\frac{\partial h}{\partial E_3}\right|_{(0,0)} &= D_3(0,0) = 0 \ .
\end{aligned} \tag{2.163}$$

By considering (2.162) and (2.163), ignoring terms of order higher than two and developing the symbolic power, equation (2.161) reduces to:

$$\begin{aligned}
h = \frac{1}{2}\Bigg(& \left.\frac{\partial^2 h}{\partial \epsilon_{11}^2}\right|_{(0,0)} \epsilon_{11}^2 + \left.\frac{\partial^2 h}{\partial \epsilon_{22}^2}\right|_{(0,0)} \epsilon_{22}^2 + \cdots + \left.\frac{\partial^2 h}{\partial E_3^2}\right|_{(0,0)} E_3^2 \\
& + 2\left.\frac{\partial^2 h}{\partial \epsilon_{11}\partial \epsilon_{22}}\right|_{(0,0)} \epsilon_{11}\epsilon_{22} + 2\left.\frac{\partial^2 H}{\partial \epsilon_{11}\partial \epsilon_{33}}\right|_{(0,0)} \epsilon_{11}\epsilon_{33} + \dots \\
& + 2\left.\frac{\partial^2 h}{\partial \epsilon_{12}\partial E_1}\right|_{(0,0)} \epsilon_{12}E_1 + 2\left.\frac{\partial^2 h}{\partial \epsilon_{12}\partial E_2}\right|_{(0,0)} \epsilon_{12}E_2 + 2\left.\frac{\partial^2 H}{\partial \epsilon_{12}\partial E_3}\right|_{(0,0)} \epsilon_{12}E_3 \\
& + 2\left.\frac{\partial^2 H}{\partial E_1\partial E_2}\right|_{(0,0)} E_1E_2 + 2\left.\frac{\partial^2 H}{\partial E_1\partial E_3}\right|_{(0,0)} E_1E_3 + 2\left.\frac{\partial^2 h}{\partial E_2\partial E_3}\right|_{(0,0)} E_2E_3\Bigg)
\end{aligned} \ . \tag{2.164}$$

Equation (2.164) consists of:

- six terms in the following form:

$$\left.\frac{\partial^2 h}{\partial E_i \partial E_j}\right|_{(0,0)} E_iE_j \ . \tag{2.165}$$

Mixed partial derivatives in (2.165) are given by:

$$\frac{\partial^2 h}{\partial E_i \partial E_j} = \frac{\partial}{\partial E_i}\left(\frac{\partial h}{\partial E_j}\right) = -\frac{\partial D_j}{\partial E_i} = \varepsilon_{ij} \ , \tag{2.166}$$

where coefficients ε_{ij} has the dimension of an electrical permittivity. They can be collected in a tensor that, in compact notation[1], can be written as follows:

$$\left[\varepsilon\right] = \begin{bmatrix} h^{(2)}_{,1} & h^{(2)}_{,1,2} & h^{(2)}_{,1,3} \\ h^{(2)}_{,2,1} & h^{(2)}_{,2} & h^{(2)}_{,2,3} \\ h^{(2)}_{,3,1} & h^{(2)}_{,3,2} & h^{(2)}_{,3} \end{bmatrix}_{(0,0)} \ . \tag{2.168}$$

Equation (2.168) identifies the tensor of *permittivity at constant strain*. Since for a generic function f, with second order partial derivatives continuous in a point x_0, the following statement is true:

$$\left.\frac{\partial^2 f}{\partial x_i \partial x_j}\right|_{x_0} = \left.\frac{\partial^2 f}{\partial x_j \partial x_i}\right|_{x_0} \ , \tag{2.169}$$

tensor $\left[\varepsilon\right]$ results to be symmetric, therefore only six components are needed to fully define it.

- eighteen terms in the form:

$$\left.2\frac{\partial^2 h}{\partial \epsilon_{ij} \partial E_k}\right|_{(0,0)} \varepsilon_{ij} E_k \ , \tag{2.170}$$

where mixed derivative can be expressed as follows:

$$\frac{\partial^2 h}{\partial \epsilon_{ij} \partial E_k} = \frac{\partial}{\partial \epsilon_{ij}}\left(\frac{\partial h}{\partial E_k}\right) = -\frac{\partial D_k}{\partial \epsilon_{ij}} = -d_{kij} \ . \tag{2.171}$$

Coefficients d_{ijk} defines a (3×6) tensor denoted as *piezoelectric coupling tensor*:

$$\left[d\right] = -\begin{bmatrix} h^{(2)}_{,11,1} & h^{(2)}_{,22,1} & h^{(2)}_{,33,1} & h^{(2)}_{,23,1} & h^{(2)}_{,13,1} & h^{(2)}_{,12,1} \\ h^{(2)}_{,11,2} & h^{(2)}_{,22,2} & h^{(2)}_{,33,2} & h^{(2)}_{,23,2} & h^{(2)}_{,13,2} & h^{(2)}_{,12,2} \\ h^{(2)}_{,11,3} & h^{(2)}_{,22,3} & h^{(2)}_{,33,3} & h^{(2)}_{,23,3} & h^{(2)}_{,13,3} & h^{(2)}_{,12,3} \end{bmatrix}_{(0,0)} \tag{2.172}$$

[1] In compact notation, the second derivative of a generic function f, with respect to generic variables x_i and x_j, is denoted by:

$$f^{(2)}_{,i,j} = \frac{\partial^2 f}{\partial x_i \partial x_j} \ . \tag{2.167}$$

- twenty one terms in the form:

$$c_{ijkl} = \frac{\partial^2 h}{\partial \epsilon_{ij} \partial \epsilon_{kl}} \epsilon_{ij} \epsilon_{kl} \ , \tag{2.173}$$

which defines the *stiffness tensor at constant electric field*:

$$\big[c\big] = \begin{bmatrix} h^{(2)}_{,11} & h^{(2)}_{,22,11} & h^{(2)}_{,33,11} & h^{(2)}_{,23,11} & h^{(2)}_{,13,11} & h^{(2)}_{,12,11} \\ h^{(2)}_{,11,22} & h^{(2)}_{,22} & h^{(2)}_{,33,22} & h^{(2)}_{,23,22} & h^{(2)}_{,13,22} & h^{(2)}_{,12,22} \\ h^{(2)}_{,11,33} & h^{(2)}_{,22,33} & h^{(2)}_{,33} & h^{(2)}_{,23,33} & h^{(2)}_{,13,33} & h^{(2)}_{,12,33} \\ h^{(2)}_{,11,23} & h^{(2)}_{,22,23} & h^{(2)}_{,33,23} & h^{(2)}_{,23} & h^{(2)}_{,13,23} & h^{(2)}_{,12,23} \\ h^{(2)}_{,11,13} & h^{(2)}_{,22,13} & h^{(2)}_{,33,13} & h^{(2)}_{,23,13} & h^{(2)}_{,13} & h^{(2)}_{,12,13} \\ h^{(2)}_{,11,12} & h^{(2)}_{,22,12} & h^{(2)}_{,33,12} & h^{(2)}_{,23,12} & h^{(2)}_{,13,12} & h^{(2)}_{,12} \end{bmatrix} . \tag{2.174}$$

Equation (2.164) reduces to a quadratic form consisting of forty five coefficients:

$$h = \epsilon_{ij}\epsilon_{kl} \frac{1}{2} \frac{\partial^2 h}{\partial \epsilon_{ij} \partial \epsilon_{kl}}\bigg|_{(0,0)} + E_i E_j \frac{1}{2} \frac{\partial^2 h}{\partial E_i \partial E_j}\bigg|_{(0,0)} + \epsilon_{ij} E_k \frac{\partial^2 h}{\partial \epsilon_{ij} \partial E_k}\bigg|_{(0,0)} . \tag{2.175}$$

By taking into account (2.166), (2.171), and (2.173), it is possible to recast (2.175) in the following form:

$$h = \frac{1}{2} \epsilon_{ij} \epsilon_{kl} c_{ijkl} - \frac{1}{2} E_i E_j \varepsilon_{ij} - \epsilon_{ij} E_k d_{kij} \ , \tag{2.176}$$

which, in compact form, results:

$$h = \frac{1}{2} \overline{\epsilon}^T \, [\, c \,] \, \overline{\epsilon} - \frac{1}{2} \overline{E}^T \, [\, \varepsilon \,] \, \overline{E} - \overline{E}^T \, [\, d \,] \, \overline{\epsilon} \ . \tag{2.177}$$

Equation (2.177) states that the electric enthalpy density h, for a linear piezoelastic system, consists in a term that accounts for elastic deformation at constant electric field; in a term accounting for electrostatic effects at constant strain; finally, in a third term representative of the electromechanical coupling within the material.

2.4.2 Linear constitutive equations

In the previous subsection we derived a compact form of the electric enthalpy density function for a linear piezoelastic system. Constitutive equations define stress $\overline{\sigma}$ and electric displacement $\overline{D}$ as a function of strain $\overline{\epsilon}$ and electric $\overline{E}$ fields. Since relations

(2.158) holds, through the derivation of (2.177), the following constitutive equations are obtained:

$$\begin{cases} \overline{\sigma} = [\,c\,]\,\overline{\epsilon} - [\,d\,]^T\overline{E} \\ \overline{D} \;\; = [\,d\,]\overline{\epsilon} + [\,\varepsilon\,]\,\overline{E} \end{cases} , \tag{2.178}$$

in which the coupling between fields describing the elastic and the electrostatic behavior of the considered system is made evident through the tensor $[\,d\,]$.

It is useful to report here the constitutive equations (2.178) expressed adopting the indicial notation. They result as follows:

$$\begin{cases} \sigma_{ij} = c_{ijkl}\epsilon_{kl} - E_k d_{kij} \\ D_r = E_r\varepsilon_{ir} + \epsilon_{ij}d_{rij} \end{cases} . \tag{2.179}$$

Equation set (2.178), which expresses both the stress tensor and the electric displacement vector as function of the independent variables $\overline{\epsilon}$ and $\overline{E}$, represent the *stress-charge* form of the constitutive equations. Depending on applications, it is useful to express constitutive equations as a function of other independent variables.

By pre-multiplying the second of (2.178) by $[\,\varepsilon\,]^{-1}$, it results:

$$\overline{E} = [\,\varepsilon\,]^{-1}\overline{D} - [\,\varepsilon\,]^{-1}[\,d\,]\overline{\epsilon}\;, \tag{2.180}$$

which can be substituted in the first of (2.178) in order to obtain:

$$\overline{\sigma} = \Big([\,c\,] - [\,d\,]^T[\,\varepsilon\,]^{-1}[\,d\,]\Big)\,\overline{\epsilon} - \big[\,d\,\big]^T\big[\,\varepsilon\,\big]^{-1}\overline{D}\;. \tag{2.181}$$

By denoting as:

$$[\,c\,]_{|\sigma E|} = \big[\,c\,\big] - \big[\,d\,\big]^T\big[\,\varepsilon\,\big]^{-1}\big[\,d\,\big]\;, \tag{2.182}$$

$$[\,d\,]_{|\sigma E|} = [\,\varepsilon\,]^{-1}\,[\,d\,]\;, \tag{2.183}$$

$$[\,\varepsilon\,]_{|\sigma E|} = [\,\varepsilon\,]^{-1}\;, \tag{2.184}$$

the following *stress-field* form of the constitutive equations is obtained:

$$\begin{cases} \overline{\sigma} = [\,c\,]_{|\sigma E|}\,\overline{\epsilon} - [\,d\,]^T_{|\sigma E|}\overline{D} \\ \overline{E} \;\; = -[\,d\,]_{|\sigma E|}\overline{\epsilon} + [\,\varepsilon\,]_{|\sigma E|}\,\overline{D} \end{cases} . \tag{2.185}$$

Through similar mathematical manipulations it is possible to obtain the other two forms of the constitutive equations. They are:

- the *strain-charge* form:

$$\begin{cases} \overline{\epsilon} = [\,s\,]_{|\epsilon D|}\,\overline{\sigma} + [\,d\,]^T_{|\epsilon D|}\overline{E} \\ \overline{D} \;\; = [\,d\,]_{|\epsilon D|}\overline{\sigma} + [\,\varepsilon\,]_{|\epsilon D|}\,\overline{E} \end{cases} , \tag{2.186}$$

where:

$$[\,s\,]_{|\epsilon D|} = \big[\,c\,\big]^{-1} \ , \tag{2.187}$$

$$[\,d\,]_{|\epsilon D|} = [\,d\,]\,[\,c\,]^{-1} \ , \tag{2.188}$$

$$[\,\varepsilon\,]_{|\epsilon D|} = [\,\varepsilon\,] + [\,d][\,c\,]^{-1}[\,d\,]^T \ . \tag{2.189}$$

- the *strain-field* form:

$$\begin{cases} \overline{\epsilon} = [\,s\,]_{|\epsilon E|}\,\overline{\sigma} - [\,d\,]^T_{|\epsilon E|}\overline{D} \\ \overline{E} \;\; = -[\,d\,]_{|\epsilon E|}\overline{\sigma} + [\,\varepsilon\,]_{|\epsilon E|}\,\overline{D} \end{cases} , \tag{2.190}$$

where:

$$[\,s\,]_{|\epsilon E|} = \Big(I - \big[\,c\,\big]^{-1}\,[\,d\,]^T[\,\varepsilon\,]^{-1}[\,d\,]\Big)^{-1} \ , \tag{2.191}$$

$$[\,d\,]_{|\epsilon E|} = [\,\varepsilon\,]^{-1}[\,d\,]\,[\,s\,]_{|\epsilon E|} \ , \tag{2.192}$$

$$[\,\varepsilon\,]_{|\epsilon E|} = [\,\varepsilon\,]^{-1} + [\,\varepsilon\,]^{-1}[\,d][\,s\,]_{\epsilon E}[\,d\,]^T[\,\epsilon\,]^{-1} \ . \tag{2.193}$$

2.4.3 Compact matrix notation

It is useful to introduce hereafter a different notation allowing to recast (2.179) in a more readable form. The compact notation, defined in (22), consists in substituting double indexes ij and kl with single indexes p and q, respectively. The correspondence between the two notations is reported in Table 2.1.

ij or kl:	11	22	33	23 or 32	13 or 31	12 or 21
p or q:	1	2	3	4	5	6

Table 2.1: Compact notation

In compact notation, the vectorial form of stress and strain tensors (equations (2.72) and (2.93), respectively) can be rewritten as follows:

$$\begin{aligned} \overline{\sigma} &= [\sigma_{11},\ \sigma_{22},\ \sigma_{33},\ \sigma_{23},\ \sigma_{13},\ \sigma_{12}]^T = [\sigma_1,\ \sigma_2,\ \sigma_3,\ \sigma_4,\ \sigma_5,\ \sigma_6]^T \ , \\ \overline{\epsilon} &= [\epsilon_{11},\ \epsilon_{22},\ \epsilon_{33},\ \epsilon_{23},\ \epsilon_{13},\ \epsilon_{12}]^T = [\epsilon_1,\ \epsilon_2,\ \epsilon_3,\ \epsilon_4,\ \epsilon_5,\ \epsilon_6]^T \ . \end{aligned} \tag{2.194}$$

Therefore, constitutive equations (2.179) reduces in the following:

$$\begin{cases} \sigma_p &= c_{pq}\epsilon_q - d_{kp}E_k, \\ D_i &= d_{iq}\epsilon_q + \varepsilon_{ik}E_k \ . \end{cases} \tag{2.195}$$

Double subscripts, introduced in (2.195) for the components of the material constitutive tensors, can be interpreted as follows: the first subscript refers to the direction of the excitation; the second subscript identifies the direction of the system response. As examples: d_{33} correlates the electric field component along direction 3 to the mechanical stress component along the same direction; d_{31} correlates the electric field component along direction 3 to the mechanical stress component along direction 1. For this reason, systems for which an electric field is applied along direction 3 in order to obtain a strain along the same axis (and vice versa) are said operating in the d_{33} *mode*. Following a similar reasoning, system designed to produce a strain along direction 1 when an electric field is applied along axis 3 (and vice versa) are said working in d_{31} *mode*.

2.4.4 Constitutive matrices specialized for PZT and PDVF materials

In section 2.4.1, tensors describing the characteristic of a piezoelectric solid have been introduced. Moreover, it has been concluded that the behavior of a piezoelastic solid is fully characterized by 45 parameters, consisting of:

- 21 independent parameters of the stiffness tensor $[\,c\,]$;
- 6 independent parameters of the permittivity tensor $[\,\varepsilon\,]$;
- 18 independent parameters of the piezoelectric coupling tensor $[\,d\,]$.

In many cases, however, it is possible to reduce the number of independent parameters needed for the characterization of the material by exploit crystallographic symmetry. With reference to Fig. 2.3, it can be seen that independent parameters reduces to 17 for a Polyvinylidene Fluoride (PVDF) material, and to 10 for a PZT crystal (22).

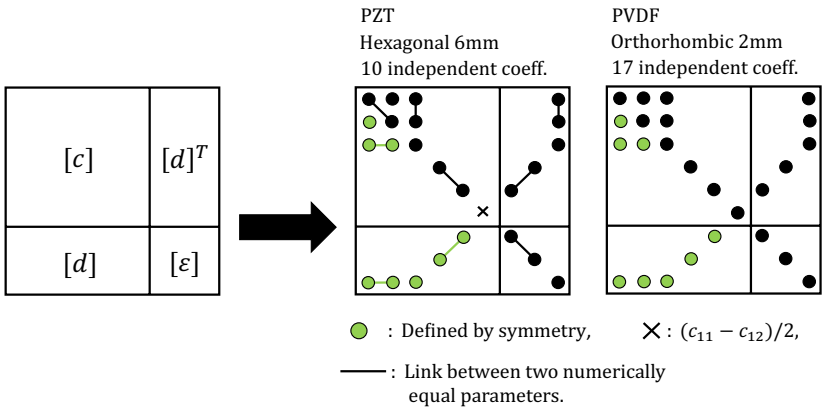

Figure 2.3: Visual representation of symmetry properties for PVDF and PZT materials. Independent parameters needed to fully characterize the solid reduces to 17 and to 10, respectively.

Therefore, if we assume a solid consisting of a linear piezoceramic, relative constitutive matrices have the following form:

$$[\,c\,] = \begin{bmatrix} c_{11} & c_{12} & c_{13} & 0 & 0 & 0 \\ c_{12} & c_{11} & c_{13} & 0 & 0 & 0 \\ c_{13} & c_{13} & c_{33} & 0 & 0 & 0 \\ 0 & 0 & 0 & c_{44} & 0 & 0 \\ 0 & 0 & 0 & 0 & c_{44} & 0 \\ 0 & 0 & 0 & 0 & 0 & \frac{(c_{11}-c_{12})}{2} \end{bmatrix}, \tag{2.196}$$

$$[\,d\,] = \begin{bmatrix} 0 & 0 & 0 & 0 & d_{15} & 0 \\ 0 & 0 & 0 & d_{15} & 0 & 0 \\ d_{31} & d_{31} & d_{33} & 0 & 0 & 0 \end{bmatrix}, \qquad [\,\varepsilon\,] = \begin{bmatrix} \varepsilon_{11} & 0 & 0 \\ 0 & \varepsilon_{11} & 0 \\ 0 & 0 & \varepsilon_{33} \end{bmatrix}, \tag{2.197}$$

where all independent parameters are constant.

Linear constitutive equations (2.178) can be expanded in the following set of

scalar equations:

$$\begin{cases} \sigma_1 &= c_{11}\epsilon_1 + c_{12}\epsilon_2 + c_{13}\epsilon_3 - d_{31}E_3 \\ \sigma_2 &= c_{12}\epsilon_1 + c_{11}\epsilon_2 + c_{13}\epsilon_3 - d_{31}E_3 \\ \sigma_3 &= c_{13}\epsilon_1 + c_{13}\epsilon_2 + c_{33}\epsilon_3 - d_{33}E_3 \\ \sigma_4 &= c_{44}\epsilon_4 - d_{15}E_2 \\ \sigma_5 &= c_{44}\epsilon_5 - d_{15}E_1 \\ \sigma_6 &= \frac{(c_{11}-c_{12})}{2}\epsilon_6 \\ D_1 &= \varepsilon_{11}E_1 + d_{15}\epsilon_5 \\ D_2 &= \varepsilon_{11}E_2 + d_{15}\epsilon_4 \\ D_3 &= \varepsilon_{33}E_3 + d_{31}\epsilon_1 + d_{31}\epsilon_2 + d_{33}\epsilon_3 \end{cases} . \tag{2.198}$$

By taking into account relations (2.95) and (2.53), equation set (2.198) can be recast so that components of $\overline{\sigma}_m$ and $\overline{D}$ are expressed as a function of the components of vector $\overline{\eta}$ and the scalar potential φ:

$$\begin{cases} \sigma_1 &= c_{11}\eta_{1,1} + c_{12}\eta_{2,2} + c_{13}\eta_{3,3} + d_{31}\varphi_{,3} \\ \sigma_2 &= c_{12}\eta_{1,1} + c_{11}\eta_{2,2} + c_{13}\eta_{3,3} + d_{31}\varphi_{,3} \\ \sigma_3 &= c_{13}\eta_{1,1} + c_{13}\eta_{2,2} + c_{33}\eta_{3,3} + d_{33}\varphi_{,3} \\ \sigma_4 &= c_{44}(\eta_{2,3} + \eta_{3,2}) + d_{15}\varphi_{,2} \\ \sigma_5 &= c_{44}(\eta_{1,3} + \eta_{3,1}) + d_{15}\varphi_{,1} \\ \sigma_6 &= \frac{(c_{11}-c_{12})}{2}(\eta_{1,2} + \eta_{2,1}) \\ D_1 &= d_{15}(\eta_{1,3} + \eta_{3,1}) - \varepsilon_{11}\varphi_{,1} \\ D_2 &= d_{15}(\eta_{2,3} + \eta_{3,2}) - \varepsilon_{11}\varphi_{,2} \\ D_3 &= d_{31}\eta_{1,1} + d_{31}\eta_{2,2} + d_{33}\eta_{3,3} - \varepsilon_{33}\varphi_{,3} \end{cases} . \tag{2.199}$$

2.4.5 Unidirectional piezoelectric constitutive equations

2.4.5.1 Problem formulation

With reference to Fig. 2.4, let us consider a rod of a linear piezoceramic[1] material - characterized by a uniform cross sectional area - having electrodes attached at the extremities (23).

Let denote by:

- L, the length of the considered solid;
- S_b^0, the bottom section of the solid ($S_b^0 = f(x_1, x_2, 0)$);
- S_b^L, the upper section of the solid ($S_b^L = f(x_1, x_2, L)$);

[1]The discussion is similar for the case of PVDF materials.

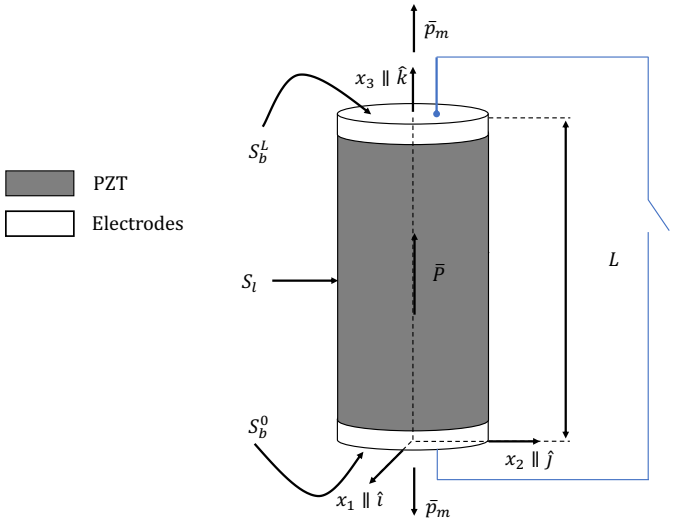

Figure 2.4: Piezoceramic rod subjected to a normal load $\overline{p}_m$. It has been denoted by: S_b^0 the surface of the bottom extremity of the rod; S_b^L the surface of the upper extremity; S_l the lateral surface of the rod. $\overline{P}$ is the resulting polarization vector.

- S_l, the lateral surface of the solid;
- Vol, the volume of the solid.

The rod is subjected to a normal load $\overline{p}_m$ along its principal intertia axis x_3. Electrodes thickness is considered negligible.

The following assumptions and boundary conditions are considered:

- Volume forces are equal to zero:

$$\overline{F}_V = \overline{0} \ , \qquad \forall P \in Vol \ . \tag{2.200}$$

As a consequence, the static equilibrium condition (2.73) becomes:

$$\begin{aligned} &\frac{\partial \sigma_{11}}{\partial x_1} + \frac{\partial \sigma_{12}}{\partial x_2} + \frac{\partial \sigma_{13}}{\partial x_3} = 0 \ , \\ &\frac{\partial \sigma_{21}}{\partial x_1} + \frac{\partial \sigma_{22}}{\partial x_2} + \frac{\partial \sigma_{23}}{\partial x_3} = 0 \ , \qquad \forall P \in Vol \\ &\frac{\partial \sigma_{31}}{\partial x_1} + \frac{\partial \sigma_{32}}{\partial x_2} + \frac{\partial \sigma_{33}}{\partial x_3} = 0 \ . \end{aligned} \tag{2.201}$$

- Surface forces on S_l are equal to zero:

$$\overline{p}_m = \overline{0} \qquad \forall P \in S_l \ . \tag{2.202}$$

With reference to Fig. 2.4, the normal vector of lateral surface S_l can be defined as $\overline{n} = n_1\hat{\imath} + n_2\hat{\jmath}$. Therefore, (2.202) results in the following scalar equations:

$$\begin{aligned} &\sigma_{11}n_1 + \sigma_{12}n_2 = 0 \ , \\ &\sigma_{21}n_1 + \sigma_{22}n_2 = 0 \ , \qquad \forall P \in S_l \\ &\sigma_{31}n_1 + \sigma_{32}n_2 = 0 \ . \end{aligned} \tag{2.203}$$

- Surface forces, on S_b^0 and S_b^L, are given as follows:

$$\begin{aligned} \overline{p}^0(x_1, x_2) &= p_1^0\hat{\imath} + p_2^0\hat{\jmath} + p_3^0\hat{k} = 0\hat{\imath} + 0\hat{\jmath} + p_3^0\hat{k} \qquad \forall P \in S_b^0 \ , \\ \overline{p}^L(x_1, x_2) &= p_1^L\hat{\imath} + p_2^L\hat{\jmath} + p_3^L\hat{k} = 0\hat{\imath} + 0\hat{\jmath} + p_3^L\hat{k} \qquad \forall P \in S_b^L \ . \end{aligned} \tag{2.204}$$

As a consequence of the solid equilibrium condition, the following equations must be verified:

$$\begin{aligned} \int_{S_b^0} \overline{p}^0 \mathrm{d}S + \int_{S_b^L} \overline{p}^L \mathrm{d}S = \overline{0} \ , \\ \int_{S_b^0} \overline{r} \times \overline{p}^0 \mathrm{d}S + \int_{S_b^L} \overline{r} \times \overline{p}^L \mathrm{d}S = \overline{0} \ . \end{aligned} \tag{2.205}$$

From the equivalence conditions on surfaces S_b^0 and S_b^L, it results:

$$\begin{aligned} &\sigma_{13} = 0 \ , \\ &\sigma_{23} = 0 \ , \qquad \forall P \in S_b^0 \cup S_b^L \\ &\sigma_{33} = p_3 \ . \end{aligned} \tag{2.206}$$

- The free charge density ρ_e, in the volume of the rod, is equal to zero:

$$\rho_e = 0 \ , \qquad \forall P \in Vol \ , \tag{2.207}$$

as the rod consists of a dielectric material. From the Gauss's law (2.33), the null divergence condition for vector $\overline{D}$ results verified:

$$\frac{\partial D_1}{\partial x_1} + \frac{\partial D_2}{\partial x_2} + \frac{\partial D_3}{\partial x_3} = 0 \ , \qquad \forall P \in Vol \ . \tag{2.208}$$

- The free charge density (σ_e) on S_l is equal to zero:

$$\sigma_e = 0 \qquad \forall P \in S_l \ , \tag{2.209}$$

therefore, from the last of (2.240), it results:

$$D_1 n_1 + D_2 n_2 = 0 \qquad \forall P \in S_l \ . \tag{2.210}$$

- Points on surfaces where electrodes are applied (S_b^0 and S_b^L), present the same electric potential. As a consequence, it must result:

$$E_1 = E_2 = 0 \ , \qquad \forall P \in S_b^0 \cup S_b^L \ . \tag{2.211}$$

- The zero curl condition is considered for the electric field:

$$\begin{aligned} \frac{\partial E_3}{\partial x_2} - \frac{\partial E_2}{\partial x_3} &= 0 \ , \\ \frac{\partial E_1}{\partial x_3} - \frac{\partial E_3}{\partial x_1} &= 0 \ , \\ \frac{\partial E_2}{\partial x_1} - \frac{\partial E_1}{\partial x_2} &= 0 \ , \end{aligned} \tag{2.212}$$

as we are considering a static problem.

2.4.5.2 Solution through the semi-inverse method

The static problem formalized in the previous subsection, can be solved through the *semi inverse* method.

With reference to constitutive equations 2.186, it can be proved that tensors $[\,s\,]_{|\epsilon D|}$, $[\,d\,]_{|\epsilon D|}$, and $[\,\varepsilon\,]_{|\epsilon D|}$ presents the same structure of tensors $\left[\,c\,\right]$, $\left[\,d\,\right]$, and $[\,\varepsilon\,]$. Therefore, the extended form of (2.186) results, for the case of a PZT material, in the following set of scalar equations:

$$\begin{cases} \epsilon_{11} &= s_{11}^{|\epsilon D|}\sigma_{11} + s_{12}^{|\epsilon D|}\sigma_{22} + s_{13}^{|\epsilon D|}\sigma_{33} + d_{31}^{|\epsilon D|}E_{33} \ , \\ \epsilon_{22} &= s_{21}^{|\epsilon D|}\sigma_{11} + s_{11}^{|\epsilon D|}\sigma_{22} + s_{13}^{|\epsilon D|}\sigma_{33} + d_{31}^{|\epsilon D|}E_{33} \ , \\ \epsilon_{33} &= s_{31}^{|\epsilon D|}\sigma_{11} + s_{31}^{|\epsilon D|}\sigma_{22} + s_{33}^{|\epsilon D|}\sigma_{33} + d_{33}^{|\epsilon D|}E_{33} \ , \\ \epsilon_{23} &= s_{44}^{|\epsilon D|}\sigma_{23} + d_{15}^{|\epsilon D|}E_2 \ , \\ \epsilon_{13} &= s_{44}^{|\epsilon D|}\sigma_{13} + d_{15}^{|\epsilon D|}E_1 \ , \\ \epsilon_{12} &= s_{66}^{|\epsilon D|}\sigma_{12} \ , \\ D_1 &= \varepsilon_{11}^{|\epsilon D|}E_1 + d_{15}^{|\epsilon D|}\sigma_{13} \ , \\ D_2 &= \varepsilon_{11}^{|\epsilon D|}E_2 + d_{15}^{|\epsilon D|}\sigma_{23} \ , \\ D_3 &= \varepsilon_{33}^{|\epsilon D|}E_3 + d_{31}^{|\epsilon D|}\sigma_{11} + d_{31}^{|\epsilon D|}\sigma_{22} + d_{33}^{|\epsilon D|}\sigma_{33} \ . \end{cases} \tag{2.213}$$

Boundary conditions on the lateral surface of the rod, expressed by (2.203) and (2.210), are verified by setting:

$$\begin{aligned} &\sigma_{11} = \sigma_{22} = \sigma_{23} = \sigma_{13} = \sigma_{12} = 0 \ , \\ &D_1 = D_2 = 0 \ . \end{aligned} \tag{2.214}$$

By taking into account (2.214), equations (2.203) and (2.208) becomes:

$$\frac{\partial \sigma_{33}}{\partial x_3} = 0 \ , \tag{2.215a}$$

$$\frac{\partial D_3}{\partial x_3} = 0 \ , \tag{2.215b}$$

from which results:

$$\begin{aligned} &\sigma_{33} = \text{const.} = p_{m_3} \ , \\ &D_3 = \text{const.} \ . \end{aligned} \tag{2.216}$$

Therefore, the possible solution derived from: the boundary conditions on S_l; the equilibrium equation; and the zero condition for ρ_e; can be summarized as follows (23):

$$\begin{aligned} &\sigma_{11} = \sigma_{22} = \sigma_{23} = \sigma_{13} = \sigma_{12} = 0 \ , \qquad \sigma_{33} = p_{m_3} \ , \\ &D_1 = D_2 = 0 \ , \qquad D_3 = \text{const.} \ . \end{aligned} \tag{2.217}$$

Solution (2.217) satisfies condition (2.206) and allows, through the constitutive equations (2.213), for obtaining the following solution for the electric field:

$$E_1 = E_2 = 0 \ , \quad E_3 = \text{const.}, \qquad \forall P \in Vol \ , \tag{2.218}$$

which satisfies both boundary condition (2.211) and (2.212).

Since the proposed solution verifies all the equations and the boundary conditions describing the problem, it can be considered as valid.

By substituting it in (2.213), the unidirectional piezoelectric constitutive equations are obtained:

$$\begin{cases} \epsilon_{23} = \epsilon_{13} = \epsilon_{12} = 0 \\ \epsilon_{11} = \epsilon_{22} = s_{13}^{|\epsilon D|} p_{m_3} + d_{31}^{|\epsilon D|} E_3 \\ E_1 = E_2 = 0 \\ \epsilon_{33}^{|\epsilon D|} = s_{33}^{|\epsilon D|} p_{m_3} + d_{33}^{|\epsilon D|} E_3 \\ D_3 = d_{33}^{|\epsilon D|} p_{m_3} + \varepsilon_{33}^{|\epsilon D|} E_3 \end{cases} . \tag{2.219}$$

In (2.219) we state that the electric field and the displacement vector are constants along direction 3. By considering the electrical boundary conditions for the short-circuit and open-circuit cases, it directly derives what follows:

- for the short-circuit case: $E_3 = 0$; $D_3 = d_{33}^{|\epsilon D|} p_{m_3}$;
- for the open-circuit case: $E_3 = -\frac{d_{33}^{|\epsilon D|}}{\varepsilon_{33}^{|\epsilon D|}} p_{m_3}$; $D_3 = 0$.

Last two expressions in (2.219) suffice to describe the behavior of a linear PZT material working in d_{33} mode. For such a material, the stress-charge form of the constitutive equations is:

$$\begin{cases} \sigma_3 = c_{33}\epsilon_3 - d_{33}E_3 \\ D_3 = d_{33}\epsilon_3 + \varepsilon_{33}E_3 \end{cases} . \tag{2.220}$$

2.4.6 Strong form

In this section, the derivation of mathematical expressions describing the behavior of a linear piezoelectric system is discussed. The problem is formulated in terms of two unknown variables: the displacement vector $\overline{\eta}$, and the scalar electric potential φ. For ease of reading, involved fundamental relations are hereafter reported. Briefly, they are:

- The strain-displacement relation (2.95):

$$\overline{\epsilon} = [\,\partial\,]\,\overline{\eta}\ . \tag{2.221}$$

- The differential equation stating the relationship between the electric field and the electric potential:

$$\overline{E} = -\overline{\nabla}\varphi\ , \tag{2.222}$$

- The constitutive equations (2.178):

$$\begin{cases} \overline{\sigma} = [\,c\,]\,\overline{\epsilon} - [\,d\,]^T\overline{E} \\ \overline{D} \ = [\,d\,]\overline{\epsilon} + [\,\varepsilon\,]\,\overline{E} \end{cases} . \tag{2.223}$$

- The Gauss's law for a dielectric medium (2.33), which can be recast in the following form:

$$\overline{\nabla}^T\overline{D} = \rho_e\ . \tag{2.224}$$

- The Navier's equations (2.75), describing dynamics of mechanical systems:

$$[\,\partial\,]^T\,\overline{\sigma} + \overline{F}_V = \rho\ddot{\overline{\eta}}\ , \tag{2.225}$$

where we denoted by $\ddot{\overline{\eta}}$ the second derivative, in time domain, of the displacement vector.

By substituting (2.222) and (2.221) in the constitutive equations (2.223), it results:

$$\begin{cases} \overline{\sigma} = [\,c\,]\,[\,\partial\,]\,\overline{\eta} + [\,d\,]^T\,\overline{\nabla}\varphi \\ \overline{D} = [\,d\,]\,[\,\partial\,]\,\overline{\eta} - [\,\varepsilon\,]\,\overline{\nabla}\varphi \end{cases}\ , \tag{2.226}$$

which can be respectively included in (2.225) and (2.224), in order to obtain:

$$\begin{cases} \left([\,\partial\,]^T\,[\,c\,]\,[\,\partial\,]\right)\overline{\eta} + \left([\,\partial\,]^T\,[\,d\,]^T\,\overline{\nabla}\right)\varphi + \overline{F}_V &= \rho\ddot{\overline{\eta}} \\ \left(\overline{\nabla}^T\,[\,d\,]\,[\,\partial\,]\right)\overline{\eta} - \left(\overline{\nabla}^T\,[\,\varepsilon\,]\,\overline{\nabla}\right)\varphi &= \rho_e \end{cases}\ . \tag{2.227}$$

Equation set (2.227) consist of four Partial Derivative Equations (PDEs) describing the dynamics of the displacement field and the electric potential in every point of the volume occupied by the considered system.

In order to fully formalize the problem, boundary condition must be taken into account. With this aim, let us consider the surface (S) delimiting the volume occupied by the piezoelectric material (Vol). By denoting as:

S_η the portion of S where a known displacement field $\overline{\eta}_\flat$ is applied;

S_{p_m} the portion of S where boundary forces $\overline{p}_m$ are applied;

S_φ the portion of S where the distribution $\varphi_\flat$ of the electric potential is given;

S_{q_e} the portion of S where free charges (q_e) are collected, with density σ_e;

the overall boundary (S) can be partitioned as reported in the following sets relations:

$$S_\eta \cup S_{p_m} = S_\varphi \cup S_{q_e} = S \tag{2.228}$$

$$S_\eta \cap S_{p_m} = S_\varphi \cap S_{q_e} = \varnothing \tag{2.229}$$

More in detail, the following relation holds for any point P on boundary S_η:

$$\overline{\eta} = \overline{\eta}_\flat \qquad \forall P \in S_\eta \ . \tag{2.230}$$

On boundary S_{p_m}, stress field must coincide with boundary forces p_m. Therefore:

$$[\,\sigma_m\,]\,\overline{n} = \overline{p} \qquad \forall P \in S_{p_m} \ , \tag{2.231}$$

where it has been denoted by $\overline{n} = [n_x, n_y, n_z]^T$ the outward pointing, unit normal vector of S at any point P. By defining the following tensor:

$$\big[\mathscr{N}\big]^T = \begin{bmatrix} n_x & 0 & 0 & n_y & n_z & 0 \\ 0 & n_y & 0 & n_x & 0 & n_z \\ 0 & 0 & n_z & 0 & n_x & n_y \end{bmatrix} \ , \tag{2.232}$$

equation (2.231) can be recast as follows:

$$[\mathscr{N}]^T\,\overline{\sigma}_m = \overline{p}_m \qquad \forall P \in S_{p_m}. \tag{2.233}$$

By pre-multiplying both sides of the first of (2.226) by $[\mathscr{N}]^T$, it results:

$$\Big([\mathscr{N}]^T\,[\,c\,]\,[\,\partial\,]\Big)\,\overline{\eta} + \Big([\mathscr{N}]^T\,[\,d\,]^T\,\overline{\nabla}\Big)\,\varphi = \overline{p}_m \ . \tag{2.234}$$

If we assume that boundary S_φ represents the surface of the piezoelectric material on which electrodes are applied, it is reasonable to consider the distribution of the electric potential on S_φ as constant with respect to spatial coordinates, therefore:

$$\varphi = \varphi_\flat(t) \qquad \forall P \in S_\varphi \ . \tag{2.235}$$

Finally, on boundary S_{q_e} the following relation must hold:

$$\overline{n}^T\overline{D} = -\sigma_e \qquad \forall P \in S_{q_e} \ , \tag{2.236}$$

stating that the projection of the electric displacement vector on the unit normal vector of S_{q_e} is equal to the opposite of the free charge surface density σ_e. By pre-multiplying both sides of the second equation in set (2.226) by $\overline{n}^T$, it results:

$$\big(\overline{n}^T\,[\,d\,]\,[\,\partial\,]\big)\,\overline{\eta} - \big(\overline{n}^T\,[\,\varepsilon\,]\,\overline{\nabla}\big)\,\varphi = -\sigma_e \qquad \forall P \in S_{q_e} \ . \tag{2.237}$$

Based on the analysis above reported, the linear piezoleastic problem is fully described by the following set of equation:

$$\begin{aligned}
\big([\partial]^T[c][\partial]\big)\overline{\eta} + \big([\partial]^T[d]^T\overline{\nabla}\big)\varphi + \overline{F}_V = \rho\ddot{\overline{\eta}}, &\qquad \forall P \in Vol,\\
\big(\overline{\nabla}^T[d][\partial]\big)\overline{\eta} - \big(\overline{\nabla}^T[\varepsilon]\overline{\nabla}\big)\varphi = \rho_e\ , &\qquad \forall P \in Vol,\\
\big([\mathscr{N}]^T[c][\partial]\big)\overline{\eta} + \big([\mathscr{N}]^T[d]^T\overline{\nabla}\big)\varphi = \overline{p}_m\ , &\qquad \forall P \in S_{p_m},\\
\big(\overline{n}^T[d][\partial]\big)\overline{\eta} - \big(\overline{n}^T[\varepsilon]\overline{\nabla}\big)\varphi = -\sigma_e\ , &\qquad \forall P \in S_{q_e},\\
\overline{\eta} = \overline{\eta}_\flat\ , &\qquad \forall P \in S_\eta,\\
\varphi = \varphi_\flat, &\qquad \forall P \in S_\varphi.
\end{aligned} \tag{2.238}$$

Equations (2.225), (2.224), (2.223), (2.221), and (2.222) can be rewritten by using the indicial notation as follows:

$$\begin{aligned}
\sigma_{ij,j}\rho + F_i = \rho\ddot{\eta}_i\ , &\qquad \forall P \in Vol\ ,\\
D_{i,i} = \rho_e, &\qquad \forall P \in Vol\ ,\\
\sigma_{ij} = c_{ijkl}\epsilon_{kl} - d_{kij}E_k\ , &\qquad \forall P \in Vol \cup S\ ,\\
D_i = \varepsilon_{ik}E_k + d_{ikl}\epsilon_{kl}\ , &\qquad \forall P \in Vol \cup S\ ,\\
\epsilon_{ij} = \frac{1}{2}\big(u_{i,j} + u_{j,i}\big)\ , &\qquad \forall P \in V \cup S\ ,\\
E_i = -\varphi_{,i}\ , &\qquad \forall P \in Vol \cup S\ .
\end{aligned} \tag{2.239}$$

Mechanical and electrical boundary conditions, in indicial notation, are written as:

$$\begin{aligned}
\eta_i = \eta_{\flat_i}\ , &\qquad \forall P \in S_\eta\ ,\\
\sigma_{ij}n_j = p_{m_i}, &\qquad \forall P \in S_{p_m},\\
\varphi = \varphi_\flat, &\qquad \forall P \in S_\varphi,\\
D_i n_i = -\sigma_e, &\qquad \forall P \in S_{q_e}\ .
\end{aligned} \tag{2.240}$$

2.4.7 Weak form

The piezoelastic problem can be formulated starting from conservation principle of the following hamiltonian functional (24):

$$\Xi(\eta_i, \varphi) = \int_{t_0}^{t_1} \big(\mathscr{L} + W\big)\mathrm{d}t\ , \tag{2.241}$$

where $\mathscr{L}$ is the lagrangian function of the considered system and W represents virtual work related to external mechanical and electrical forces. According to the Hamilton's principle, infinitesimal variations of quantities describing the state of

the considered system (i.e., η_i and φ) must occur in such a way that potential Ξ remains constant:

$$\delta\Xi(\eta_i, \varphi) = \delta \int_{t_0}^{t_1} \big(\mathscr{L} + W\big)\mathrm{d}t = 0 \ . \tag{2.242}$$

From (2.242) it results:

$$\int_{t_0}^{t_1} \delta\big(\mathscr{L} + W\big)\mathrm{d}t = 0 \quad \Rightarrow \quad \delta\mathscr{L} + \delta W = 0 \ . \tag{2.243}$$

With reference to the case of a piezoelastic system, the work done from external forces comprises two contribution: mechanical virtual work (W_m), and electrical virtual work (W_e).

By denoting as:

$F_{V_i},\ i = 1,\ 2,\ 3$, the components of the volume force acting on the piezoelectric body;

$p_{m_i},\ i = 1,\ 2,\ 3$, the components of boundary loads acting on S_{p_m};

$F_i,\ i = 1,\ 2,\ 3$, the components of possible point loads acting on the body;

the mechanical external work related to an infinitesimal virtual displacement η_i, is given by the following:

$$\delta W_m = \int_{Vol} F_{V_i}\delta\eta_i \mathrm{d}Vol + \int_{S_{pm}} p_{m_i}\delta\eta_i \mathrm{d}S + \sum_{k=1}^{m} F_i^k \delta\eta_i^k \ , \tag{2.244}$$

where m point loads have been assumed acting on the piezoelectric solid.

By denoting as Q_k ($k = 1,\ ...,\ w$) possible point charges distributed on the boundary S, the virtual electric work related to an infinitesimal variation $\delta\varphi$ of the electric potential, can be written as:

$$\delta W_e = -\int_{S_{qe}} \sigma_e \delta\varphi \mathrm{d}S - \sum_{k=1}^{w} Q_k \delta\varphi_k. \tag{2.245}$$

Therefore, it results:

$$\begin{aligned} \delta W = \delta W_m + \delta W_e = &\int_{Vol} F_{V_i}\delta\eta_i \mathrm{d}Vol + \int_{S_{pm}} p_{m_i}\delta\eta_i \mathrm{d}S \\ &- \int_{S_{qe}} \sigma_e \delta\varphi \mathrm{d}S + \sum_{k=1}^{m} F_i^k \delta\eta_i^k - \sum_{k=1}^{w} Q_k \delta\varphi_k \ . \end{aligned} \tag{2.246}$$

Generally, function $\mathscr{L}$ is defined by the sum of the kinetic and the potential energies associated to the considered system. With reference to the case of a piezoelectric system, potential energy consists of an elastic and an electrostatic contribution. They can be taken into account by considering the opposite of the electric enthalpy thermodynamic potential. Therefore:

$$\mathscr{L} = \int_{Vol} \big(\kappa - h\big) \mathrm{d}Vol \ , \tag{2.247}$$

where we denoted by κ the kinetic energy density and by h the electric enthalpy density. They can be evaluated as follows(24):

$$\begin{aligned} \kappa &= \frac{1}{2}\rho\dot{\eta}_i^2 \ , \\ h &= \frac{1}{2}\left(\sigma_{ij}\epsilon_{ij} - E_r D_r\right) \ . \end{aligned} \tag{2.248}$$

Therefore, the lagrangian function related to the considered system, can be written in the form:

$$\mathscr{L} = \frac{1}{2}\int_{Vol} \big(\rho\dot{\eta}_i^2 - \sigma_{ij}\epsilon_{ij} + E_r D_r\big) \mathrm{d}Vol \ . \tag{2.249}$$

We are interested in infinitesimal variations of $\mathscr{L}$ (see (2.243)):

$$\delta\mathscr{L} = \int_{Vol} \big(\delta\kappa - \delta h\big) \mathrm{d}Vol \ , \tag{2.250}$$

which is related to variations in the system kinetic and potential energies. The evaluation of $\delta\kappa$ is straightforward:

$$\delta\kappa = \frac{1}{2}\rho\delta\big(\dot{\eta}_i^2\big) = \frac{1}{2}\rho\big(2\ddot{\eta}_i\delta\eta_i\big) = \rho\ddot{\eta}_i\delta\eta_i \ . \tag{2.251}$$

With reference to the electric enthalpy infinitesimal variation, by considering the second of (2.248) it results:

$$\begin{aligned} \delta h &= \frac{1}{2}\big(\sigma_{ij}\delta\epsilon_{ij} + \epsilon_{ij}\delta\sigma_{ij} - D_r\delta E_r - E_r\delta D_r\big) \\ &= \frac{1}{2}\bigg(\sigma_{ij}\delta\epsilon_{ij} + \frac{\partial\sigma_{ij}}{\partial\epsilon_{kl}}\epsilon_{ij}\delta\varepsilon_{kl} + \frac{\partial\sigma_{ij}}{\partial E_k}\epsilon_{ij}\delta E_k \\ &\quad - D_r\delta E_r - \frac{\partial D_r}{\partial\epsilon_{kl}}E_r\delta\epsilon_{kl} - \frac{\partial D_r}{\partial E_k}E_r\delta E_k\bigg) \ . \end{aligned} \tag{2.252}$$

By taking into account constitutive equations (2.179), and definitions of piezoelectric constants (2.166) and (2.171), equation (2.252) can be recast as follows:

$$\delta h = \frac{1}{2}\big(2c_{ijkl}\epsilon_{kl}\delta\epsilon_{ij} - 2d_{kij}E_k\delta\epsilon_{ij} - 2\varepsilon_{rk}E_k\delta E_r - 2d_{rkl}\epsilon_{kl}\delta E_r\big) \ . \tag{2.253}$$

Therefore, it is possible to write $\delta\mathscr{L}$ as:

$$\delta\mathscr{L} = \int_{Vol} \big(\rho\ddot{\eta}_i\delta\eta_i - c_{ijkl}\epsilon_{kl}\delta\epsilon_{ij} + d_{kij}E_k\delta\epsilon_{ij} + \varepsilon_{rk}E_k\delta E_r + d_{rkl}\epsilon_{kl}\delta E_r\big)\mathrm{d}Vol \ . \quad (2.254)$$

From (2.242), it results that the following condition must be satisfied:

$$\begin{aligned}\delta\Xi = \int_{t_0}^{t_1} \big(\delta\mathscr{L} + \delta W\big)\mathrm{d}t = \int_{t_0}^{t_1} \mathrm{d}t \int_{Vol} \big(\rho\ddot{\eta}_i\delta\eta_i - c_{ijkl}\epsilon_{kl}\delta\epsilon_{ij} + \\ + d_{kij}E_k\delta\epsilon_{ij} + \varepsilon_{rk}E_k\delta E_m + d_{rkl}\epsilon_{kl}\delta E_r\big)\mathrm{d}Vol + \int_{t_0}^{t_1} \mathrm{d}t \sum_{k=1}^{m} F_i^k\delta\eta_i^k + \\ + \int_{t_0}^{t_1} \mathrm{d}t \int_{S_\eta} p_{m_i}\delta\eta_i\mathrm{d}S - \int_{t_0}^{t_1} \mathrm{d}t \int_{S_{q_e}} \sigma_e\delta\varphi\mathrm{d}S - \int_{t_0}^{t_1} \mathrm{d}t \sum_{k=1}^{w} Q_k\delta\varphi_k = 0 \ ,\end{aligned} \quad (2.255)$$

from which the *weak form* formulation of the piezolastic problem can be obtained:

$$\begin{aligned}\int_{Vol} \big(\rho\ddot{\eta}_i\delta\eta_i - c_{ijkl}\epsilon_{kl}\delta\epsilon_{ij} + d_{kij}E_k\delta\epsilon_{ij} + \varepsilon_{rk}E_k\delta E_r + d_{rkl}\epsilon_{kl}\delta E_r\big)\mathrm{d}Vol + \\ + \int_{Vol} F_{V_i}\delta\eta_i\mathrm{d}Vol + \int_{S_{p_m}} p_{m_i}\delta\eta_i\mathrm{d}S - \int_{S_{q_e}} \sigma_e\delta\varphi\mathrm{d}S + \\ + \sum_{k=1}^{m} F_i^k\delta\eta_i^k - \sum_{k=1}^{w} Q_k\delta\varphi_k = 0 \ .\end{aligned} \quad (2.256)$$

3

A nonlinear circuit for modeling piezoelectric material effects on multiple scales

3.1 Introduction

This chapter focuses on investigating the role of material nonlinearities on the dynamic performances of devices designed for Energy Harvesting (EH) applications. The study is here limited to the case of piezoceramic materials (PZT).

As a preliminary step to the introduction of the physics-based model employed in this work, physical properties and constitutive nonlinearities of piezoceramic materials are discussed in details. Moreover, a review on hysteresis modeling techniques is reported.

A rate-dependent, physics-based free energy model for a PZT single crystal is then presented in detail. The model is able to reproduce, through a probabilistic thermodynamic approach, what can be considered as the source of hysteresis: the switching of dipoles in crystal domains. Numerical investigations aimed at understanding the influence of crystal parameters on the material hysteretic response are also reported.

Finally, a multiscale approach is adopted in order to comprise crystal domain mesoscopic evolution in the dynamic response of two energy harvester devices that, on a macroscopic scale, are modeled as Single Degree of Freedom (SDOF) systems. Numerical simulations of the resulting models allow for investigating effects of PZT nonlinearities on the harvested power (in contrast with generating performances predicted by the relative non-hysteretic models).

In order to provide an effective visualization of the role that the material mesoscopic evolution has on the energy transduction process, lumped circuit representations of the models are also derived. Implementation issue are discussed in detail.

3.2 Physical properties of piezoceramic materials

Piezoelectric materials exhibit a *domain structure* and *spontaneous* strain and polarization that can be varied by applying electric and stress fields. The arrangement (orientation) of dipoles within domains aims at minimizing electrostatic and elastic energy.

An important group of piezoelectric materials are the piezoelectric ceramics, of which PZT is an example. Piezoceramics are polycrystalline ferroelectric materials isostructural with the mineral *Perovskite* ($CaTiO_3$). Perovskite materials exhibit a cubic (isotropic) structure for temperatures above the Curie point (T_c), and tetragonal (anisotropic) structure for temperatures from below T_c. The former corresponds to the *paraelectric* phase of the material (Fig. 3.1-a); the latter identifies the *ferroelectric* phase (Fig. 3.1-b,c,d).

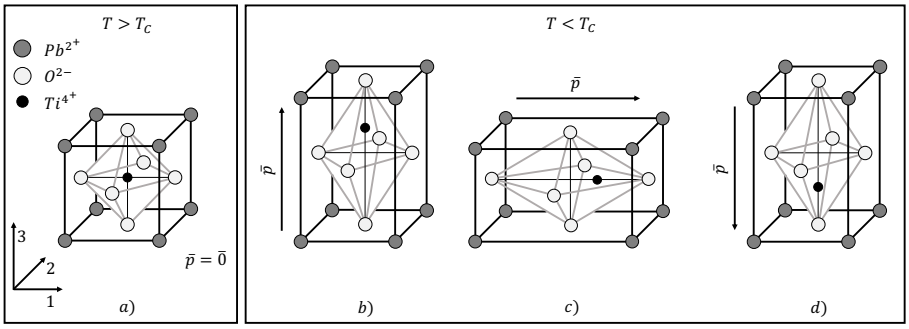

Figure 3.1: Unit cell configurations for a $PbTiO_3$ crystal in: a) the paraelectric phase ($T > T_C$); b) the ferroelectric phase ($T < T_C$).

With reference to Fig. 3.1, the symmetric ionic configuration corresponding to the paraelectric phase makes the barycenters of both positive and negative charges to be located at the center of the unit cell. As a consequence, a net polarization equal to zero corresponds to this state.

In the ferroelectric phase, unit cells can exists in one of six tetragonal structures characterized by having the tetravalent metal ion (Ti^{4+}, for the case depicted in Fig. 3.1) biased along one of the three mutually orthogonal crystallographic directions. This non-symmetric configuration produces a net polarization different from zero.

All the variants identified in the ferroelectric phase correspond to minimum energy configurations, at the considered temperature T.

The position of Ti^{4+}, in unit cells existing in the ferroelectric phase, can change under the effects of electric and mechanical loads. Moreover, strong enough loads might trigger unit cells switching from a variant to another. The process is sketched in Fig. 3.2 for the one-dimensional case of a PZT crystal working in d_{33} mode.

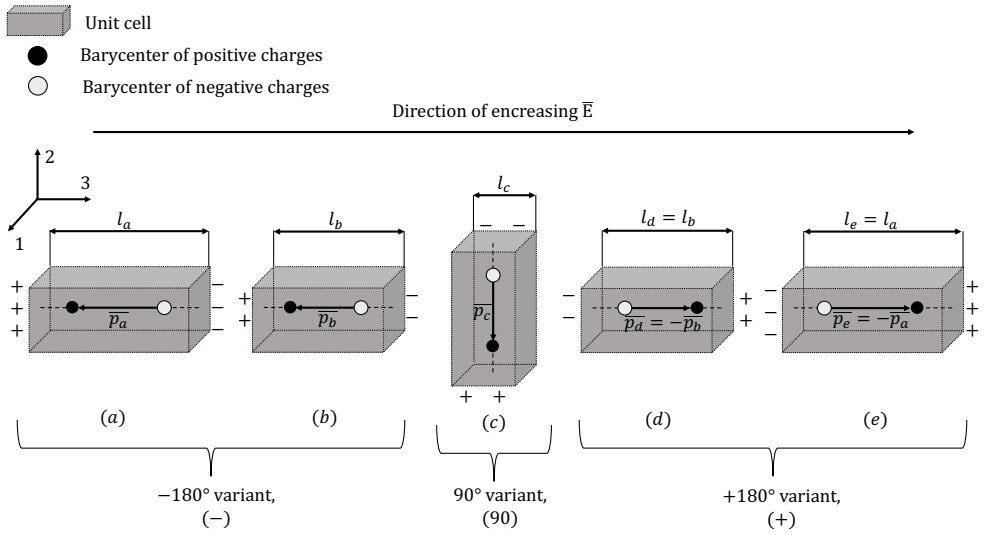

Figure 3.2: Unit cell switching process for a PZT crystal under electrical loading.

With reference to Fig. 3.2, it is possible to distinguish three variants for the unit cells of the considered material:

- (−) variant, characterized by having a $-180°$ orientation with respect to axis 3 (configurations $(a), (b)$);
- (90) variant, characterized by having a $90°$ orientation with respect to axis 3 (configuration (c));
- (+) variant, characterized by having the same orientation of axis 3 (configurations $(d), (e)$).

Let assume that configuration (a) is an initial equilibrium condition for the unit cell (when no electric field and mechanical stress are applied). A positive electric field $\overline{E}$ along direction 3, will result in a movement of the Ti^{4+} ion such that the distance between the barycenters of positive and negative charges decreases. As a consequence, both the dipole moment ($|p_{b_3}| < |p_{a_3}|$) and the geometry of the

unit cell will change ($l_b < l_a$[1]). The unit cell has moved from configuration (a) to configuration (b).

A further increase of the electric field (over the coercive value), will cause the Ti^{4+} ion to jump out the ($-$) orientation and into (90) orientation, which is an unstable position in the absence of any mechanical loads (1), thus causing the ion to continue towards the ($+$) orientation. In configuration (d), the unit cell presents a polarization reversed with respect to (b), but same geometrical characteristics. With a stronger positive electric field, the ion will move towards configuration (e), increasing both the polarization ($p_e > p_d$) and the size of the unit cell along direction 3. Note that (e) is symmetric with respect to the initial equilibrium configuration (a). Therefore, if now the electric field is removed, unit cell remains in this new equilibrium position: the process has caused the crystal repoling. Note that ($+$) and ($-$) configurations depicted in Fig. 3.2 present the same strain, as the relative polarization forms are symmetric.

A description of the switching process has been provided for the case of purely electrical loading. However, since the material is electromechanically coupled, the process can be triggered also by sufficiently large mechanical loads. Generally, there exist two different types of switchings in ferroelectric materials: 180°- and 90°-switchings. 180°-switchings occur between variants having opposite polarization vectors, whereas 90°-switchings involve variants whose polarization are 90° apart. Electric fields can induce both 180°- and 90°-switchings, while mechanical stresses produce only non-180°-switchings (25, 26). It is believed that the domain switching process in piezoceramics results from two successive 90° switches rather than a single 180° switch even for electrically induced switching (27).

Figure 3.3, provided by (1), shows experimental major hysteresis loops for an electrically loaded PZT actuator, in quasi-static conditions. The evolution in time domain of polarization and strain is also reported, showing different relaxation times that can be related to different switching mechanisms.

Concluding, the microscopic transitions from a variant to another occurring within domains, determines the highly nonlinear electromechanical behavior observed in PZT materials and is the source of the rate-dependent hysteresis.

[1]The slight variation of unit cell size along axis 1 and axis 2 is not represented in Fig. 3.2.

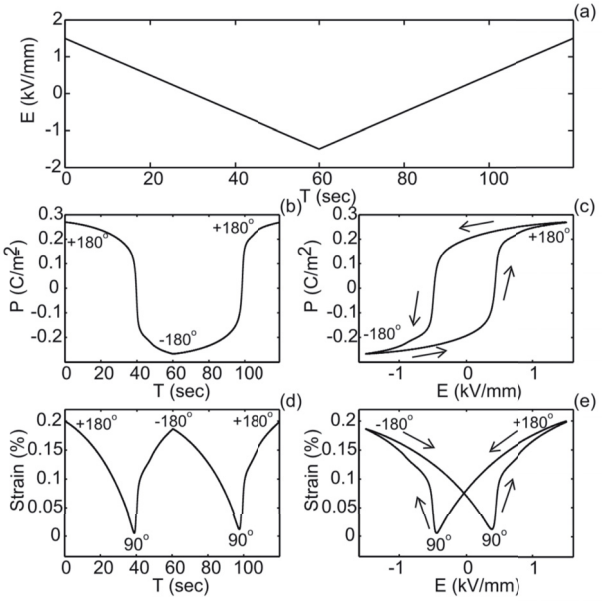

Figure 3.3: Experimental full major hysteresis loops of a PZT actuator electrically loaded: a) driving electric field; b) polarization vs time; c) polarization vs electric field; d) strain vs time; e) strain vs electric field (1).

3.3 Modeling of PZT crystal nonlinearities

3.3.1 Introduction

Rate-dependent hysteresis modeling is a complex and computationally onerous task (28). Techniques developed so far can be classified in two main categories: *physics-based* and *phenomenological* techniques. Phenomenological models are considered advantageous when the underlying physics of the system is poorly understood or difficult to characterize (29, 30). Therefore, starting from experimental curves, a certain set of macroscopic variables are chosen in order to mathematically describe the observed behavior. Based on the different mathematical explanation type adopted, these models can be distinguished into two main categories: differential equation-based model (Duhem model, Backlash-like model, BoucWen model) and operator-based model (Preisach model, PrandtlIshlinskii model, Krasnosel'skii-Pokrovskii model) (31, 32, 33, 34).

The Preisach model is one of the most popular operator-based model and is widely used in the smart material control applications (35, 36). It is defined by an integral operator which maps an input time series to an output time series by superimposing (through density functions) weighted outputs of indefinitely many elementary hysteresis loop. It allows a good hysteresis characterization at narrow-

band frequency as well as at no-load condition (37). To increase its accuracy, which gradually deteriorates as the input frequency increases, many modified Preisach models have been developed by researchers so far, in different fields of application. In some approaches, hybrid models proved to effectively enhance Preisach model performances (38, 39). The Krasnoselski-Pokrovskii (KP) model, derived from the Preisach, provides more information about the nonlinearity compared to its predecessor, thanks to its ability to record all previous extremes of hysteresis input output behaviors (37). KP model enabled some researchers to characterize the hysteresis nonlinearity in magnetically shaped memory alloys (40). The Prandtl-Ishlinskii (PI) model is another operator-based model which can be considered as a subset of Preisach one. It is defined in terms of an integral of play or stop operators, with a density function determining the shape of hysteresis. It has a simple mathematical structure and is attractive for real-time applications (due to its analytically evaluable inverse) (41). Preisach models and its subclass PI variant are, by far, the most well-known and widely used phenomenological models. They were originally developed to describe rate-independent hysteresis, which refers to a static memory effect. However, as previously mentioned, piezoelectric materials exhibit rate-dependent hysteresis. For such materials, Preisach and PI models could yield considerable errors under inputs applied at varying rates (42).

It has been reported in literature that hysteretic effects can be modeled in series with the dynamics of the considered device. That is to say, the output of the rateindependent hysteresis model is the input of the dynamic model (43). Instead of separately modeling the two interacting dynamic effects, some solutions were evaluated to treat their combined effects phenomenologically and formulate modified rate-dependent models able to take into account hysteresis non linearity at varying excitation frequencies (44, 45). Most of the above mentioned modifications are focused on the Preisach model. They are based on including input rate of change in the density functions. PI model offers a further benefit, since not only the density functions but also the *play* and *stop* operators are allowed to be redefined (42). However, these highly specialized operators work only for limited cases (1, 46, 47).

As previously clarified, phenomenological models are inherently based on observed phenomena and cannot predict physical behavior resulting from material microscopic dynamics.

Physics-based techniques, on the other hand, are derived from the material underlying physics and are combined with empirical factors to describe observed

nonlinear behaviors (48).

With reference to ferroelectric materials, this second approach is based on describing the switching process at the crystal lattice scale.

In (49, 50, 51, 52, 53, 54, 55), a free energy model, addressing the ferroelectric switching as a process based on thermal activation, is presented. The approach, motivated by the shape memory alloy model developed in (56, 57, 58, 59), is based on a one-dimensional Helmholtz free energy potential Ψ presenting two convex energy wells and a concave energy barrier between the wells. Potential Ψ is expressed as a sole function of the polarization. Depending on the applied electric field, unit cells jump from a well to another as a results of a competition between thermal activation and energy barriers.

In this Thesis, an extended version of this pure polarization model is employed (1, 60, 61). Developed for single crystal piezoceramics, the model includes a 1-D strain component and a corresponding 90°-variant. Moreover, it is capable of predicting the rate-dependent hysteretic behavior.

A description of the adopted model is provided in the following subsection.

3.3.2 Physics-based one-dimensional model of a PZT crystal

Figure 3.4 reports a scan image of a PZT polycrystalline specimen at the mesoscale. It can be seen that the structure of each crystal is organized in layers, called *domains*. We will focus our interest on mono-crystalline PZT materials.

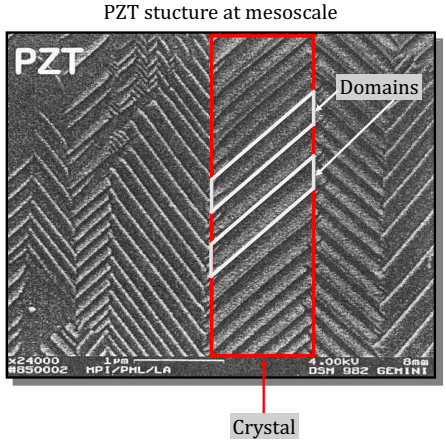

Figure 3.4: Structure of a PZT material specimen at the mesoscale.

Let us consider a macroscopic piezoceramic material volume according to Fig. 3.5-a, where w, l, t are respectively the width, the length and the thickness of the considered block.

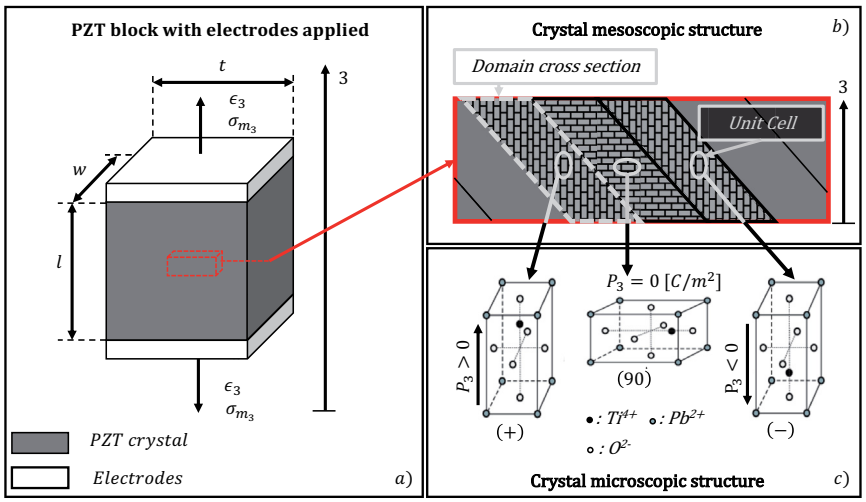

Figure 3.5: a) PZT monocrystalline block with electrodes applied. ϵ_3 and σ_{m_3} are the strain and the mechanical stress along axis 3, respectively ; b) mesoscopic structure of the PZT crystal; c) microscopic structure of the PZT crystal. P_3 is the polarization along axis 3.

The 1-D nonlinear model adopted in this work relies on the assumption that each domain (ref. Fig. 3.5-b) consists in a number of equally poled (i.e. oriented) unit cells. Unit cells (and by extension domains) can exist in three differently oriented variants: namely (+), (−), and (90), depending on whether the Ti^{4+} ion is displaced upward, downward or perpendicularly with respect to the center of symmetry (ref. Fig. 3.5-c). Domain switching is triggered by the applied stress and electric field along direction 3.

Starting from the definition of the Gibbs free energy density (g) for the system depicted in Fig. 3.5-a, domain switching probabilities can be determined through statistical thermodynamic arguments.

The model assumes the following paraboloid representation for the Gibbs free energy density associated to the j^{th} variant:

$$g_j = \frac{\eta_j}{2}(\sigma_e - \sigma_{e_{j,0}})^2 + \mu_j(\sigma_e - \sigma_{e_{j,0}})(\epsilon_3 - \epsilon_{j,0}) + \frac{Y_j}{2}(\epsilon_3 - \epsilon_{j,0})^2 - E_3\sigma_e - \sigma_{m_3}\epsilon_3 \ , \quad \text{for } j = (+), (-), (90) \ , \tag{3.1}$$

where η_j, μ_j, Y_j, $\sigma_{e_{j,0}}$, and $\epsilon_{j,0}$ are, respectively, the electric permittivity reciprocal, the coupling coefficient, the Young's modulus, the remnant charge, and the remnant strain associated to the j^{th} variant. Moreover, σ_e is the charge density related to the electrical current entering the system ($\dot{q}_e = \dot{\sigma}_e wl$) and ϵ_3 is the crystal strain along direction 3.

As it can be inferred from (3.1), the energy content associated to each variant depends on the applied electric field (E_3) and the mechanical stress (σ_{m_3}) along direction 3. The expected average strain and charge density associated to a domain in the j^{th} variant can be evaluated by searching for the minimum point of the relative energy density paraboloid:

$$\begin{cases} \frac{\partial g_j}{\partial \sigma_e} = 0 \\ \frac{\partial g_j}{\partial \epsilon_3} = 0 \end{cases} \implies \begin{cases} \left\langle \sigma_{e_j} \right\rangle = \frac{Y_j E_3 - \mu_j \sigma_{m_3}}{\eta_j Y_j - {\mu_j}^2} + \sigma_{e_j,0} \\ \left\langle \epsilon_{3_j} \right\rangle = \frac{\eta_j \sigma_{m_3} - \mu_j E_3}{\eta_j Y_j - {\mu_j}^2} + \epsilon_{j,0} \end{cases} . \tag{3.2}$$

Quantities $\left\langle \epsilon_{3_j} \right\rangle$ and $\left\langle \sigma_{e_j} \right\rangle$ represent the contribution due to a single domain to the overall crystal strain (ϵ_3) and to the overall charge density (σ_e), respectively.

In order to reproduce the global electromechanical response of the material, the model must be able to predict not only how many domains exist in the j^{th} variant when a given input excitation (E_3, σ_{m_3}) is applied, but also how many domains switch from a variant to another if a change in the input excitation occurs.

The crystal mesoscopic configuration can be mapped by the following three variables, called Phase Fractions (PFs):

$$x_j = \frac{N_j}{N} \in [0,1], \quad \text{for } j = (+), (-), (90) \tag{3.3}$$

where N is the total number of domains in the crystal and N_j is the number of domains in the j^{th} variant.

Since the following consistency equation holds:

$$\sum_j x_j(t) = 1, \quad \forall t \tag{3.4}$$

only two independent PFs are needed for reconstructing the crystal mesoscopic structure in time.

PFs kinetics is then expressed by the following set of Ordinary Differential Equations (ODEs):

$$\begin{cases} \dot{x}_+ = -x_+ p_{[+,90]} + x_{90} p_{[90,+]} \\ \dot{x}_- = -x_- p_{[-,90]} + x_{90} p_{[90,-]} \end{cases} , \tag{3.5}$$

where $x_{90} = (1 - x_+ - x_-)$.

The generic quantity $p_{[j,k]}$ represents the probability that a domain switches from the j^{th} to the k^{th} variant. Transition probabilities can be evaluated as (60):

$$p_{[j,k]} = \frac{1}{\tau_{x_{[j,k]}}} exp\left(-\frac{v_l \Delta g_{[j,k]}}{k_B T} \right), \tag{3.6}$$

where $\Delta g_{[j,k]}$ is the energy barrier that a domain has to overcome in order to switch from the j^{th} to the k^{th} variant. To improve computational efficiency, energy barrier can be expressed as a function of a *driving force* $F(E_3, \sigma_{m_3})_{[j,k]} = min\{g_j\} - min\{g_k\}$ and a material parameter Δg_0, which has to be appropriately chosen (see (26, 60) for further details). Moreover, parameter $1/\tau_{x_{[j,k]}}$ in (3.6) represents the frequency at which, due to thermal activation, lattice domains attempt to cross the relative barrier; T is the constant crystal temperature; k_B is the Boltzmann constant; and v_l is the volume of a domain.

By knowing the evolution in time of PFs as a function of the input excitation (through (3.5)), it is possible to write the crystal constitutive equations as follows:

$$\begin{cases} \sigma_e(E_3, \sigma_{m_3}) = x_+ \left\langle \sigma_{e_+} \right\rangle + x_- \left\langle \sigma_{e_-} \right\rangle + x_{90} \left\langle \sigma_{e_{90}} \right\rangle \\ \epsilon_3(E_3, \sigma_{m_3}) = x_+ \left\langle \epsilon_{3_+} \right\rangle + x_- \left\langle \epsilon_{3_-} \right\rangle + x_{90} \left\langle \epsilon_{3_{90}} \right\rangle \end{cases} . \tag{3.7}$$

Equation set (3.7), along with (3.5), expresses the *strain-charge* form of the PZT crystal nonlinear model. By substituting (3.2) into (3.7), a more common form can be achieved through appropriate manipulations.

The complete PZT material hysteretic model, expressed in the *strain-charge* form, is than given by the following set of Differential and Algebraic Equations (DAEs):

$$\begin{cases} \dot{x}_+ = -x_+ p(E_3, \sigma_{m_3})_{[+,90]} + x_{90} p(E_3, \sigma_{m_3})_{[90,+]} \\ \dot{x}_- = -x_- p(E_3, \sigma_{m_3})_{[-,90]} + x_{90} p(E_3, \sigma_{m_3})_{[90,-]} \\ \sigma_e = a(x_+, x_-) E_3 + b(x_+, x_-) \sigma_{m_3} + c(x_+, x_-) \\ \epsilon_3 = b(x_+, x_-) E_3 + d(x_+, x_-) \sigma_{m_3} + f(x_+, x_-) \end{cases} , \tag{3.8}$$

where quantities a, b, c, d, and f are nonlinear functions of the PFs.

It results that:

- $a(x_+, x_-)$ has the dimension of the electrical permittivity;
- $b(x_+, x_-)$ has the dimension of the coupling coefficient reciprocal;
- $c(x_+, x_-)$ is a charge density depending on the remnant charge densities associated to each variant;
- $d(x_+, x_-)$ has the dimension of a flexibility term;
- $f(x_+, x_-)$ is a non-dimensional quantity depending on the remnant strains associated to each variant.

Note that (3.8) coincide with the linear eq. set (2.219) if: PFs dynamic is suppressed (i.e., $[\dot{x}_+, \dot{x}_-] = 0^T$), and residual terms c and f are set equal to zero.

With reference to DAE (3.8), it is worth to highlight that there is no dependence of the differential variables (x_+, x_-) on the algebraic ones (σ_e, ϵ_3).

Therefore, in order to obtain other forms of the nonlinear constitutive model, it is possible to manipulate the algebraic equations in (3.8) without this resulting in any change of the material internal dynamics (as it will be shown in the following subsection).

Other forms of the nonlinear material model are hereafter reported:

- *strain-field* form:

$$\begin{cases} \dot{x}_+ = -x_+ p(\sigma_{m_3}, \sigma_e)_{[+,90]} + x_{90} p(\sigma_{m_3}, \sigma_e)_{[90,+]} \\ \dot{x}_- = -x_- p(\sigma_{m_3}, \sigma_e)_{[-,90]} + x_{90} p(\sigma_{m_3}, \sigma_e)_{[90,-]} \\ \epsilon_3 = \frac{ad-b^2}{a}\sigma_{m_3} + \frac{b}{a}\sigma_e + \frac{af-bc}{a} \\ E_3 = -\frac{b}{a}\sigma_{m_3} + \frac{1}{a}\sigma_e - \frac{c}{a} \end{cases} ; \tag{3.9}$$

- *stress-charge* form:

$$\begin{cases} \dot{x}_+ = -x_+ p(\epsilon_3, E_3)_{[+,90]} + x_{90} p(\epsilon_3, E_3)_{[90,+]} \\ \dot{x}_- = -x_- p(\epsilon_3, E_3)_{[-,90]} + x_{90} p(\epsilon_3, E_3)_{[90,-]} \\ \sigma_{m_3} = \frac{1}{d}\epsilon_3 - \frac{b}{d}E_3 - \frac{f}{d} \\ \sigma_e = \frac{b}{d}\epsilon_3 + \frac{ad-b^2}{d}E_3 + \frac{cd-bf}{d} \end{cases} ; \tag{3.10}$$

- *stress-field* form:

$$\begin{cases} \dot{x}_+ = -x_+ p(\epsilon_3, \sigma_e)_{[+,90]} + x_{90} p(\epsilon_3, \sigma_e)_{[90,+]} \\ \dot{x}_- = -x_- p(\epsilon_3, \sigma_e)_{[-,90]} + x_{90} p(\epsilon_3, \sigma_e)_{[90,-]} \\ \sigma_{m_3} = \frac{a}{ad-b^2}\epsilon_3 - \frac{b}{ad-b^2}\sigma_e - \frac{af-bc}{ad-b^2} \\ E_3 = -\frac{b}{ad-b^2}\epsilon_3 + \frac{d}{ad-b^2}\sigma_e + \frac{bf-cd}{ad-b^2} \end{cases} . \tag{3.11}$$

With reference to EH devices, to which an input mechanical stress is provided in order to produce an electric field or a charge output, *stress-charge* and *stress-field* forms turn out to be the most suitable modeling choices.

3.3.3 Simulation results

In order to show the model capability of catching rate-dependent hysteretic behaviors, quasi-static simulations are reported in this Section.

Table 3.1 summarizes crystal parameters, which has been chosen as in (1). The identification of such parameters is based on experimental tests performed on a stack actuator made of soft PZT (PIC-151).

Table 3.1: PZT Crystal Parameters(1)

Parameter	Value	Dim.	Parameter	Value	Dim.
$\eta_{\pm};\ \eta_{90}$	4.7e07; 6.5e07	$\left[\frac{m}{F}\right]$	$\sigma_{e_{\pm,0}};\ \sigma_{e_{90,0}}$	$\pm$0.23; 0.0	$\left[\frac{C}{m^2}\right]$
$\mu_{\pm};\ \mu_{90}$	$\mp$7.5e08; 0.0	$\left[\frac{N}{C}\right]$	$\epsilon_{\pm,0};\ \epsilon_{90,0}$	1.5e-3; -0.5e-3	$[-]$
$Y_{\pm};\ Y_{90}$	60; 65	$[GPa]$	$\tau_{x_{[\pm,90]}};\ \tau_{x_{[90,\pm]}}$	4.3e-3; 3.1e-3	$[s]$
vl	4e-24	$\left[m^3\right]$	T	293	$[K]$
Δ_{g_0}	33.5e3	$[Pa]$	ρ	7500	$\left[\frac{kg}{m^3}\right]$

Fig. 3.6 reports simulations of model (3.8) carried out driving the PZT crystal with the following input quantities: sinusoidal electric field (E_3) having 0.5 MV/m amplitude and 0.01 Hz frequency; null stress ($\bar{\sigma}_{m_3} = 0\ Pa$).

It can be noticed the role of the material parameter Δg_0 in the resulting shape of the hysteresis loop. With reference to the left-handed side of Fig. 3.6, a decrease in Δg_0 results in a decrease of the hysteresis loop area. This means that the electric field amplitude required to trigger crystal switching between its two linear operating regions (i.e. $x_+ = 1$ and $x_- = 1$ regions in Fig. 3.6) is lower for lower Δg_0. As a consequence of that, a crystal characterized by smaller hysteresis areas will exhibit nonlinear behavior for input varying in ranges where crystals with wider hysteresis (i.e. higher Δg_0) operate linearly.

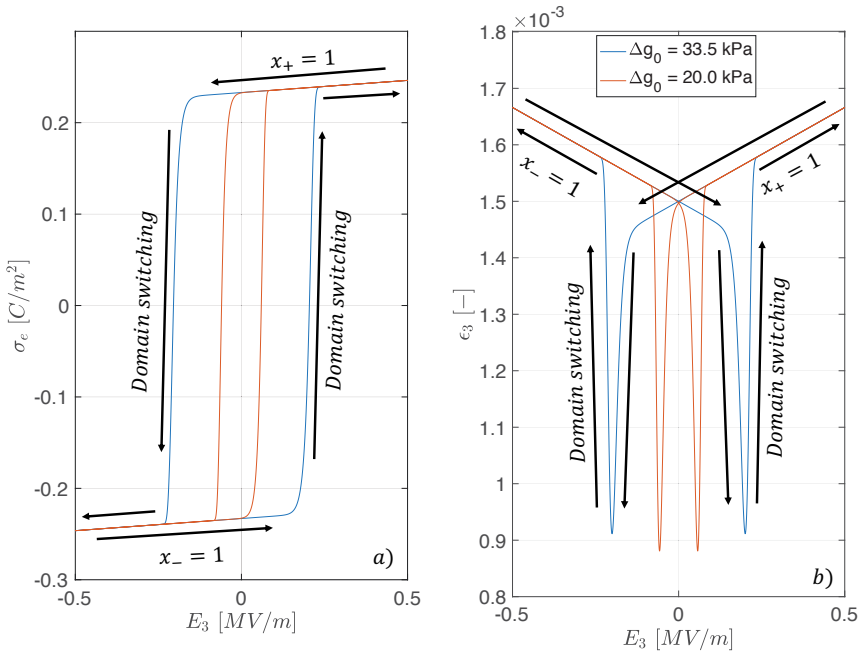

Figure 3.6: Crystal hysteresis under purely electrical load: role of the parameter Δg_0. Sinusoidal input excitation frequency: 0.01 Hz.

With reference to the red curves reported in Fig. 3.6 (hysteretic loops for $\Delta g_0 = 22\ kPa$), evolutions in time of crystal PFs, charge density and strain are reported in Fig. 3.7-b, Fig. 3.7-c, and Fig. 3.7-d, respectively. It can be seen how ranges where the crystal operates linearly are characterized by constant mesoscopic configurations ($[\dot{x}_+, \dot{x}_-] = \bar{0}^T$).

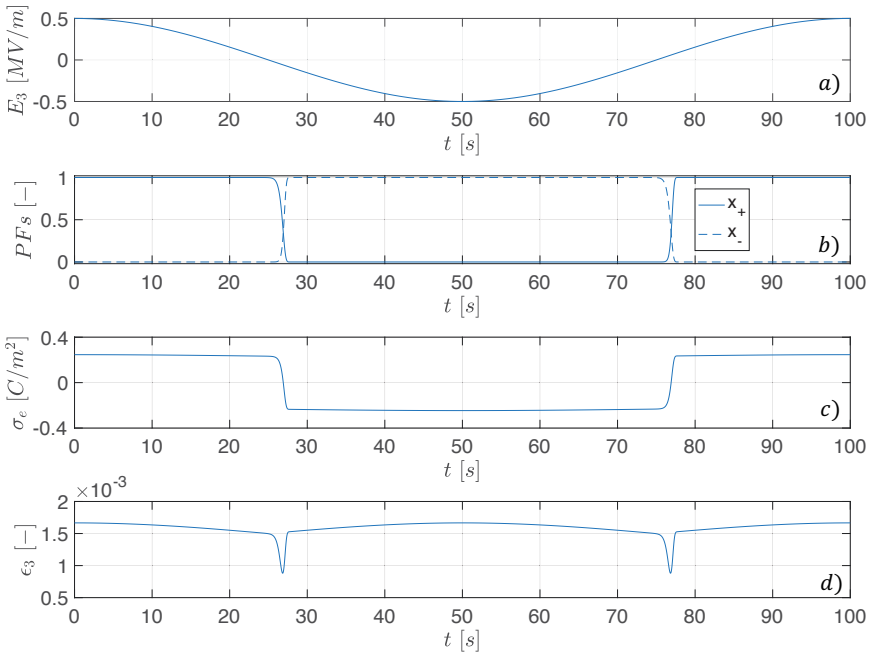

Figure 3.7: Evolution in time of: a) the electric field E_3; b) crystal PFs; c) the surface charge density; d) the crystal strain; relative to the red hysteretic loop ($\Delta g_0 = 22\ kPa$) reported in Fig. 3.6.

Figure 3.8 reports a comparison between predictions of the nonlinear model considered in two different forms: namely, *strain-charge* (3.8) and *strain-field* (3.9) forms. Blue solid curves show hysteretic loops obtained through the simulation of model (3.8) under a slow sinusoidal electrical load (signal in Fig. 3.7-a) and a null mechanical stress. Red dashed curves refers to simulations of model (3.9), carried out providing the charge density reported in Fig. 3.7-c and a null stress as inputs. The perfect overlapping of the reported curves confirms the equivalence of the *strain-charge* and the *strain-field* forms of the presented nonlinear model. The above mentioned equivalence can be assumed for all the other forms, by extension.

Finally, Fig. 3.9 reports the hysteretic response of the crystal for different rates of the input electric field: namely 0.01 Hz and 5.00 Hz. Simulation results show that the model is able to predict the dependence of the hysteresis loop on the input excitation frequency (26).

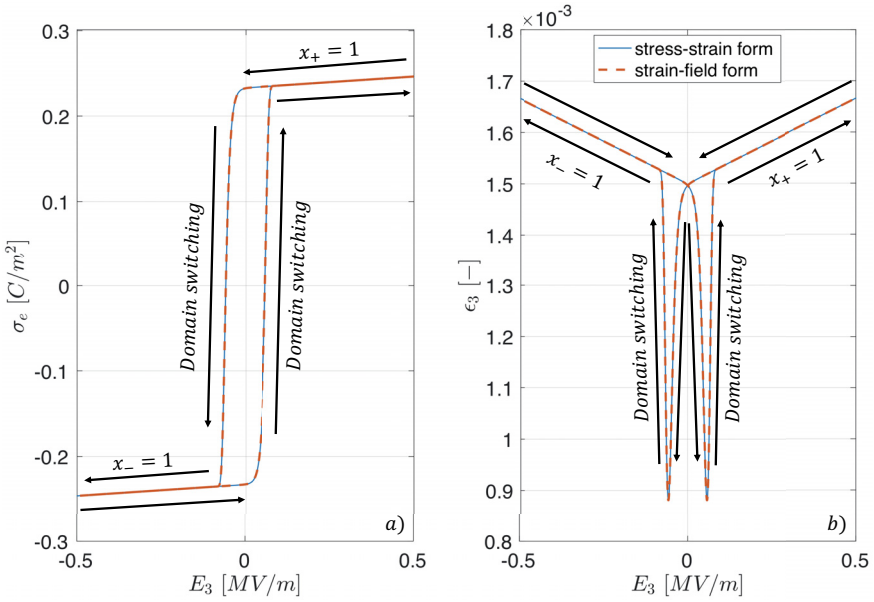

Figure 3.8: Crystal hysteresis loops. Blue solid curves and red dashed curves refer to the simulation of the material model in the *strain-charge* and the *strain-field* forms respectively, under the same operative conditions.

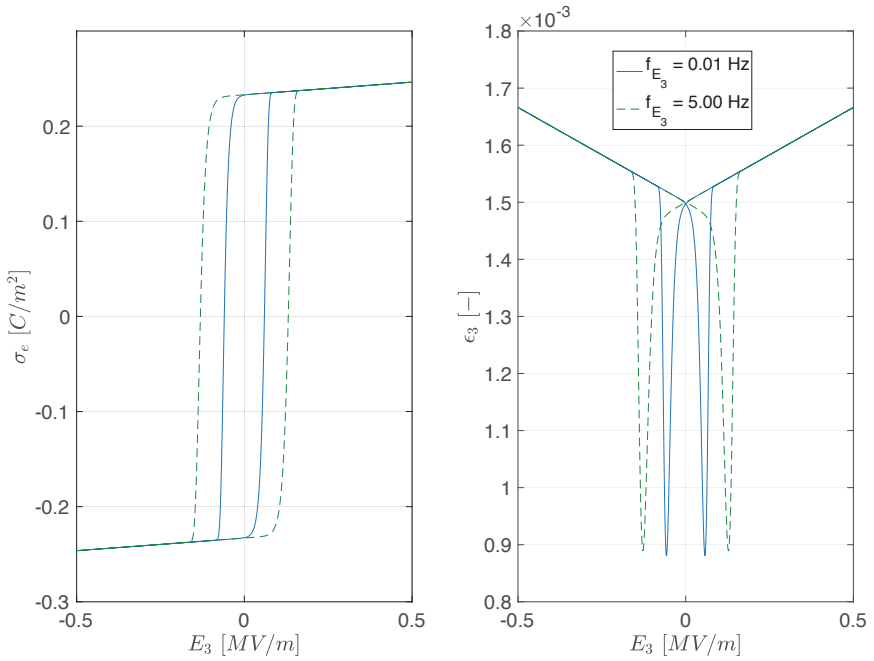

Figure 3.9: Crystal hysteresis loop for different frequencies of the input electric field.

3.4 Effects of PZT crystal nonlinearities on the dynamics of EH devices

With the aim of investigating the role of material nonlinearities on performances of vibrating harvester devices, a multi-scale approach is adopted to comprise hysteretic effects in the dynamic response of two different type of piezoelectric devices. Cases taken into account are: EH device working in d_{33} mode (62, 63), EH device working in d_{31} mode (64). Both devices are modeled as a SDOF systems.

For the d_{33} case, the classical linear model is first presented, along with its equivalent lumped circuit representation. This is done with the major aim of providing an effective comparison with the following nonlinear approach .

3.4.1 EH device working in d_{33} mode

A schematic representation of the considered device is reported in Fig. 3.10-a. It consists in a PZT volume that is fixed on a moving base and presents a tip mass M_{Tip} on top. The electrodes, which have a negligible thickness t_e, are placed as depicted in Fig. 3.10-a.

Figure 3.10-b shows a sketch of the device SDOF model. A base acceleration ($\ddot{z}_b$) puts the system equivalent mass (m) into an oscillatory motion along z direction. Mass oscillations result in a mechanical stress (σ_{m_3}) for the PZT crystal, which consequently injects an electric current (i_{R_L}) in the resistive load (R_L) connected to the electrodes.

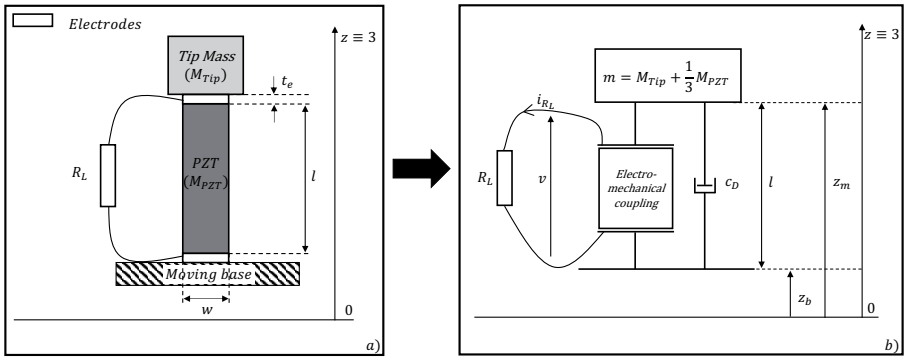

Figure 3.10: a) schematic representation of the PZT harvester device; b) sketch of the device SDOF model.

The electro-mechanical dynamics of the system is described by a set of two

ODEs. The first one is given by the second Newton's Law for the mass m:

$$m\ddot{z}_m = -F_D - F_{PZT}, \tag{3.12}$$

where F_D, and F_{PZT} are the reaction forces generated by the the damper, and the piezoceramic element respectively. If l_0 is the PZT wire initial length, by considering the following relations:

$$l = z_m - z_b; \quad \eta = l - l_0; \quad F_D = c_D\dot{l} = c_D\dot{\eta}\ ; \tag{3.13}$$

where c_D is a damping coefficient, equation (3.12) can be recast as follows:

$$m\ddot{\eta} + c_D\dot{\eta} + F_{PZT} = -m\ddot{z}_b = F_b\ . \tag{3.14}$$

The second ODE can be obtained by determining the current provided to the resistive load:

$$i_{R_L}(t) = \frac{v(t)}{R_L}\ , \tag{3.15}$$

where $v(t)$ is the device ouput voltage (Fig. 3.10-b).

In the following Subsections, the derivation of the complete device model - through the coupling of the PZT material model with dynamic equations (3.14) and (3.15) - is presented for both the linear and nonlinear case. An equivalent lumped circuit representation is also reported. Moreover, some implementation issues are discussed.

3.4.1.1 Linear model

Assuming small deformations, the expressions of F_{PZT} and i_{R_L}, in (3.14) and (3.15) respectively, can be obtained by multiplying both sides of the crystal linear constitutive equations (2.220) by the electrodes surface ($A = wt$) and considering the following relations between intensive and extensive quantities:

$$\epsilon_3 = \frac{\eta}{l_0}; \quad E_3 = \frac{v}{l_0}; \quad i_{R_L} = -A\dot{D}_3\ . \tag{3.16}$$

Finally, the overall system model is given by the following set of linear time-invariant ODEs:

$$\begin{cases} m\ddot{\eta} + c_D\dot{\eta} + \frac{Ac_{33}}{l_0}\eta - \frac{Ad_{33}}{l_0}v = F_b \\ \frac{A\varepsilon_{33}}{l_0}\dot{v} + \frac{Ad_{33}}{l_0}\dot{\eta} + \frac{1}{R_L}v = 0 \end{cases}\ , \tag{3.17}$$

which will be hereafter referred to as Linear Time-Invariant Model (LTIM).

Figure 3.11 reports the equivalent lumped circuit representation of the LTIM. It consists of a two-port electrical circuit where the provided mechanical power ($p_m = F_b\dot{\eta}$) is converted into the electrical power absorbed by the resistive load ($p_e = vi_{R_L}$). The coupling between the mechanical and the electrical ports, which represents the energy conversion process (from the mechanical form to the electrical one), has been taken into account through a voltage-controlled voltage source and a current-controlled current source, both having the same constant gain[1]:

$$\alpha^{LTIM} = \frac{Ad_{33}}{l_0} \ . \tag{3.18}$$

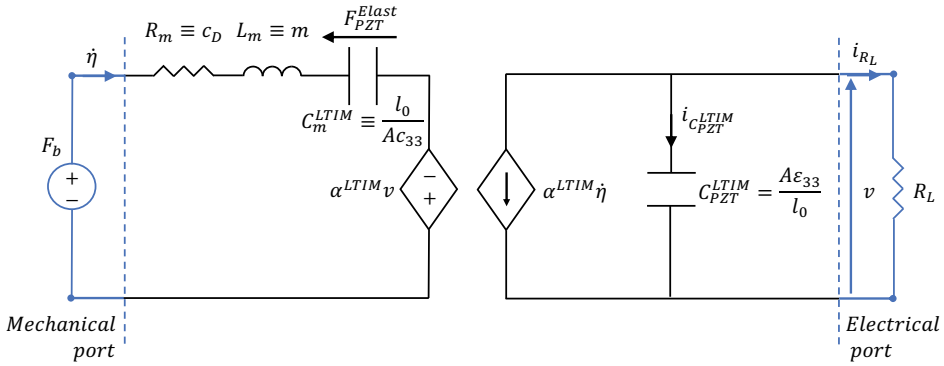

Figure 3.11: Lumped circuit representation for the LTIM of the system.

All the circuit components in Fig. 3.11 are characterized by constant values. As a consequence, under the assumption of sinusoidal input excitation, it can be inferred (just by visual inspection of the circuit) that the energy entering the mechanical port of the device is allocated as follows:

- a part is dissipated by viscous effects (relative to the resistor R_m);
- a part is stored in the system as kinetic and elastic energy (relative to the inductor L_m and the capacitor C_m^{LTIM} respectively);
- part of the energy converted into the electrical form is stored in the system as electrostatic energy (absorbed by the capacitor C_{PZT}^{LTIM});
- the remaining part is made available at the electrical port.

[1]Note that this representation of the coupling between the two ports coincides with an ideal transformer having a voltage ratio equal to α^{LTIM}.

3.4.1.2 Nonlinear Multi-scale Model

By analogy with the linear case, we present the derivation of the device nonlinear model through the coupling of the crystal constitutive equations (3.10) - expressed in the *stress-charge* form - with the device dynamics. This is mostly aimed at achieving an equivalent lumped circuit representation allowing for an immediate comparison with the linear one (depicted in Fig. 3.11), which has been widely reported in literature.

As it will emerge from the discussion, the implementation of the resultin Multi-scale Model (MsM) presents a critical aspect, due to the *anticausal* nature of the coupling between the material internal dynamics and the device dynamics. The derivation of a model based on a *causal* coupling is then presented.

Anticausal coupling based MsM : As for the linear case, by multiplying both sides of (3.10) by A and taking into account (3.16) - where now $I_{R_L} = -A\dot{\sigma}_e$ - the complete system model results in the following set of nonlinear time-variant ODEs:

$$\begin{cases} m\ddot{\eta} + c_D\dot{\eta} + \frac{A}{l_0 d(x_+,x_-)}\eta - \frac{Ar(x_+,x_-)}{l_0}v - \frac{Af(x_+,x_-)}{d(x_+,x_-)} = F_b \\ \frac{A}{l_0}h(x_+,x_-)\dot{v} + \left[\frac{1}{R_L} + \frac{A}{l_0}\dot{h}(x_+,x_-)\right]v + \frac{Ar(x_+,x_-)}{l_0}\dot{\eta} + ... \\ \qquad ... + \frac{A}{l_0}\dot{r}(x_+,x_-)\eta + A\dot{g}(x_+,x_-) = 0 \\ \dot{x}_+ + x_+ p(\eta,v)_{[+,90]} - (1 - x_+ - x_-)p(\eta,v)_{[90,+]} = 0 \\ \dot{x}_- + x_- p(\eta,v)_{[-,90]} - (1 - x_+ - x_-)p(\eta,v)_{[90,-]} = 0 \end{cases}, \tag{3.19}$$

where: $h = (ad - b^2)/d$; $g = (cd - bf)/d$; $r = b/d$.

Equation set (3.19) represents a multi-scale model, as variables defined at the material scale (x_+, x_-) and variables defined at the device scale (η, v) are mutually influenced.

It is worth to highlight how the LTIM results from MsM if:

- the kinetic of PFs (i.e. the source of the crystal nonlinear behavior) is suppressed. With reference to (3.19), this implies that:

$$\begin{cases} \dot{x}_+ = 0 \\ \dot{x}_- = 0 \end{cases} \implies \left[\dot{d}, \dot{f}, \dot{g}, \dot{h}, \dot{r}\right]^T = \bar{0}^T; \tag{3.20}$$

- the crystal is characterized by null remnant strain along direction 3: $f(x_+, x_-) = 0$.

Figure 3.12 depicts the equivalent lumped circuit representation of the MsM. Differently from LTIM, all the circuit components change in time as nonlinear functions of the PFs - except for the ones related to the constant mechanical parameters (R_m and L_m) and the constant resistive load R_L. The coupling between the two ports is taken into account by means of three controlled generators. Two of them, are characterized by the same time variant gain (α^{MsM}), which is now a nonlinear function of both crystal coupling coefficient and Young's modulus (with reference to (3.8), quantities $Y_{PZT} = d^{-1}$ and b^{-1} respectively):

$$\alpha^{MsM}(t) = \frac{Ar}{l_0} = \frac{Ab}{l_0 d} \ . \tag{3.21}$$

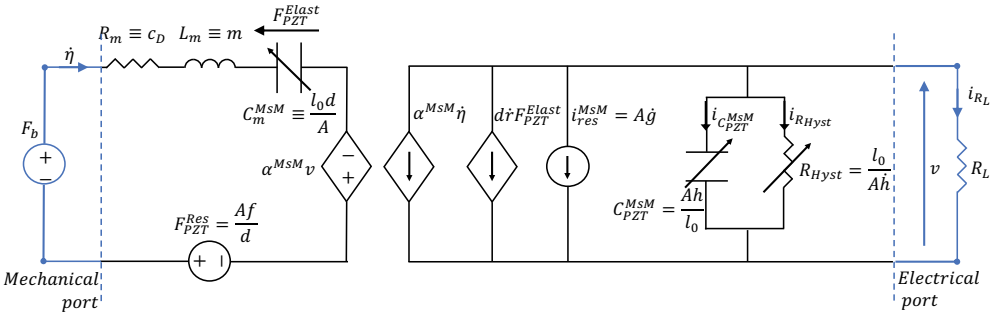

Figure 3.12: Lumped circuit representation of the anticausal coupling based MsM.

Due to the domain switching process, a third controlled current generator results connected to the electrical port. It is driven by the elastic term of the PZT reaction force:

$$F_{PZT}^{Elast}(t) = \frac{A}{l_0 d}\ \eta \ , \tag{3.22}$$

and its transconductance depends on the rate of change of both the material Young's modulus and coupling coefficient.

The capacitor connected to the electrical port is now a nonlinear function of three crystal properties: the permittivity (i.e. parameter a in eq. set (3.8)), the coupling coefficient and the Young's modulus. The analytical expression of the capacitance C_{PZT}^{MsM} is given by the following:

$$C_{PZT}^{MsM}(t) = \frac{A}{l_0} h = \frac{A}{l_0}\left(a - \frac{b^2}{d}\right) \ . \tag{3.23}$$

Due to the changing mesoscopic structure of the crystal, a time variant ohmic component (R_{Hyst}) appears in the side of the circuit connected to the electrical port. Resistance R_{Hyst} is a function of the PFs' rate of change and accounts for a portion of the losses related to mechanical and dielectric hysteresis:

$$R_{Hyst}(t) = \frac{l_0}{A\dot{h}} \ . \tag{3.24}$$

Finally, two independent generators appear in the equivalent circuit of the MsM. The first one, related to the mechanical port, represents the residual term of the PZT reaction force (F_{PZT}^{Res}). The second one, connected to the electrical port, is a current generator related to the rate of change of the PZT material residual charge density and residual stress (with reference to (3.8), quantities c and f respectively).

It is worth to highlight that the variable nature of circuital components accounting for the elastic and the electrostatic energy stored in the system (C_m^{MsM} and C_{PZT}^{MsM} respectively), results in the relative absorption of instantaneous powers having mean values different from zero[1]. Depending on the operative condition of the device (i.e. waveform and harmonic content of the input acceleration), these mean powers can assume positive or negative values. As a consequence, dissipative phenomena (related to mechanical and dielectric hysteresis) or active power injection might be associated with capacitances C_m^{MsM} and C_{PZT}^{MsM}. In both cases, the power balance is ensured by the complementary role of the independent and controlled generators present in the circuit.

As previously mentioned, MsM (3.19) allows for an immediate comparison with the classical model (3.17), derived from the PZT linear constitutive equations. Moreover, it easily leads to an equivalent lumped circuit that provides an effective visualization of the role that the material mesoscopic evolution has on the transduction process.

Its implementation, however, presents a critical aspect. This can be inferred from Fig. 3.13, where the coupling between the scales involved in the model is depicted in the form of a block diagram. With reference to the red feedback

[1]Note that in nonlinear regimes even the instantaneous power related to time-invariant circuital components (as is the case for the inductor in Fig. (3.12)) is characterized by a non-null mean value.

loop in Fig. 3.13, it can be seen that the implementation of equation set (3.19) requires the numerical computation of σ_e time-derivative, in order to evaluate the device output current i_{R_L} and, finally, the electric field applied to the PZT material ($E_3 = i_{R_L} R_L / l_0 = -A\dot{\sigma}_e R_L / l_0$).

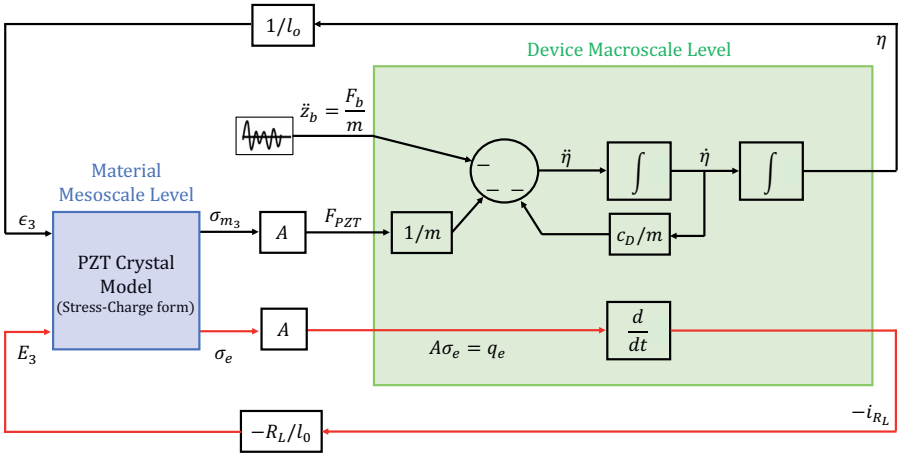

Figure 3.13: Implementation block diagram of the anticausal coupling based MsM.

The above mentioned difficulty can be overcome by recasting the PZT constitutive equation in a form that allows for a causal coupling between the models at the two scales: the *stress-field* form (3.11).

Causal coupling based MsM : Starting from the PZT *stress-field* constitutive equation, by the same procedure previously adopted for the anticausal coupling based MsM, the following nonlinear time-variant model can be obtained:

$$\begin{cases} m\ddot{\eta} + c_D\dot{\eta} + \frac{A}{l_0}p^{SF}\eta - Ah^{SF}\sigma_e - Ag^{SF} = F_b \\ A\dot{\sigma}_e + \frac{l_0}{R_L}r^{SF}\sigma_e - \frac{h^{SF}}{R_L}\eta + \frac{l_0}{R_L}w^{SF} = 0 \\ \dot{x}_+ + x_+ p(\eta,\sigma_e)_{[+,90]} - (1 - x_+ - x_-)p(\eta,\sigma_e)_{[90,+]} = 0 \\ \dot{x}_- + x_- p(\eta,\sigma_e)_{[-,90]} - (1 - x_+ - x_-)p(\eta,\sigma_e)_{[90,-]} = 0 \end{cases} \tag{3.25}$$

where superscripts "SF" refers to quantities derived from the *stress-field* PZT constitutive equations and:

$$\begin{aligned} g^{SF} &= \frac{af - bc}{ad - b^2}\ ; & h^{SF} &= \frac{b}{ad - b^2}\ ; & p^{SF} &= \frac{a}{ad - b^2}\ ; \\ r^{SF} &= \frac{d}{ad - b^2} = \frac{1}{h}\ ; & w^{SF} &= \frac{bf - cd}{ad - b^2}\ . \end{aligned} \tag{3.26}$$

Figure 3.14 reports the equivalent lumped circuit representation of the model (3.25).

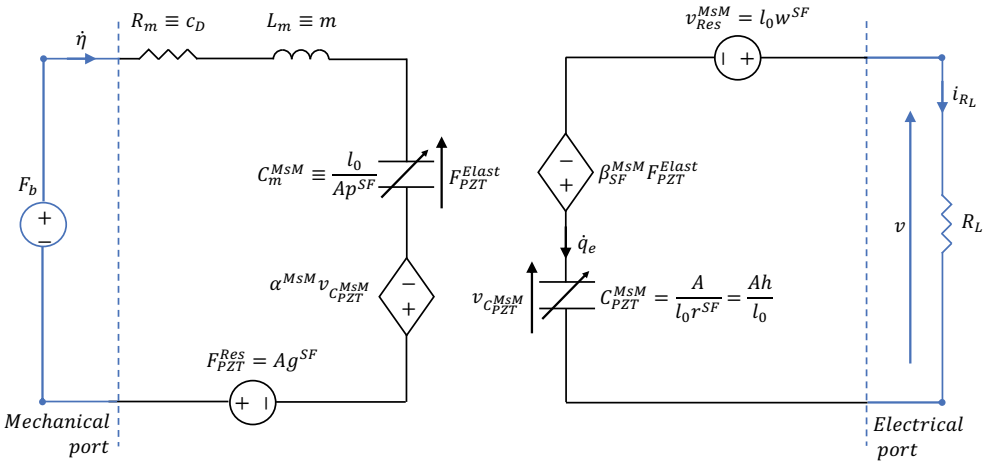

Figure 3.14: Lumped circuit representation of the causal coupling based MsM.

In this representation of the device, the coupling between the ports is taken into account by two voltage-controlled voltage generators. In analogy with the previous case, the controlled generator connected to the mechanical port presents a gain expressed by (3.21) and is driven by the voltage [1] on the PZT variable capacitor defined by (3.23).

The controlled generator accounting for the energy transferred to the electrical port is characterized by a gain (β_{SF}^{MsM}) depending on crystal coupling coefficient and permittivity:

$$\beta_{SF}^{MsM}(t) = \frac{l_0}{A}\frac{h^{SF}}{p^{SF}} = \frac{l_0 b}{Aa} \ . \tag{3.27}$$

Moreover, it is driven by the elastic component of the PZT crystal reaction force, which is now given by:

$$F_{PZT}^{Elast} = \frac{A}{l_0} p^{SF} \eta \ . \tag{3.28}$$

The implementation of model (3.25) does not involve the computation of numerical time derivatives, since it allows for evaluating the PZT input charge density through the time-integration of the applied electric field: $\sigma_e = -\frac{l_0}{AR_L}\int E_3 \, \mathrm{d}t$ (see the blue feedback loop in Fig. 3.14).

Despite the significant difference in the topology of circuits reported in Fig. 3.12 and Fig. 3.14, MsMs (3.19) and (3.25) - which describe the same device

[1] Note that, in this representation of the system, the voltage on C_{PZT}^{MsM} differs from the device output voltage (see Fig. 3.14).

- are equivalent in terms of external (i.e. input/output) behavior. In fact, provided the same input quantities (F_b, $\dot{\eta}$) to the mechanical port, both models predict the same outputs (i_{R_L}, v) at the electrical port (see Appendix A).

Therefore, simulations reported in this work have been performed through the numerical integration of the MsM (3.25).

In order to show the effect of hysteretic nonlinearities on the device dynamic response, the numerical integration of the following ODE set has also been preformed:

$$\begin{cases} m\ddot{\eta} + c_D\dot{\eta} + \frac{A}{l_0}p^{SF}\eta - Ah^{SF}\sigma_e - Ag^{SF} = F_b \\ A\dot{\sigma}_e + \frac{l_0}{R_L}r^{SF}\sigma_e - \frac{h^{SF}}{R_L}\eta + \frac{l_0}{R_L}w^{SF} = 0 \\ \dot{x}_+ = 0 \\ \dot{x}_- = 0 \end{cases} . \tag{3.29}$$

Model (3.29), which will be hereafter referred to as Time-Invariant Model (TIM), results from (3.25) when PFs' kinetics are suppressed.

3.4.1.3 Simulation results

Table 3.2 reports the parameters of the device adopted as case study in this work. It consists on a PZT volume, which has dimensions comparable with the elementary cell of a piezoceramic nanogenerator (65).

Table 3.2: Harvester Device Parameters

PZT Volume Geometrical Parameters	Value	Dim.
Originary Length (l_0); Width (w)	5; 0.5	$[\mu m]$
Cross sectional area ($A = w^2$)	0.25	$[\mu m^2]$

SDOF Model Parameters	Value	Dim.
Tip Mass (M_{Tip})	0.255	$[\mu g]$
Damping Coeff. (c_D)	1.05e-4	$[\frac{Ns}{m}]$

It is assumed that the crystal factory polarization is such that no domains are present in the $(-)$ variant. Therefore, since the mechanical stress applied on the PZT volume can only produce $(+) \leftrightarrow (90)$ phase transitions, the $(-)$ variant has been suppressed in the models.

The initial mesoscopic configuration of the PZT material is reported in Table 3.3, along with all the considered initial conditions.

Table 3.3: Initial Conditions of the Device

	Symbol	Value	Dim.
Mesoscopic Conf.	$x_+(0)$; $x_-(0)$	0.59; 0.0	$[-]$
Displacement	$\eta(0)$	3.3	$[nm]$
Velocity	$\dot{\eta}(0)$	0.0	$[m/s]$
Charge Density	$\sigma_e(0)$	0.135	$[C/m^2]$

The short-circuit natural frequency of the device (ω_n^{SC}) corresponding to the initial mesoscopic configuration can be approximately evaluated as follows:

$$\omega_n^{SC} = \sqrt{\frac{AY_{PZT}(0)}{ml_0}} \approx 103 \ [krad/s] \ . \tag{3.30}$$

Assuming the PFs as constants - which is the case of both the LTIM and the TIM - an approximated value of the resistive load allowing for the maximum power extraction in near-resonance conditions can be evaluated (through the *maximum power transfer* theorem in case of pure resistive load) as follows:

$$R_L^{Opt} = \frac{1}{\omega_n^{SC} C_{PZT}^{TIM}} = \frac{l_0}{\omega_n^{SC} A} r^{SF} \approx 65 \ [G\Omega] \ . \tag{3.31}$$

Figure 3.15 reports a comparison among the MsM and TIM (blue and red lines respectively) to a chirp input base acceleration of amplitude $g_{acc} = 9.81 \ m/s^2$.

Magnitude spectra of the displacement and the output voltage are provided in case of matched and unmatched resistive load. Simulation results confirm that the device resonance frequency (ω_r) depends on the resistive load (66). For the case of matched R_L (right-hand side of Fig. 3.15), the TIM reveals a 5% increase of ω_r with respect to ω_n^{SC}. Considering (3.29), this means that the electric term of the PZT reaction force:

$$F_{PZT}^{Elect} = Ah^{SF}\sigma_e \ , \tag{3.32}$$

results into a stiffening of the device.

The comparison between the TIM and the MsM always shows a further slight increase of the resonance frequency for the hysteretic system.

Moreover, plots relative to the matched R_L case show that, in some ranges of the input excitation frequency, the output voltage of the hysteretic system can exceed the one provided by the non-hysteretic one. The widening of the output voltage

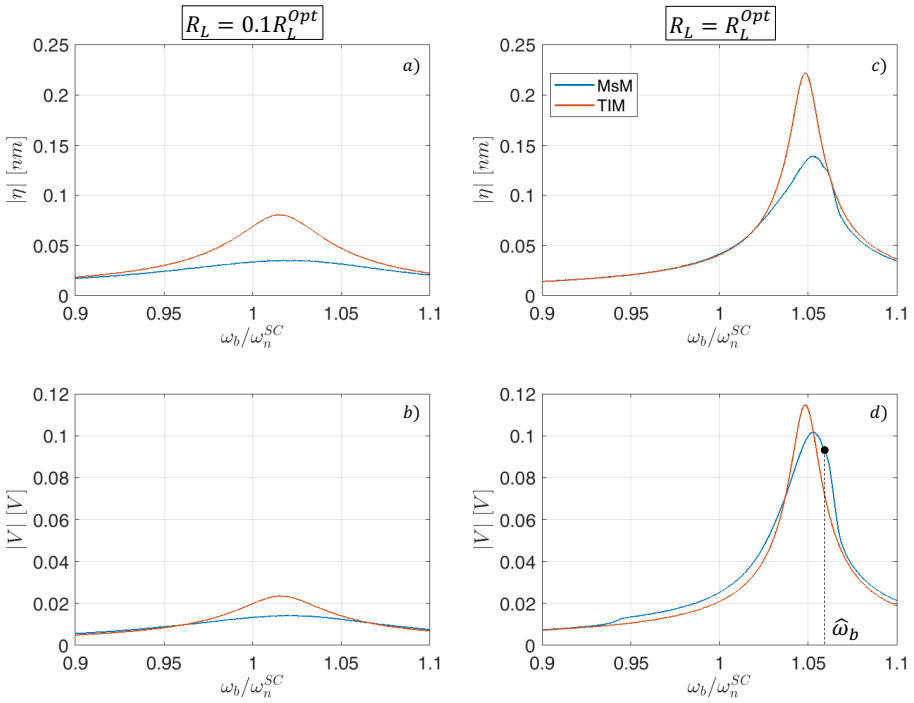

Figure 3.15: Simulation results for a chirp input base acceleration ($|\ddot{z}_b| = 1 g_{acc}$): a)-b) case with non-matched resistive load; c)-d) case with matched resistive load.

frequency bandwidth is a consequence of the domain switching process, which affects the material polarization and, therefore, the charge collected on the electrodes.

This is clearly shown in Figure 3.16, where the transient evolution of some quantities of interest is reported. In this case a harmonic input excitation of frequency 6% ω_n^{SC} (corresponding to $\widehat{\omega}_b$ in Fig. 3.15) and amplitude 1 g_{acc} has been applied to the device.

With respect to the hysteretic model (blue line), it can be seen how the mesoscopic configuration of the material (Fig. 3.16-a) rapidly evolves in a steady state condition characterized by periodic slight deviations from a condition where all domains are in the (+) variant. As a consequence, the average value of the charge density (Fig. 3.16-b) increases with respect to the TIM case (red line).

This results in an increased peak-to-peak value of the steady state output voltage of the hysteretic model, as can be observed in Fig. 3.17-c.

Figure 3.17 reports, for the same test case of Fig. 3.16, the evolution of some quantities of interest in a representative period (τ) of the system steady-state response. The relative percentage error between the TIM and the MsM predictions of the output voltage root-mean-square value is abut 16% (about 43% for the electric

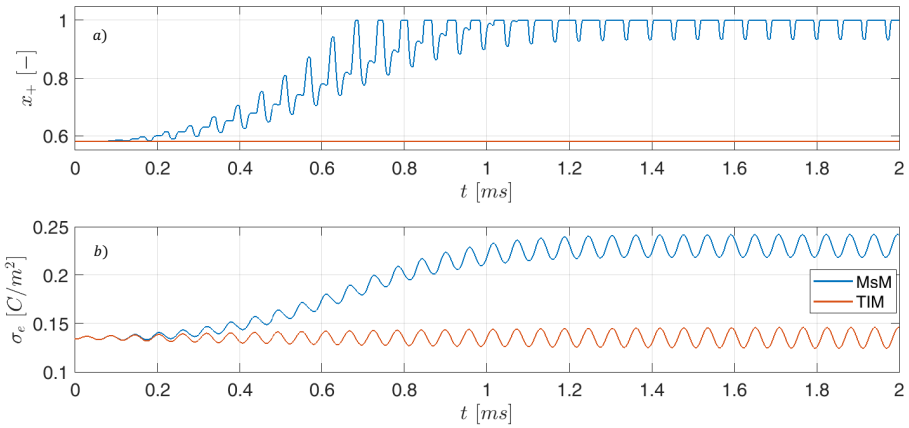

Figure 3.16: Evolution in time of: a) PF relative to the (+) variant; b) charge density on the electrode surface. Harmonic input excitation of amplitude $1g_{acc}$ and frequency $\widehat{\omega}_b \approx 6\%\ \omega_n^{SC}$ (see Fig. 3.15). Matched resistive load case.

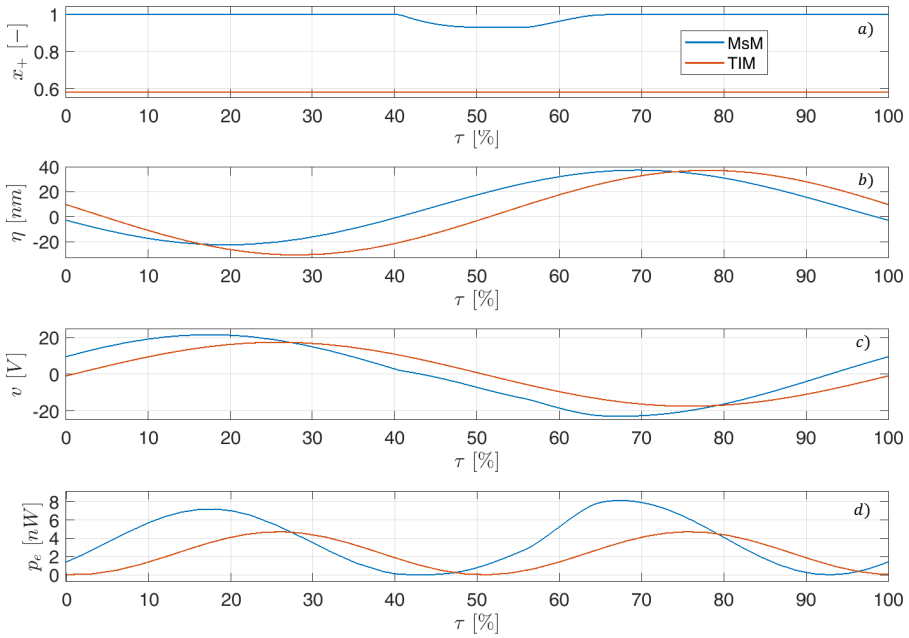

Figure 3.17: Evolution of some quantities of interest in a representative period of the system steady-state response: a) PF relative to the (+) variant; b) displacement of the device; c) output voltage; d) instantaneous electrical power. Harmonic input excitation of amplitude $1 \cdot g_{acc}$ and frequency $\widehat{\omega}_b \approx 6\%\ \omega_n^{SC}$ (see Fig. 3.15). Matched resistive load case.

power mean value). It can be seen how the domain switching process within the PZT material results in a slightly distorted waveform for the electrical quantities.

With the aim of further investigating the role of material nonlinearities in the dynamic response of the device, two more simulations have been carried out, as-

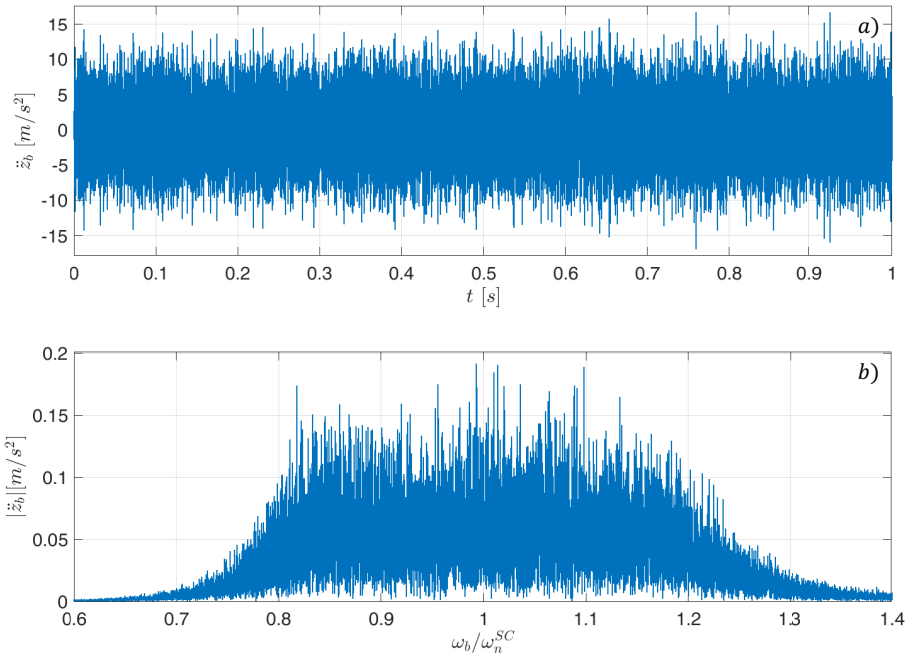

Figure 3.18: Random input acceleration ($\ddot{z}_b$): colored noise signal characterized by a null mean value and a standard deviation equal to 3.4 m/s^2. a) signal in time domain; b) signal magnitude in frequency domain.

suming a random acceleration signal as input for the system.

With reference to Fig. 3.18-a, the considered input excitation ($\ddot{z}_b$) is characterized by a null mean value and a standard deviation equal to 3.4 m/s^2. The relative frequency bandwidth, which has been chosen in a small range around the device resonance frequency, is depicted in Fig. 3.18-b.

Figures 3.19 and 3.20 reports, respectively, a comparison between displacements and output voltages predicted by TIM and MsM. For this analysis, the crystal corresponding to red hysteretic curves reported in Fig. 3.7 (hereafter referred to as $C1$) has been considered. It is characterized by a $\Delta g_0 = 20\ kPa$, while the remaining parametric set has been chosen as in Table 3.1. The initial conditions reported in Table 3.3 have been assumed for both the models.

With reference to Fig. 3.20-b, simulation results confirm the slightly wider frequency bandwidth of the MsM voltage response with respect to TIM (accordingly with Fig. 3.15-d). However, this does not result in a higher active power prediction of the MsM with respect to TIM. The Root Mean Square (RMS) value of the voltage signal relative to the hysteretic model, in fact, results about 8% lower than the TIM output.

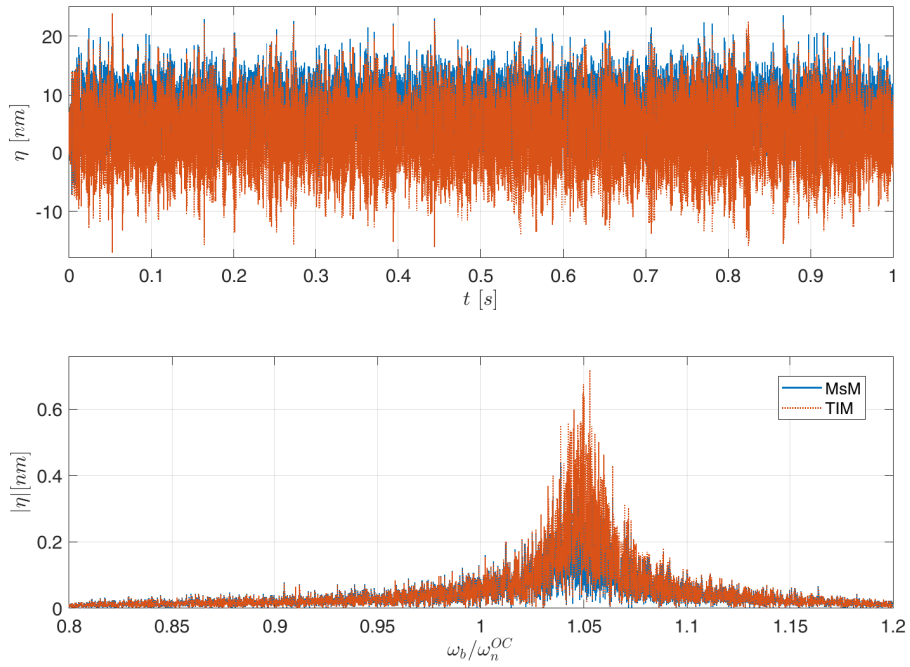

Figure 3.19: d_{33}-mode device: displacement (η) under a random input excitation. PZT crystal C1. a) signal in time domain; b) signal magnitude in frequency domain.

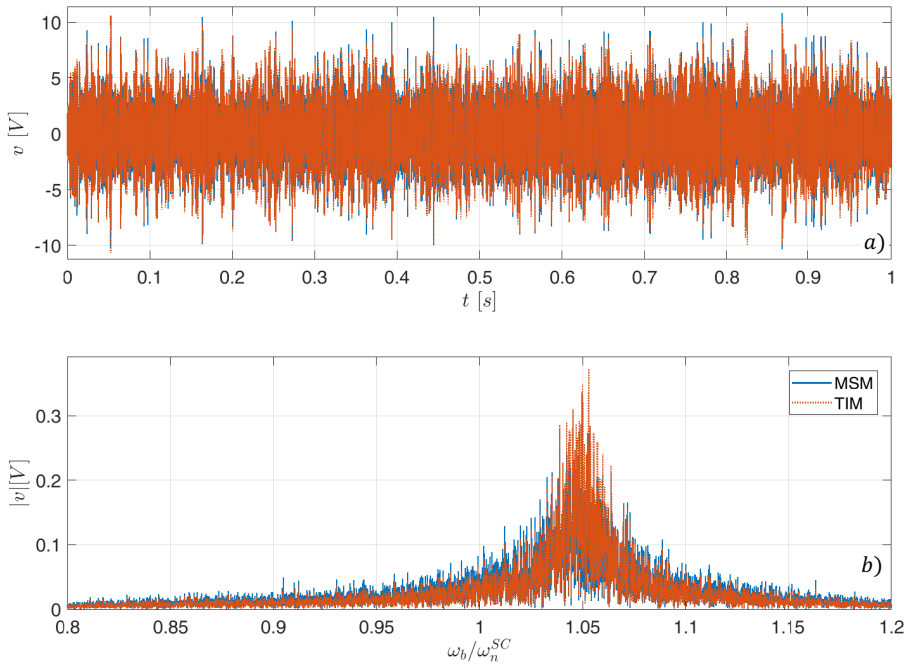

Figure 3.20: d_{33}-mode device:output voltage (v) under a random input excitation. PZT crystal C1. a) signal in time domain; b) signal magnitude in frequency domain.

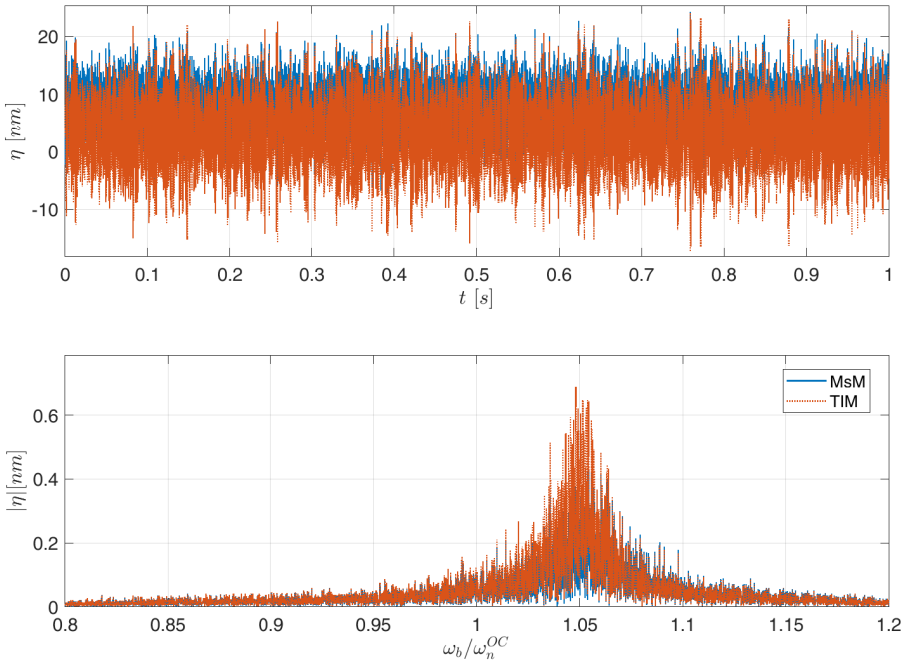

Figure 3.21: d_{33}-mode device: displacement (η) under a random input excitation. PZT crystal C2. a) signal in time domain; b) signal magnitude in frequency domain.

The diametrically opposite situation can be observed for a different PZT crystal. Figures 3.21 and 3.22 reports simulation results obtained assuming the device made of a crystal (hereafter referred to as $C2$) that, differently from $C1$, presents a four time larger value of the permittivity related to the (+) variant. The same random acceleration $\ddot{z}_b$ has been considered as input (Fig. 3.18).

By comparing Fig. 3.22-b and Fig. 3.20-b, it can be seen that the MsM response is now characterized by a significantly larger frequency bandwidth with respect to TIM. This results in a RMS of the hysteretic model output voltage that, in the considered case, is about 8% larger that the one provided by TIM. Simulations carried out assuming a random input acceleration provide an example of how, through an engineered crystal design (which is made possible by the physic based nature of the proposed model), material nonlinearities can be exploited in order to improve generation performances.

3.4.2 EH device working in d_{31} mode

The 1-D physics-based model, introduced in section 3.3.2, is now employed for modeling an harvester device working in the d_{31} mode. With reference to a single crystal domain (see Fig. 3.5), the basic assumption is that strains along the polarization

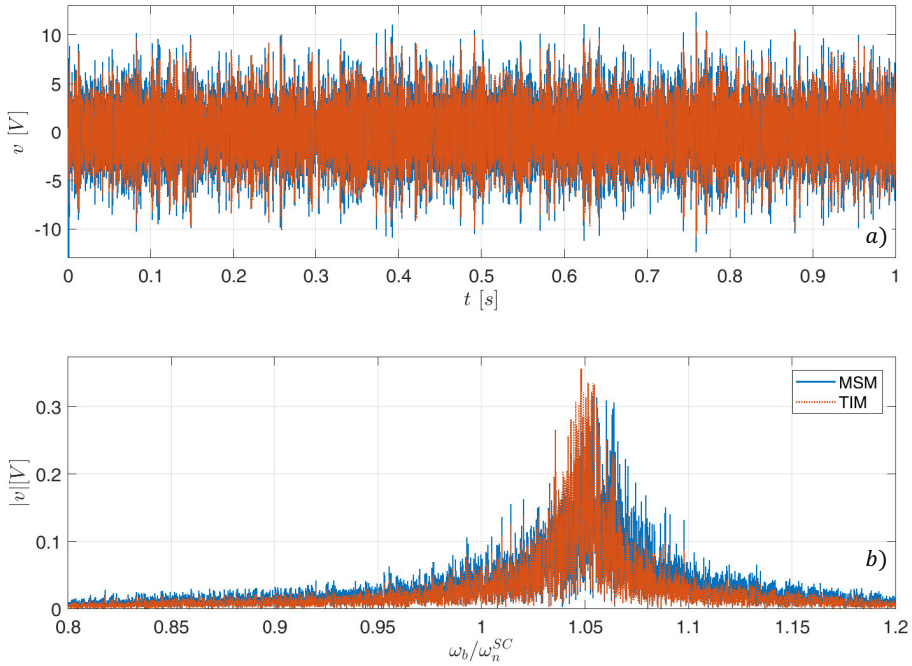

Figure 3.22: d_{33}-mode device: output voltage (v) under a random input excitation. PZT crystal C2. a) signal in time domain; b) signal magnitude in frequency domain.

axis (3-axis) can be related to strains along 1-axis, through the Poisson's coefficient.

A sketch of the device investigated in this section is shown in Fig. 3.23. It is a unimorph cantilever beam subjected to a direct excitation (i.e., with a base acceleration transverse to the axis of the cantilever) (67).

Thicknesses and Young's moduli of the PZT layer and the supporting substrate are in such a ratio that the neutral axis of the beam is located outside the PZT volume. As a consequence of that, an upward (positive) bending of the cantilever results in an overall axial compression of PZT domains, with a consequent average elongation of unit cells along the 3-axis ($\tilde{\epsilon}_3 > 0$). On the other hand, a downward (negative) tip deflection results in an overall axial elongation of domains, producing a compression of the unit cells along the transverse axis ($\tilde{\epsilon}_3 < 0$). Electric charge is collected on electrodes attached on the upper and the lower faces of the PZT layer, perpendicularly to the 3-axis. Electrodes extend all over the available surface. Moreover, a resistive load R_L is assumed to be connected to the electrodes.

The structure of the device consists of thin layers with different geometry and mechanical properties. All layers have the same length L and width W but different thicknesses t_i and Young's moduli $\tilde{Y}_i$.

The following assumptions are also taken into account: interfaces among layers

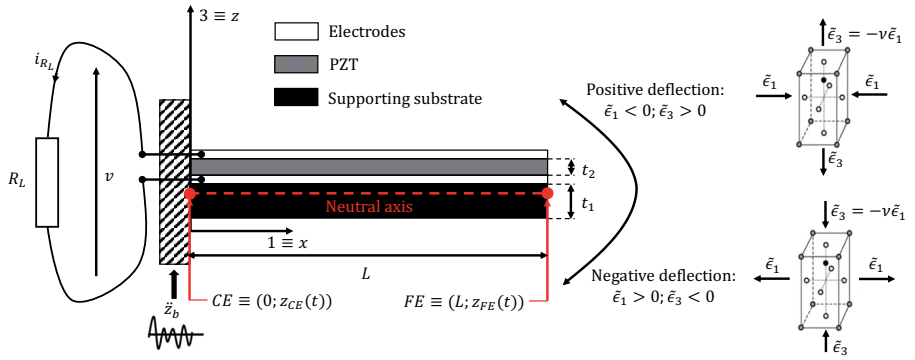

Figure 3.23: Sketch of the considered cantilever unimorph. Following quantities are related to the PZT material layer: average axial strain ($\tilde{\epsilon}_1$); average transverse strain ($\tilde{\epsilon}_3$); Poisson's coefficient (ν).

are smooth and continuous; layers do not slip with respect to each other. Moreover, the contribution of the electrodes to the system overall stiffness can be considered negligible. Therefore, from a mechanical point of view, the device will be modeled as a bi-layered cantilever (see Fig. 3.24) consisting in a linear isotropic elastic supporting substrate (thickness t_1, Young's modulus $\tilde{Y}_1 = const.$) and a top layer made of PZT crystal (thickness t_2, Young's modulus $\tilde{Y}_2$).

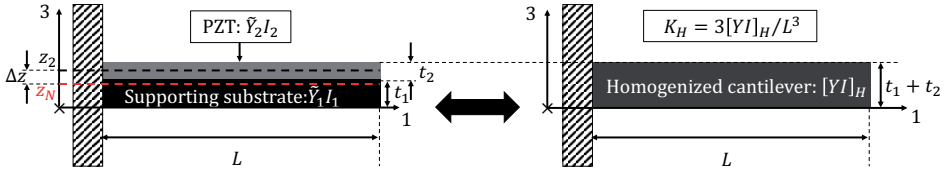

Figure 3.24: Bi-layered cantilever homogenization. Generic quantity $\tilde{Y}_i I_i$ represent the flexural rigidity of the i^{th} layer, while K_H is the stiffness of the homogenized cantilever.

Based on the model expressed by (3.8), it results that the PZT crystal Young's modulus is a nonlinear function of crystal phase fractions:

$$\tilde{Y}_2 = \frac{1}{d\left(x_+, x_-\right)} \ , \tag{3.33}$$

therefore, it is an implicit function of time t, strain $\tilde{\epsilon}_3$ and charge density σ_e, affecting the mechanical response of the cantilever.

As for the previous case, a simple SDOF model is employed to assess the time history of the unimorph tip displacement under the direct base excitation ($\ddot{z}_b$). The

SDOF model is expressed by the following ODE:

$$\ddot{z}_{tip} = -\ddot{z}_b - \frac{c_D}{m}\dot{z}_{tip} - \frac{K_H}{m} z_{tip} \ , \tag{3.34}$$

where: $z_{tip} = z_{FE} - z_{CE}$ (see Fig. 3.23) is the relative vertical displacement of the cantilever free end with respect to the clamped end; m is the cantilever equivalent mass; c_D is the viscous damping coefficient.

In (3.34), parameter K_H is the cantilever equivalent stiffness and can be evaluated as follows:

$$K_H = \frac{3[YI]_H}{L^3} \ , \tag{3.35}$$

where $[YI]_H$ is the *homogenized* flexural rigidity about the neutral axis.

According to (68), for an arbitrary n-layered cantilever, the following equation holds:

$$[YI]_H = \sum_{i=1}^{n} \left\{ A_i \tilde{Y}_i \left[(z_i - z_N)^2 + \frac{{t_i}^2}{12} \right] \right\} \ , \tag{3.36}$$

where $A_i = t_i W$ is the cross sectional area of the i^{th} layer and z_i is the symmetry axis coordinate, for the i^{th} layer, along direction 3 (see Fig. 3.24).

Neutral axis coordinate z_N can be evaluated using the following relation (68):

$$z_N = \sum_{i=1}^{n} \tilde{Y}_i t_i z_i \Big/ \sum_{i=1}^{n} \tilde{Y}_i t_i \ . \tag{3.37}$$

It is worth stressing that, given (3.33), (3.35)-(3.37), K_H is a nonlinear parameter depending on the PZT crystal electromechanical response.

In order to couple system (3.34) with the crystal model, a relation between the cantilever tip deflection (z_{tip}) and the crystal average transverse strain ($\tilde{\epsilon}_3$) must be provided. Under the assumption of small deflections, the average axial strain ($\tilde{\epsilon}_1$) in the PZT volume can be evaluated through the following expression:

$$\tilde{\epsilon}_1 = -\tilde{\kappa}(z_{tip})\Delta z \ , \tag{3.38}$$

where $\Delta z = z_2 - z_N$, is the distance of the piezoelectric film layer symmetry axis from the neutral axis (see Fig. 3.24) and $\tilde{\kappa}$ is the average beam curvature:

$$\tilde{\kappa} = \frac{1}{L} \int_0^L z''(x, z_{tip}) \, \mathrm{d}x \ . \tag{3.39}$$

In (3.39), $z^{''}$ is the second derivative in space domain of the beam neutral axis deflection.

According to the classical SDOF representation of a cantilever beam with mass per length λ, the equivalent mass has been computed as $m = 0.2235\lambda L$, while a quarter cosine wave form has been used for z:

$$z = \left[1 - cos\left(\frac{\pi x}{2L}\right)\right] z_{tip}(t) \ . \tag{3.40}$$

Finally, the PZT crystal average transverse strain ($\tilde{\epsilon}_3$) can be computed through the Poisson's ratio (ν):

$$\tilde{\epsilon}_3 = -\nu\tilde{\epsilon}_1(z_{tip}) \ . \tag{3.41}$$

Concerning the coupling of the PZT crystal model with the characteristic of an external resistive load (R_L) connected to the device electrodes, if $p_e(t) = vi_{R_L}$ is the instantaneous power absorbed by the load, the following expression holds:

$$q_e = -\int \dot{q}_{R_L}\,\mathrm{d}t = -\int \frac{v}{R_L}\,\mathrm{d}t = -\int \frac{E_3 t_2}{R_L}\,\mathrm{d}t \ , \tag{3.42}$$

where q_e is the free charge on the electrodes. Free charge density σ_e can be evaluated dividing q_e by the electrodes surface area $A = LW$.

Equations (3.41) and (3.42) allow for coupling the crystal mesoscopic evolution with the SDOF dynamics of the cantilever beam (3.34) and the electric load characteristic (3.42).

By substituting (3.11) in (3.42), taking into account (3.37)-(3.40) and definitions (3.26), the resulting nonlinear MsM can be written as follows:

$$\begin{cases} m\ddot{z}_{tip} + c_D\dot{z}_{tip} + K_H(x_+, x_-)z_{tip} = -m\ddot{z}_b = F_b \\ A\dot{\sigma}_e + \gamma(x_+, x_-)z_{tip} + \frac{t_2}{R_L}r^{SF}\sigma_e + \frac{t_2}{R_L}w^{SF} = 0 \\ \dot{x}_+ + x_+ p(z_{tip}, \sigma_e)_{[+,90]} - (1 - x_+ - x_-)p(z_{tip}, \sigma_e)_{[90,+]} = 0 \\ \dot{x}_- + x_- p(z_{tip}, \sigma_e)_{[-,90]} - (1 - x_+ - x_-)p(z_{tip}, \sigma_e)_{[90,-]} = 0 \end{cases} , \tag{3.43}$$

where it has been denoted by γ the following quantity: $\gamma = \frac{\nu\pi t_2 h^{SF}(x_+,x_-)\Delta z(x_+,x_-)}{2R_L L^2}$.

Figure 3.25 reports the lumped circuit representation of model (3.43). The electrical port is coupled with the mechanical one through a voltage-controlled generator that is a nonlinear function of crystal permittivity, coupling coefficient and Young's modulus. It is driven by the elastic reaction force:

$$F^{elast} = K_H(x_+, x_-)z_{tip} \ . \tag{3.44}$$

Differently from the case of the d_{33}-device mode (see Fig. 3.14), no controlled generators appear in the loop connected to the electrical port. Nevertheless, the dynamics of the left-handed side circuit loop in Fig. 3.25 is influenced by the electromechanical behavior of the crystal through the parameter K_H.

Figure 3.26 reports the block diagram representation of model (3.43), respectively.

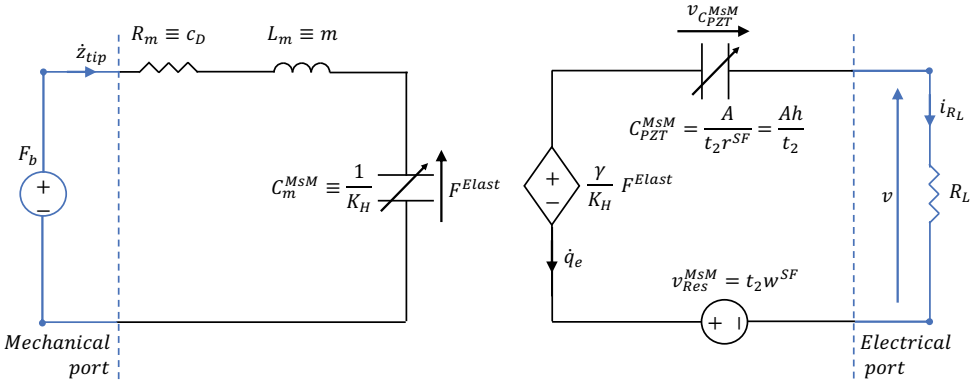

Figure 3.25: Lumped circuit representation of the PZT unimorph MsM.

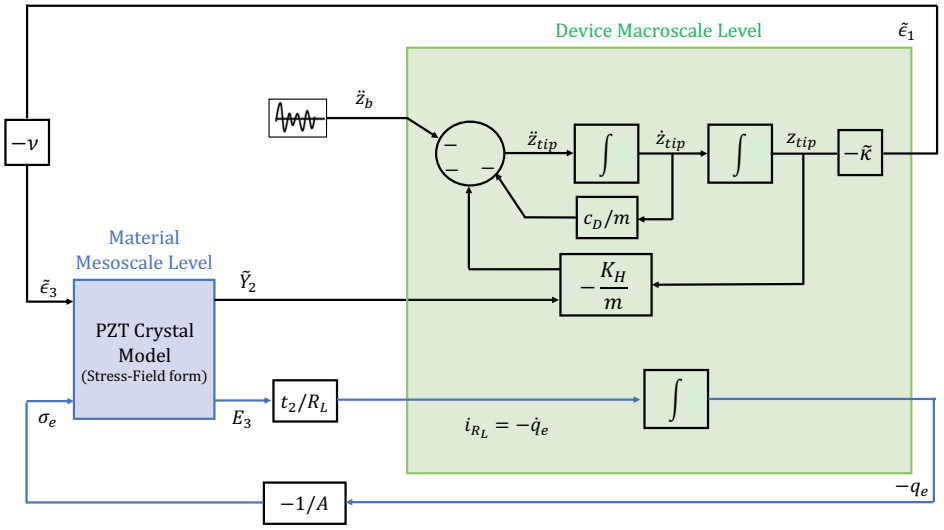

Figure 3.26: Implementation block diagram of the PZT unimorph MsM.

3.4.2.1 Simulation results

Numerical analyses have been performed exciting the device with a sinusoidal base acceleration, in *near-resonance* conditions ($f_{\ddot{z}_b} = 26\ Hz \approx f_n = \frac{1}{2\pi}\sqrt{\frac{K_H}{m}}$). Assuming that the factory polarization of the crystal such that all its domains are

in the (+) variant, the cantilever bending motion can only produce (+) $\leftrightarrow$ (90) domain transitions. Therefore, for the numerical analyses reported hereafter, the (−) variant has been suppressed in the MsM. In order to make a comparison, the same numerical analyses have been carried out by employing the TIM of the PZT crystal. As clarified in the previous section, TIM results from MsM by suppressing domain phase transitions. Crystal $C2$ has been considered as constituting the device. Parameters of the cantilever are summarized in Table 3.4.

Table 3.4: Parameters of the PZT Unimorph Device

Cantilever Geometrical Parameters	Value	Dim.
Length (L); Width (W)	83.2; $L/4$	$[mm]$
Substrate Thickness (t_1); PZT Thickness (t_2)	0.15; 0.15	$[mm]$

Substrate Material Parameters	Value	Dim.
Young's Modulus ($\tilde{Y}_1$)	190	$[GPa]$
Density (ρ_1)	8000	$\left[\frac{kg}{m^3}\right]$

PZT Crystal Parameters [1]	Value	Dim.
Δg_0	22.0	$[kPa]$
Poisson Coeff. (ν)	0.35	$[-]$

SDOF Model Parameters	Value	Dim.
Equivalent Mass (m)	0.92	$[g]$
Damping Coeff. (c_D) [2]	5e-3	$\left[\frac{Ns}{m}\right]$

Resistive Load.	Value	Dim.
R_L	10	$[k\Omega]$

Left-handed side of Fig. 3.27 shows, for increasing base acceleration amplitudes, the cantilever maximum tip deflection in percentage of the total device length (L). It can be seen that, for the highest amplitude of the input excitation ($\ddot{z}_b = 1.9\ g_{acc}$), the tip deflection does not exceed $0.25\ L$. This is in agreement with the modeling assumption of negligible geometric nonlinearities (small deflections) for the cantilever (69). Moreover, TIM and MsM predictions of the cantilever tip deflection coincide. This means that crystal nonlinearities, in the considered $\ddot{z}_b$ range, do not affect the mechanical behavior of the device in a significant way.

[1] Other crystal parameters are reported in Table 3.1.

[2] The value adopted for c_D corresponds to a damping ratio $\delta = b/(4\pi m f_n) \approx 1.7\%$, which is a common choice for systems like the one under investigation. An average value of the undamped natural frequency (f_n) can be deduced from Fig. 3.29-c.

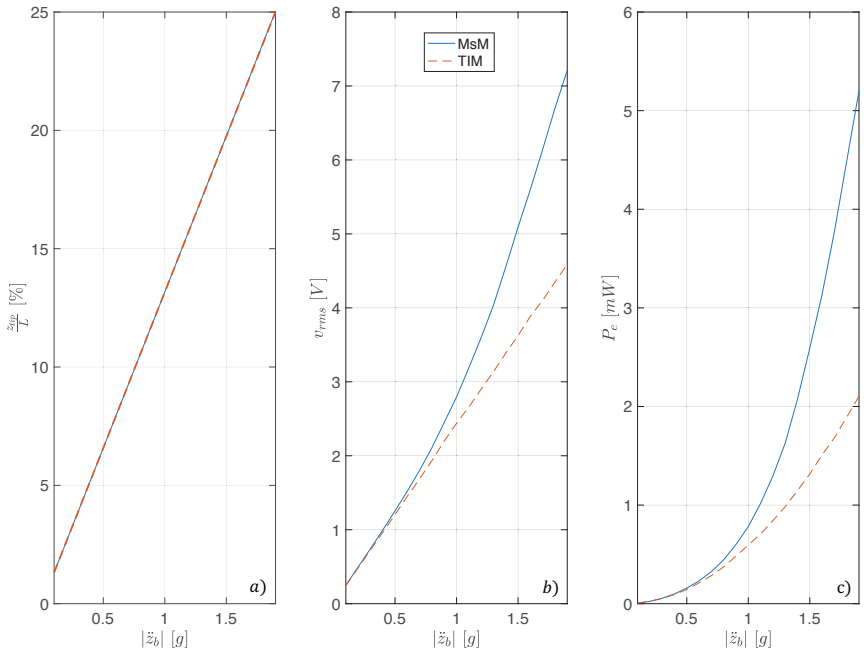

Figure 3.27: d_{31}-mode device: simulation results for different base acceleration amplitudes in near-resonance conditions ($g_{acc} = 9.81\ m/s^2$).

On the other hand, their influence on the device output voltage (v_{rms}) and, as a consequence, on the average electric power (P_e) absorbed by the resistive load (R_L) is more relevant. For excitation amplitudes larger than 0.6 g_{acc}, TIM starts to significantly underpredict v_{rms} values provided by MsM. The maximum relative percentage error, corresponding to 1.9 g_{acc}, is about 36% for the voltage and 59% for the electric power.

Fig. 3.28 shows the evolution of some quantities of interest in a representative period ($\tau = 1/f_{\ddot{z}_b}$) of the device steady-state response. The input excitation amplitude is equal to 1.9 g_{acc}. It can be seen how, differently from TIM, MsM predicts domain switching for tip deflection values outside the green highlighted zones (Fig. 3.28-b). The different maximum and minimum values reached by x_+ in the MsM case are responsible for the larger peak to peak output voltage (Fig. 3.28-c). It can be also seen how PTs produce slightly distorted voltage and power waveforms.

Fig. 3.29 reports, for the same case, the evolution in time domain of the PZT crystal Young's modulus $\tilde{Y}_2$ (Fig. 3.28-b). It can be seen how, for the MsM, $\tilde{Y}_2$ slightly deviates from the constant value predicted by the TIM, thus resulting in a negligible variation of the cantilever undamped natural frequency f_n (Fig. 3.28-c).

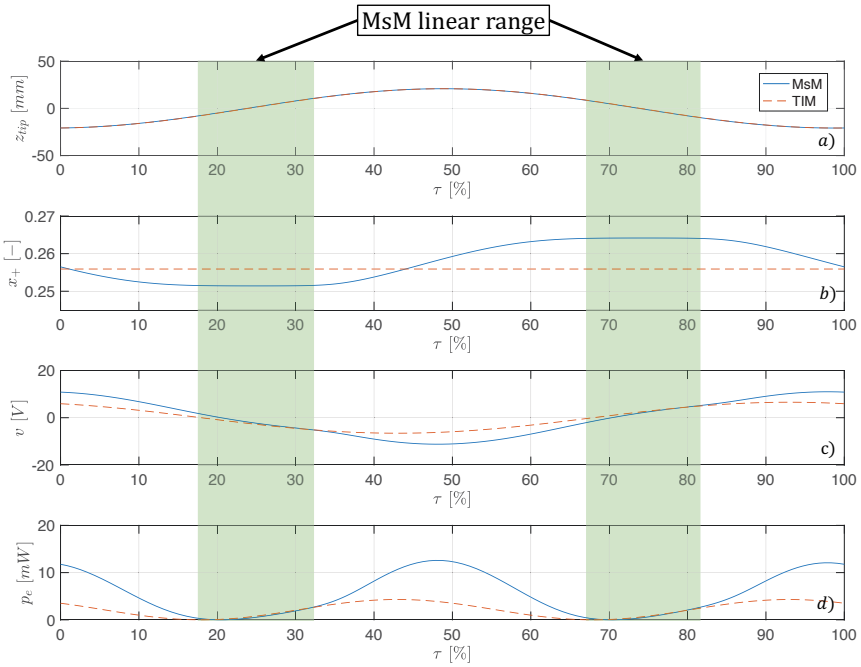

Figure 3.28: d_{31}-mode device (case $|\ddot{z}_b| = 1.9\ g_{acc}$): evolution of quantities of interest in a representative period of the device steady-state response. a) tip displacement; b) PF relative to the (+) variant; c) output voltage; d) instantaneous electric power.

The evolution in time of the crystal permittivity, which from (3.8) results equal to:

$$\varepsilon = \varepsilon_0 \varepsilon_r = a(x_+, x_-) \ , \tag{3.45}$$

is also reported (Fig. 3.28-c).

3.5 Conclusion

In this chapter, the effect of material nonlinearities on the response of piezoceramic energy harvesters has been investigated.

A physics-based, nonlinear formulation has been adopted for deriving constitutive equations of piezoceramic mono-crystalline material. The proposed model is able to reproduce domain switching dynamics, which determines the mesoscopic configuration of the material. Reported quasi-static numerical analyses have shown that hysteresis strongly depends on parameter Δg_0, which can be essentially related to the switching inertia of crystal domains. Moreover, proposed approach reproduces the rate-dependent hysteretic behavior.

Through a multi-scale approach, the mesoscopic dynamics of crystal domains has been coupled with the dynamics of two different type of devices, both modeled

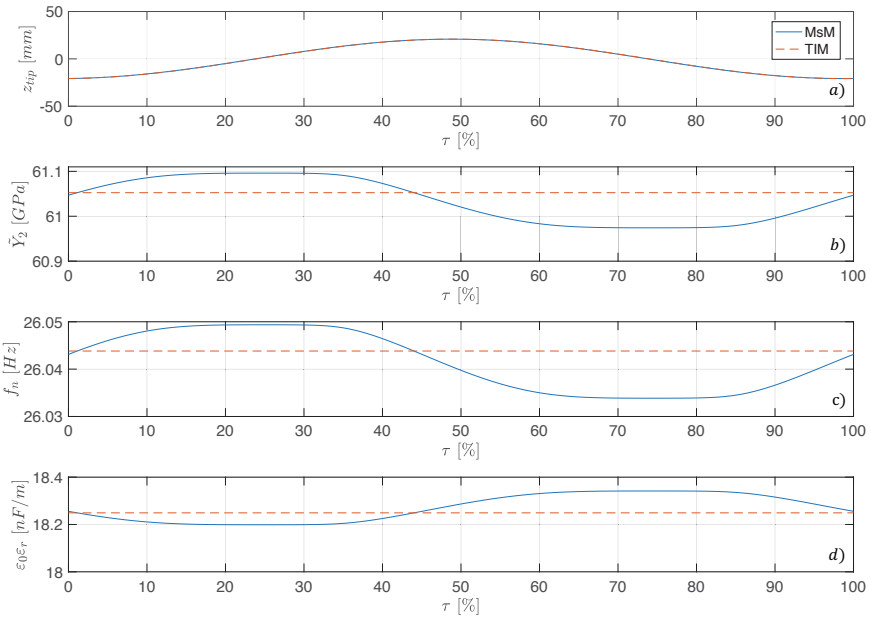

Figure 3.29: d_{31}-mode device (case $|\ddot{z}_b| = 1.9\ g_{acc}$): evolution of quantities of interest in a representative period of the device steady-state response. a) tip displacement; b) PZT crystal Young's modulus; c) device undamped natural frequency; d) crystal permittivity.

as SDOF systems. Implementation issues have been also discussed, in details.

Equivalent lumped circuit representations have been derived for the proposed models. In contrast with the classical linear circuit representation - widely adopted in literature for representing piezoelectric transducers - circuits reported in this chapter are enriched with nonlinear, time-varying components. This allows for both an effective visualization of the role that the material mesoscopic evolution has on the energy transduction process and an immediate comparison with the linear case.

Dynamic numerical analyses have been reported for two case studies: a nano-generator elementary cell (working in d_{33}-mode) and a piezoceramic unimorph (d_{31}-mode).

Results show that, even for low amplitudes of the input excitation, significant misprediction can result from ignoring material hysteresis. Moreover, the physics-based feature of the proposed modeling approach provides an insight on how, through an engineered crystal design, material nonlinearities can be potentially exploited in order to improve energy efficiencies.

4

A nonlinear circuit for modeling large deformation effects in piezoelectric system dynamics

4.1 Introduction

In the previous chapter, the behavior of devices based on piezoceramic materials has been investigated. Most of the piezoelectric energy harvesters studied to date consist of a bending member made of stiff ceramics (such as PZT) acting as a mechanical resonator. Even if designed to be tuned to the dominant frequency of the environment vibration, deformations of the beam must be typically small in order to avoid material failure under resonance conditions (69). This justifies the wide adoption of linear models in the past literature (70, 71, 72, 73, 74). The interest in nonlinear energy harvesting comes from the insight of exploiting nonlinear phenomena in order to overcome what is referred to as the main limitation of energy harvesting devices (75). As resonant electromechanical systems, in fact, their effectiveness is limited to a very narrow bandwidth around resonance frequencies. Recent literature reports various devices for energy harvesting applications with intentionally designed nonlinearities (76, 77, 78, 79). Moreover, several review papers (80, 81, 82) report examples of nonlinear and other methods of inproved broadband energy harvesting. Causes of nonlinear responses can be traced to several mechanisms, such as instability phenomena (83, 84, 85, 86), nonlinear material constitutive law (as discussed in the previous chapter), impacts (87, 88, 89, 90), etc.. Additionally, nonlinearities can arise from geometric effects (91, 92, 93). The advantage offered by piezoelectric polymers, such as PVDF (94), of sustaining large displacement without failure or

drastic reduction of the piezoelectric efficiency (95, 96, 97), provides the opportunity of exploiting geometric nonlinearities - which are significant when large deflections occur - as a way of improving the frequency bandwidth of this type of devices. In a modeling perspective, the electromechanical response of flexible piezoelectric devices can be assessed through different numerical and analytical techniques, e.g. reduced-order models, Finite Element (FE) models and circuit analogy methods (13, 98, 99, 100, 101, 102, 103, 104). While FE simulations can be a viable computational strategy for nonlinear static analyses, reduced-order models are more attractive for nonlinear dynamic analyses because they allow to save elaboration time. Aside few exceptions (99), however, most reduced-order models assumes a linear electromechanical response and the modal superposition principle is extensively adopted to derive the state-space representation of the system. The solution of nonlinear dynamic equilibrium equations using mode superposition techniques was first studied in (105) and implemented successfully in (106) for mechanical problems. A review of reduced order model techniques is reported in (107), including a description of the modal coordinate reduction. The use of modal derivatives for nonlinear model order reduction has been recently proposed in (108) in the context of isogeometric FE analysis. Few studies describe efficient numerical procedures for reduced order model techniques and coupled domains (such as in electromechanical systems). The most important contributions are provided in (109) and (110), the proposed strategy is implemented in (111).

In this chapter, an efficient hybrid approach is proposed for accurately modeling the nonlinear dynamic response of PVDF energy harvesters. The approach employs reduced-order nonlinear modeling techniques for estimating the Frequency Response Functions (FRFs) of the device. With the aim of accurately predict nonlinear geometric effects, lumped coefficients of the reduced-order model (related to nonlinear terms) are identified by fitting global curves providing the tip displacement of the device for increasing values of a static external load (i.e., the *pushover* curves). In order to obtain pushover curves, the FE method is employed to solve the equations governing the device response under static loading. The global FE-based solutions are used in place of experimental data to identify the values of linear and nonlinear lumped coefficients of the reduced-order model.

4.2 Nonlinear circuit reduced-order model

Forced vibrations of a cantilever-type generator, in the linear elastic case, can be defined through modal coordinates η_r (102, 112):

$$\begin{cases} \ddot{\eta}_r + 2\zeta_r\omega_r\dot{\eta}_r + \omega_r^2\eta_r - \theta_r\upsilon = f_r \ , \\ C_p^{\text{eq}}\dot{\upsilon} + \frac{\upsilon}{R_L} + \sum_{r=1}^{\infty}\tau_r\dot{\eta}_r = 0 \end{cases} \ , \tag{4.1}$$

for each mode r.

In (4.1), ζ_r is the modal mechanical damping ratio, ω_r is the undamped natural frequency, θ_r and τ_r are modal electromechanical coupling terms, f_r is the modal mechanical forcing function, C_p^{eq} is the capacitance, R_L is the load resistance and υ is the voltage response across the external resistive load.

Provided modal coordinates $\eta_r(t)$, the transverse displacement of the neutral axis $u(\xi,t)$ relative to the moving base at position $\xi = x/L$ and time t, is equal to:

$$u(\xi,t) = \sum_{r=1}^{\infty}\phi_r(\xi)\eta_r(t) \tag{4.2}$$

where $\phi_r(\xi)$ is a mass normalized eigenfunction (*mode shape*). Using Hamilton's principle and Galerkin method, Stanton et al. (113) extended the formulation in (102) to the case of nonlinear piezoelectricity:

$$\begin{cases} \ddot{\eta}_r + 2\zeta_r\omega_r\dot{\eta}_r + \omega_r^2\eta_r + \sum_{j,k,l}^{N}\alpha_{rjkl}\eta_j\eta_k\eta_l - \left(\theta_r + \sum_{j,k=1}^{N}\theta'_{rjk}\eta_j\eta_k\right)\upsilon = \Gamma_r\ddot{z}_b \ , \\ C_q^{eq}\dot{\upsilon} + \frac{1}{R_L}\upsilon + \left(\tau_r + \sum_{j,k=1}^{N}\tau'_{rjk}\eta_j\eta_k\right)\dot{\eta}_r = 0 \ , \end{cases} \tag{4.3}$$

where α_{rjkl}, θ_r, θ'_{rjk}, τ_r and τ'_{rjk} are coefficients that can be determined based on the orthogonal basis functions used to represent in the modal space the transverse deflection of the device. Coefficient Γ_r is the modal mechanical forcing function coefficient that multiplies the base acceleration $\ddot{z}_b$.

In (4.3) it can be seen that elastic nonlinearities results from cubic terms and the nonlinear coupling is third order as well.

Following (113) and assuming a linear damping, the single-mode approximation of (4.3) can be written as follows:

$$\begin{cases} \ddot{\eta} + 2\zeta\omega\dot{\eta} + \omega^2\eta + \alpha\eta^3 - \left(\theta + \theta'\eta^2\right)\upsilon = \mathcal{T}_n\ddot{z}_b \\ C_p^{\text{eq}}\dot{\upsilon} + \dfrac{\upsilon}{R_L} + \left(\tau + \tau'\eta^2\right)\dot{\eta} = 0 \end{cases} \ . \tag{4.4}$$

Figure 4.1 reports the lumped circuit representation of model (4.4), where the independent voltage source connected to the mechanical port is defined by $F_b = m\mathcal{T}_n \ddot{z}_b$, the constant inductance L_m represents the system equivalent mass m (accounting for the kinetic energy stored by the system), and the constant resistor $R_m \equiv c_D = 2m\zeta\omega$ represents dissipative effects related to viscous damping.

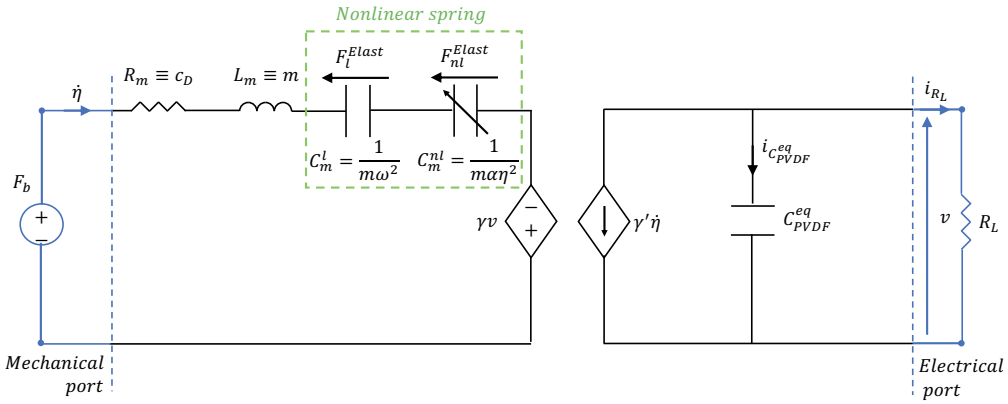

Figure 4.1: PVDF unimorph generator: lumped circuit representation of the relative reduced-order model.

The coupling between the mechanical and the electrical port is taken into account through controlled generators. The controlled voltage generator connected to the mechanical port, which is driven by the device outpu voltage v, is characterized by a gain γ depending on the device tip displacement square:

$$\gamma = m(\theta + \theta'\eta^2) \ . \tag{4.5}$$

The controlled current generator connected to the electrical port, driven by the device tip displacement rate of change $\dot{\eta}$, is characterized by a nonlinear gain $\gamma^{'}$:

$$\gamma^{'} = (\tau + \tau'\eta^2) \ . \tag{4.6}$$

The circuital component accounting for the electrostatic energy stored by the system is characterized by a constant capacitance C_p^{eq}, whereas the elastic energy stored by the system is taken into account through the series of a linear capacitor $C_m^l = 1/m\omega^2$ and a nonlinear capacitor $C_m^{nl} = 1/(m\alpha\eta^2)$. Voltage across the overall series capacitance represents the reaction force of a nonlinear Duffing's spring:

$$F^{Elast} = F_l^{Elast} + F_{nl}^{Elast} = \left(\kappa_D + \alpha_D\eta^2\right)\eta \ , \tag{4.7}$$

where $\kappa_D = m\omega^2$, and $\alpha_D = m\alpha$.

In order to accurately modeling the nonlinear dynamic response of the system under investigation, equation set (4.4) must be provided with proper values of the following parameters: κ_D, α_D, $\theta_D = m\theta$, $\theta_D^{'} = m\theta^{'}$, τ, and $\tau^{'}$. According to the approach proposed in (114), they can be estimated by fitting analytical approximations of push-over curves determined through quasi-static FE analyses. In the following subsections, a short review on nonlinear elasticity is reported, along with a description of the FE discretization.

4.3 Methods

4.3.1 Nonlinear elasticity theory

For the sake of completeness, we briefly review hereafter the equations for the continuum mechanical description of a piezoelectric solid under large strains. The interested reader can refer to (115) for a more complete discussion. The reference and deformed configurations are denoted by $\mathcal{B}$ and $\mathcal{S}$, respectively, where $\mathcal{B}, \mathcal{S} \subset \mathbb{R}^3$. When the electromechanical body deforms, the nonlinear mapping function $\varphi : \mathcal{B} \rightarrow \mathcal{S}$ at time instant t maps the material point $\mathbf{X} \in \mathcal{B}$ onto $\mathbf{x} \in \mathcal{S}$: $\mathbf{x} = \varphi(\mathbf{X}, t)$. The displacement vector $\mathbf{u}$ is obtained as the difference between the positions vectors of the current and initial configuration: $\mathbf{u}(\mathbf{X}, t) = \varphi(\mathbf{X}, t) - \mathbf{X}$, whereas the deformation gradient $\mathbf{F}$ can be defined as function of the displacement gradient $\mathbf{H}$: $\mathbf{F} = 1 + \mathbf{H}$, where: $\mathbf{H} = \operatorname{grad} \mathbf{u}$. According to the Faraday's law in quasi-static conditions: $\operatorname{curl} \vec{\mathbf{e}} = 0$, where $\vec{\mathbf{e}}$ is the electric field vector in the current configuration. Consequently, $\vec{\mathbf{e}}$ is the gradient of a scalar electric potential ϕ: $\vec{\mathbf{e}} = -\frac{\partial \phi}{\partial \mathbf{x}}$. In the current configuration, the balance of momentum and the Gauss's law state that:

$$\operatorname{div} \boldsymbol{\sigma} + \rho_{m,v} \bar{\mathbf{b}}_v = \rho_{m,v} \mathbf{A}, \quad \operatorname{div} \vec{\mathbf{d}} = \varrho_{e,v}, \tag{4.8}$$

where $\boldsymbol{\sigma}$ represents the mechanical Cauchy stress tensor, $\vec{\mathbf{d}}$ denotes the electric displacement, $\rho_{m,v}$ is the mechanical density, $\varrho_{e,v}$ is free electric charge density and $\rho_{m,v} \bar{\mathbf{b}}_v$ indicates the volume force (in the current configuration). In the initial configuration, the local balance of momentum given by Eq. (4.8) can be recast with respect to different stress and strain measures:

$$\operatorname{div} \mathbf{P} + \rho_{m,V} \bar{\mathbf{b}}_V = \rho_{m,V} \mathbf{A}, \quad \operatorname{div} \mathbf{FS} + \rho_{m,V} \bar{\mathbf{b}}_V = \rho_{m,V} \mathbf{A}, \tag{4.9}$$

where $\mathbf{P}$ and $\mathbf{S}$ are the total first and second Piola-Kirchoff stress tensors, respectively. Moreover, $\rho_{m,V} \bar{\mathbf{b}}_V$ represents the body force in the initial configuration.

Furthermore, it is assumed that a strain energy density function ψ exists for the electromechanical body that, in general, can be defined with respect to different kinematics tensors, namely $\mathbf{F}, \mathbf{E}, \mathbf{C}$ and the electric field vector $\vec{\mathbf{E}}$. All the quantities refer to the initial configuration. Here, $\mathbf{E}$ indicates the Green-Lagrange strain tensor that is obtained as: $\mathbf{E} = \frac{1}{2}\left(\mathbf{F}\mathbf{F}^T - \mathbf{I}\right) = \frac{\mathbf{C}-\mathbf{I}}{2}$, where $\mathbf{C} = \mathbf{F}^T\mathbf{F}$ is the right Cauchy-Green tensor. A compressible Neo-Hookean type material model with a total energy density $\psi\left(\mathbf{C}, \vec{\mathbf{E}}\right)$ is used in this work to model the piezoelectric layer:

$$\psi\left(\mathbf{C}, \vec{\mathbf{E}}\right) = \mu\left\{\frac{1}{2}\left[\mathcal{I}_1 - 3\right] - \ln\left(J_F\right)\right\} + \frac{\lambda}{2}\ln\left(J_F\right)^2 + \mathcal{C}_1\mathcal{I}_4 + \mathcal{C}_2\mathcal{I}_5, \tag{4.10}$$

where λ and μ are the Lame constants, $\mathcal{C}_1$ and $\mathcal{C}_2$ are further material constants to be calibrated and $\mathcal{I}_1, \mathcal{I}_4, \mathcal{I}_5$ are computed for a transversely isotropic material according to (116, 117). Given ψ it is obtained respectively that $\mathbf{S} = \frac{\partial \psi}{\partial \mathbf{E}}$ and $\overrightarrow{\mathbf{D}} = -\frac{\partial \psi}{\partial \overrightarrow{\mathbf{E}}}$, where $\overrightarrow{\mathbf{D}}$ is the dielectric displacement vector in the initial configuration. Further transformations from the material to the current configuration is possible by means of the following relationships:

$$\overrightarrow{\mathbf{e}} = \mathbf{F}^{-T}\overrightarrow{\mathbf{E}}, \qquad \overrightarrow{\mathbf{d}} = \frac{\mathbf{F}\overrightarrow{\mathbf{D}}}{J_F}, \qquad \boldsymbol{\sigma} = \frac{\mathbf{F}\mathbf{S}\mathbf{F}^T}{J_F}. \tag{4.11}$$

Classical Dirichlet and Neumann boundary conditions for the mechanical and electrical fields are considered (see Chapter 2). Finally, it is remarked as for the non piezoelectric layer, a compressible Neo-Hookean type material model is employed where the total energy density is $\psi\left(\mathbf{F}\right)$:

$$\psi(\mathbf{F}) = \frac{1}{2}\lambda\left(J_F - 1\right)^2 + \mu\left(\frac{1}{2}\left(\mathrm{Tr}\left[\mathbf{C}\right] - 3\right) - \ln(J_F)\right). \tag{4.12}$$

4.3.2 Finite element discretization for static problems

The standard nodal FE discretization is employed following (117, 118). In doing so, the advanced symbolic computational tools for FE analysis available in the AceGen/AceFEM are useful to facilitate the full automation of the linearization process. Therefore, let $\mathbf{u} = \sum N_i\hat{\mathbf{u}}_i$ and $\phi = \sum N_i\hat{\phi}_i$ be the discretized displacement and electric potential fields, respectively, where $\hat{\mathbf{u}}_i$ are the nodal displacements and $\hat{\phi}_i$ the nodal electric potentials (N_i are the shape functions). According to (118), since all quantities in Eq. (4.10) and Eq. (4.12) depend on the displacement field and the electric potential, the resulting set of nonlinear equations has the general form $\mathbf{R}(\mathbf{p}) = \mathbf{0}$, where the unknown variables $\mathbf{p} \in \Re^{n_{tp}}$ have to be determined (n_{tp} is the total number of global unknowns of the problem). If $\mathbf{p}_e \subset \mathbf{p}$ is a subset of the

global vector of unknowns $\mathbf{p}$ from which the eth element depends explicitly, then the element $\mathbf{R}_e$ and the Gauss point $\mathbf{R}_g$ contributions to the global residuals $\mathbf{R}$ are explicit functions of $\mathbf{p}_e$, i.e. $\mathbf{R}_e(\mathbf{p}_e)$ and $\mathbf{R}_g(\mathbf{p}_e)$. In particular, at the element level, the internal residuals $\mathbf{R}_e$ are obtained using AceGen as follows (118):

$$\mathbf{R}_e = \frac{\partial}{\partial \mathbf{p}_e}\left(\int_V \psi(\mathbf{p}_e) dV\right) = \mathbf{0}, \tag{4.13}$$

where $\mathbf{p}_e$ is the unknown vector related to the element that collects all nodal displacements $\hat{\mathbf{u}}_i$ and/or nodal electrical potentials $\hat{\phi}_i$. Within the FE procedure, the global residuals $\mathbf{R}$ are approximated as:

$$\mathbf{R} \approx \bigwedge_{e=1}^{n_e} \mathbf{R}_e = \bigwedge_{e=1}^{n_e} \sum_{g=1}^{n_g} w_g J_g \mathbf{R}_g = \mathbf{0}, \tag{4.14}$$

where $\bigwedge$ is the standard FE assembly operator, n_e indicates the number of elements, n_g is the number of Gauss points and g indicates a generic Gauss point (w_g and J_g are the Gauss point weight and Jacobian determinant, respectively). The Gauss point contribution to the residuals is $\mathbf{R}_g = \frac{\hat{\delta}\psi(\mathbf{p}_e)}{\hat{\delta}\mathbf{p}_e}$. Finally, within the FE procedure, the tangent operator $\mathbf{K} \approx \bigwedge_{e=1}^{n_e} \mathbf{K}_e = \bigwedge_{e=1}^{n_e} \sum_{g=1}^{n_g} w_g \mathbf{K}_g$ is formed from the Gauss point tangent operator $\mathbf{K}_g$:

$$\mathbf{K}_g = \left(\frac{\hat{\delta}\mathbf{R}_g}{\hat{\delta}\mathbf{p}_e}\right). \tag{4.15}$$

4.4 Hybrid computational strategy

A hybrid computational approach is here employed for modeling the dynamical behavior of EH devices. (see Fig. 4.2). It is based on two steps. First, Eq. (4.14) is solved discretizing the physical domain of the piezoelectric cantilever. In particular, a pattern of forces (F_z) is statically applied to the structural model (including nonlinear effects) and the z-component of the total reaction at the base (R_z) is plotted as a function of the tip displacement (η). This provides the capacity curve of the device (usually referred to as pushover curve). Through the second step of the proposed procedure, pushover curves allows for reducing the nonlinear static problem to an equivalent SDOF system. Hence, a lumped nonlinear spring element, representing the elastic reaction force ($F^{Elast} = R_z$) in the reduced-order model (see Fig. 4.1), is calibrated based on the estimated capacity curve. This result is used to solve the equation set (4.4), which represents the ordinary differential equations

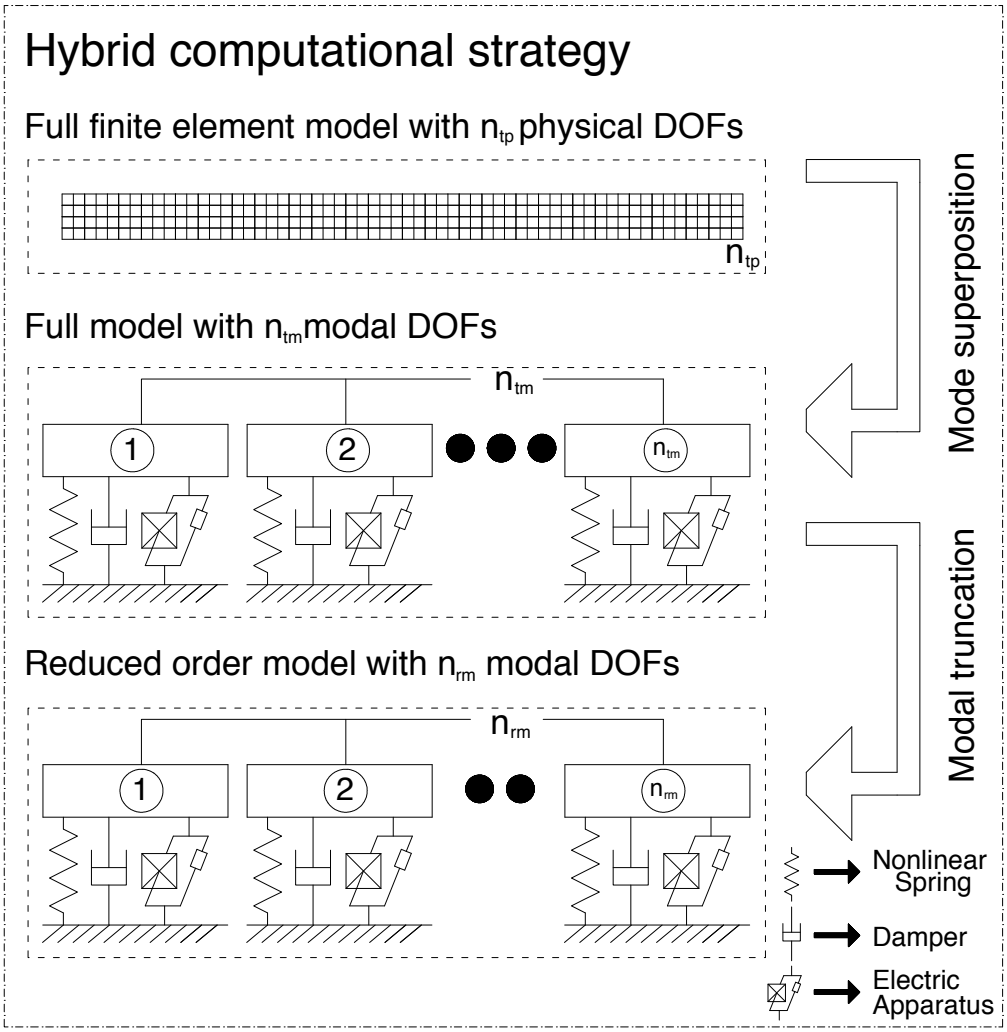

Figure 4.2: Nonlinear PVDF unimorph generator: implemented hybrid computational strategy.

describing the full dynamics of the piezoelectric energy harvester. In this way, the nonlinear state-space model equation is integrated using a time discretization algorithm. The overall numerical strategy has been implemented in Mathematica (using the advanced symbolic computational tools available in AceGen/AceFEM (118)) and Matlab.

Analytical expressions can be also derived for the case of harmonic input base vibrations. With reference to system (4.4), let assume a sinusoidal input acceleration with amplitude F_b, frequency ω_F and phase ϕ_F. Based on experimental evidence (69, 114), the electrical contribution to the mechanical equation can be considered negligible. Therefore, for the single-mode approximation, (4.4) reduces to:

$$\begin{cases} \ddot{\eta}(t) = -2\zeta\omega\dot{\eta}(t) - \omega^2\eta(t) - \alpha\eta(t)^3 + F_b\cos(\omega_F t + \phi_F) \\ C_p^{\mathrm{eq}}\dot{\upsilon} + \dfrac{\upsilon}{R_L} + \theta\dot{\eta} = 0 \end{cases} . \tag{4.16}$$

The solution of the first equation is well established (119) and allows for correlating the amplitude of the tip oscillation A_{tip} with the amplitude of the external acceleration F_b as function of ω and ω_F:

$$\left\{ \left[\left(\omega^2 - \omega_F^2\right) A_{tip} + \frac{3}{4}\alpha A_{tip}^3 \right]^2 + \left[2\zeta\omega_F A_{tip}\right]^2 \right\}^{1/2} = F_b. \tag{4.17}$$

According to (119), provided that the following inequality is verified:

$$\frac{\alpha {A_{tip}}^2}{36{\omega_F}^2} \ll 1, \tag{4.18}$$

the tip oscillation can be well approximated by a harmonic signal in the form $\eta(t) \approx A_{tip}cos(\omega_F t)$. It is worth stressing that $A_{tip}(\omega_F)$ is a nonlinear function of the input excitation frequency ω_F. Therefore, the second equation can be recast in the form:

$$\dot{\upsilon} + \frac{1}{R_L C_p^{\mathrm{eq}}}\upsilon = -\frac{\theta A_{tip}}{C_p^{\mathrm{eq}}}\frac{d}{dt}\left[\cos\left(\omega_F t\right)\right]. \tag{4.19}$$

The steady-state solution of Eq. (4.19) is given by:

$$\upsilon(t) = \mathrm{Re}\{\bar{V}e^{\iota\omega_F t}\} = |\bar{V}|cos(\omega_F t + \angle\bar{V}) \tag{4.20}$$

where $\bar{V}$ is a complex quantity expressed as follows:

$$\bar{V} = -\frac{\omega_F\theta A_{tip}}{C_p^{\mathrm{eq}}\left[{\omega_F}^2 + \frac{1}{(R_L C_p^{\mathrm{eq}})^2}\right]}\left(\omega_F + \iota\frac{1}{R_L C_p^{\mathrm{eq}}}\right). \tag{4.21}$$

Therefore, the steady-state amplitude A_v of the output voltage can be computed as:

$$A_v(\omega_F) = |\bar{V}| = \frac{\omega_F\theta A_{tip}(\omega_F)}{C_p^{\mathrm{eq}}\sqrt{\omega_F^2 + \frac{1}{(R_L C_p^{\mathrm{eq}})^2}}}. \tag{4.22}$$

Table 4.1: Material and geometrical data used in the numerical study

Property	Symbol	Value
Elastic modulus of the piezoelectric film	Y_{PVDF}	3.0 GPa
Elastic modulus of the substrate	Y_{mylar}	3.79 GPa
Poisson ratio of the piezoelectric film	ν_{PVDF}	0.3
Poisson ratio of the substrate	ν_{mylar}	0.35
Damping ratio	ζ	4.0 %
Density of the piezoelectric film	ρ_{PVDF}	1780 kg/m^3
Density of the substrate	ρ_{mylar}	1390 kg/m^3
Lumped tip mass	M_{lump}	0.032 g
Piezoelectric coupling coefficient	d_{31}	23·10^{-12} pC/N
Electrical permittivity	ε_{33}	106e^{-12} F/m
Unimorph length	L	31.7 mm
Unimorph PVDF width	W	16.0 mm
Unimorph Mylar width - R	W	16.0 mm
Unimorph Mylar width - T	W_1	1.0 mm
Circuit resistance	R_L	10 MΩ
Thickness of the piezoelectric film	T_{PVDF}	28 μm
Homogenized stiffness	YI	37.7 Nmm^2
Equivalent mylar layer thickness	T^{eq}_{mylar}	172 μm

4.5 Case studies

The capabilities of the proposed hybrid approach are now assessed based on two device configurations. The first corresponds to the EH characterized experimentally by Elvin et al. in (69, 120), the second is inspired by the work of Kwon (121), where T-shaped piezoelectric cantilevers are employed for fluid energy harvesting applications. The considered configurations are depicted in Fig. 4.3, along with details of the relative cross sectional views. Both structures consist of a PVDF film with electrodes applied on the upper and bottom faces. Electrodes are provided with wires in order to connect electrical loads. Moreover, coatings are applied to protect the device from damage. Densities and Young's moduli of PVDF and mylar are provided in Table 4.1, along with the other main material and geometrical data adopted in this numerical study.

The thickness of the PVDF layer is 28 μm and the piezoelectric strain constant is $d_{31} = 23 \cdot 10^{-12}$ pC/N. According to Fig. 4.3, five layers are considered in the real configuration of both the devices, namely: a) an acrylic protection layer with

thickness equal to 6 μm, b) a silver layer with thickness equal to 8 μm, c) a central layer of PVDF with thickness equal to 28 μm, d) another silver layer with thickness equal to 8 μm, and e) a final layer of mylar, with thickness equal to 140 μm and widths equal to 10 mm for the rectangular cross section and 1 mm for the T-Shape section. It is observed as for the T-shaped energy harvester, the piezoelectric layer (made of PVDF) corresponds to the flange whereas the web is assumed made of mylar.

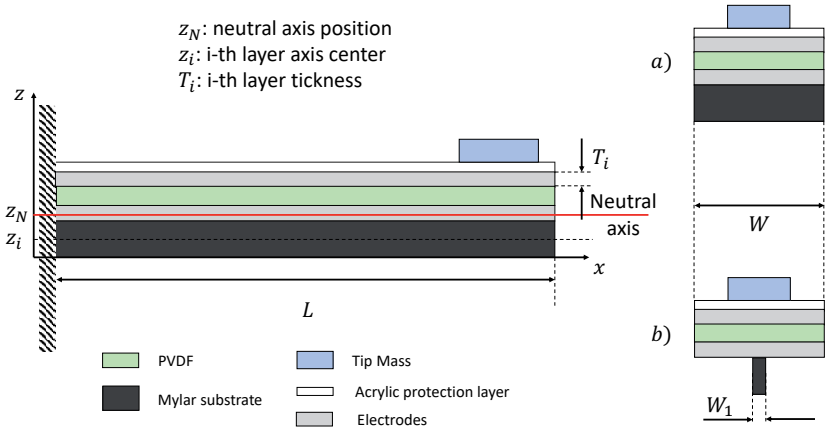

Figure 4.3: Sketch of the PVDF-based unimorph generators considered as case studies. a) rectangular cross section; b) T-shaped cross section.

FE analyses are first performed in order to derive the pushover curves of the two devices, with the assumption of open-circuit conditions for the electrical boundary. Then, a phenomenological law is derived for the nonlinear stiffness, based on the capacity curves. This involves the calibration of the spring-type elements of the reduced-order model (corresponding to the reciprocal of the series capacitance in the green box of Fig. 4.1). In practice, the capacity curve is approximated by means of the following relationship:

$$F^{Elast} = \kappa_D \eta + \alpha_D \eta^3 \ , \tag{4.23}$$

where κ_D and α_D characterize the constitutive law of the nonlinear spring.

4.6 Results

In this section, numerical results obtained by employing the proposed procedure are reported, for both the devices considered as case studies (see Fig. 4.3). In order to investigate the influence of material and geometrical parameters on their frequency

responses, a parametric analysis has been performed. Four different values are considered for the Young's moduli and layer thicknesses of involved materials (Y_{PVDF}, Y_{mylar} and T_{PVDF}, T_{mylar}, respectively). Analyses have been carried out by changing one parameter per time, keeping constant all the others at their reference values (i.e., values relative to the original configurations). Reference parametric set is reported in Table 4.1. Corresponding quantities will be referred to as E^0_{PVDF}, E^0_{mylar}, T^0_{PVDF}, T^0_{mylar} throughout the parametric analysis. Frequency Response Functions (FRFs) of tip displacements and output voltages, computed assuming a resistive electrical load of $R_L = 10\,M\Omega$, are reported for each case.

With reference to the rectangular cross section device, Figure 4.4 and Fig. 4.5 show the role of the piezoelectric elastic modulus Y_{PVDF} on the dynamic response for increasing values of the base acceleration amplitude. The influence of the substrate Young's modulus (Y_{mylar}) can be inferred from Fig. 4.6 and Fig. 4.7. Moreover, results of the parametric analyses relative to layer thicknesses are illustrated in Figures 4.8 -4.11.

Generally, it can be observed the occurrence of geometric stiffening effects, which induce a significant variation of the frequency at which the device exhibits the maximum tip displacement and output voltage. As an example, Fig. 4.4 shows for the original device configuration (case a), a peak displacement at 316 rad/s for small deformations (amplitude of the base excitation equal to or less than $1a_g$, with $a_g = 9.8$ m/s^2).

For very large deformations (amplitude of the base excitation equal to $10a_g$), the peak displacement is achieved at 350 rad/s. In such a case, an increment of the elastic modulus up to 60% shifts this frequency to 420 rad/s. With reference to the T-shaped device, Figure 4.12 and Fig. 4.13 illustrate the role of the piezoelectric elastic modulus Y_{PVDF} whereas Fig. 4.14 and Fig. 4.15 highlight the influence of the substrate thickness T_{mylar}. Qualitatively similar considerations can be done with respect to behaviors observed in the previous case.

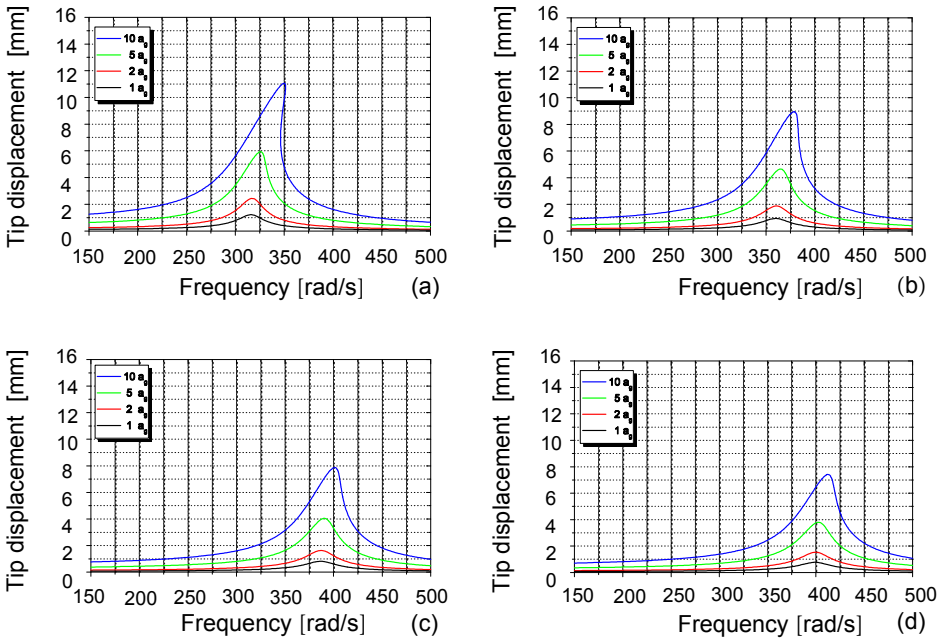

Figure 4.4: Device with rectangular cross-section: FRFs of the maximum tip displacement for base acceleration amplitudes ranging from $1a_g$ to $10a_g$, where a) $Y_{PVDF} = Y^0_{PVDF}$ b) $Y_{PVDF} = 1.2Y^0_{PVDF}$, c) $Y_{PVDF} = 1.4E^0_{PVDF}$, d) $Y_{PVDF} = 1.6Y^0_{PVDF}$.

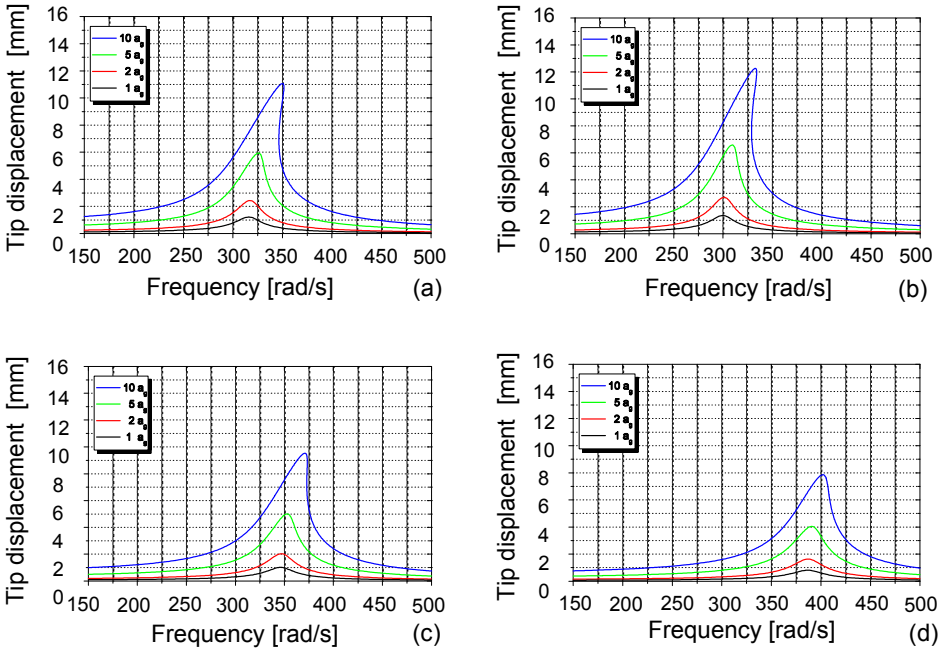

Figure 4.6: Device with rectangular cross-section: FRFs of the maximum tip displacement for base acceleration amplitudes ranging from $1a_g$ to $10a_g$, where a) $Y_{mylar} = Y^0_{mylar}$, b) $Y_{mylar} = 0.5Y^0_{mylar}$, c) $Y_{mylar} = 1.5Y^0_{mylar}$, d) $Y_{mylar} = 2.0Y^0_{mylar}$.

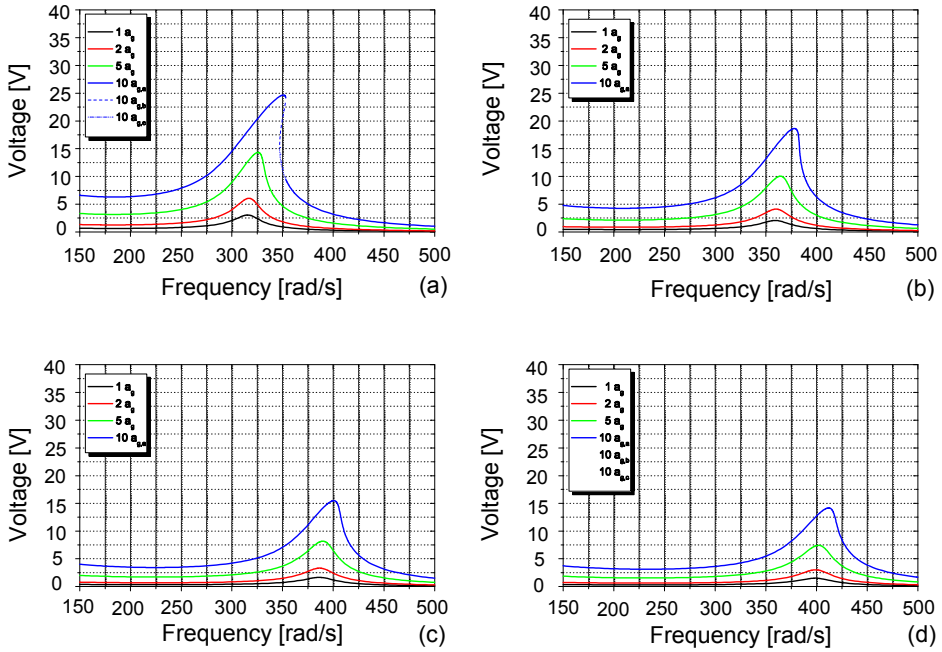

Figure 4.5: Device with rectangular cross-section: FRFs of the maximum voltage for base acceleration amplitudes ranging from $1a_g$ to $10a_g$, where a) $Y_{PVDF} = Y^0_{PVDF}$, b) $Y_{PVDF} = 1.2Y^0_{PVDF}$, c) $Y_{PVDF} = 1.4Y^0_{PVDF}$, d) $Y_{PVDF} = 1.6Y^0_{PVDF}$.

4.7 Validation

The experimental validation of the proposed procedure is discussed in this section, with reference to the case study characterized by the rectangular cross section. The considered configuration (see Fig. 4.3-a), whose relative parameters are summarized in Table 4.1, corresponds to the device under investigation in (69). Experimental evidences provided in (69) has proven that the device nonlinear response mainly depends on mechanical stiffening/softening effects. Therefore, parameters θ' and τ' in eq.set (4.4) can be considered negligible. The equivalent capacitance connected to the electrical port can be evaluated as follows:

$$C_p^{\text{eq}} = \frac{\varepsilon_{33} W L}{T_{PVDF}}, \tag{4.24}$$

where W, L, T_{PVDF} are width, length and the thickness of the piezoelectric layer respectively, and ε_{33} is the permittivity constant. Moreover, the generic electromechanical coupling term θ_r can be expressed, as a function of the rth shape mode, as follows (112):

$$\theta_r = \frac{Y_{PVDF} d_{31} W \left(2h_b + T_{PVDF}\right) \phi_r'(L)}{2}, \tag{4.25}$$

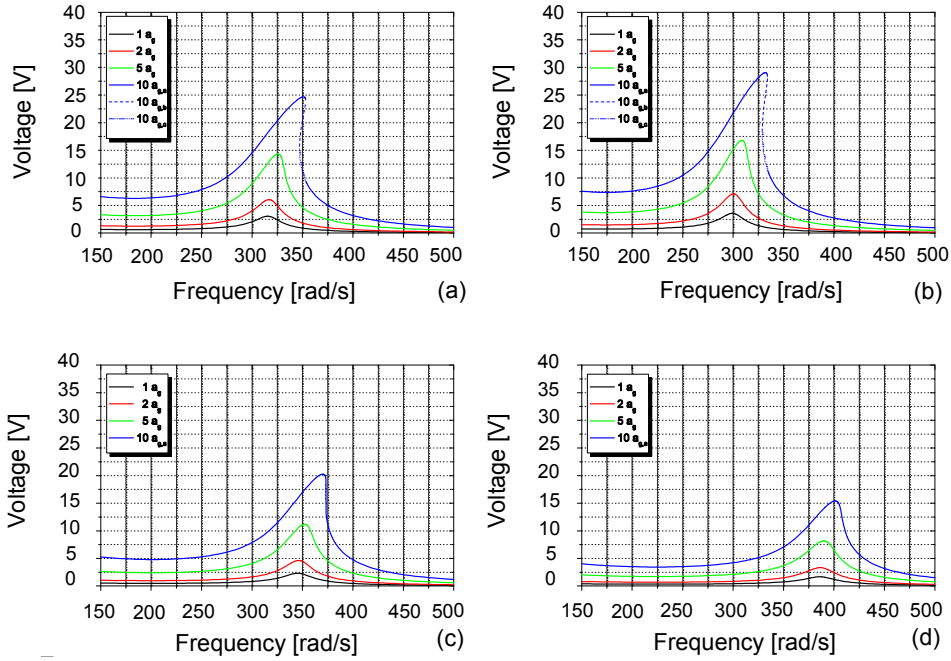

Figure 4.7: Device with rectangular cross-section: FRFs of the maximum voltage for base acceleration amplitudes ranging from $1a_g$ to $10a_g$, where a) $Y_{mylar} = Y^0_{mylar}$, b) $Y_{mylar} = 0.5Y^0_{mylar}$, c) $Y_{mylar} = 1.5Y^0_{mylar}$, d) $Y_{mylar} = 2.0Y^0_{mylar}$.

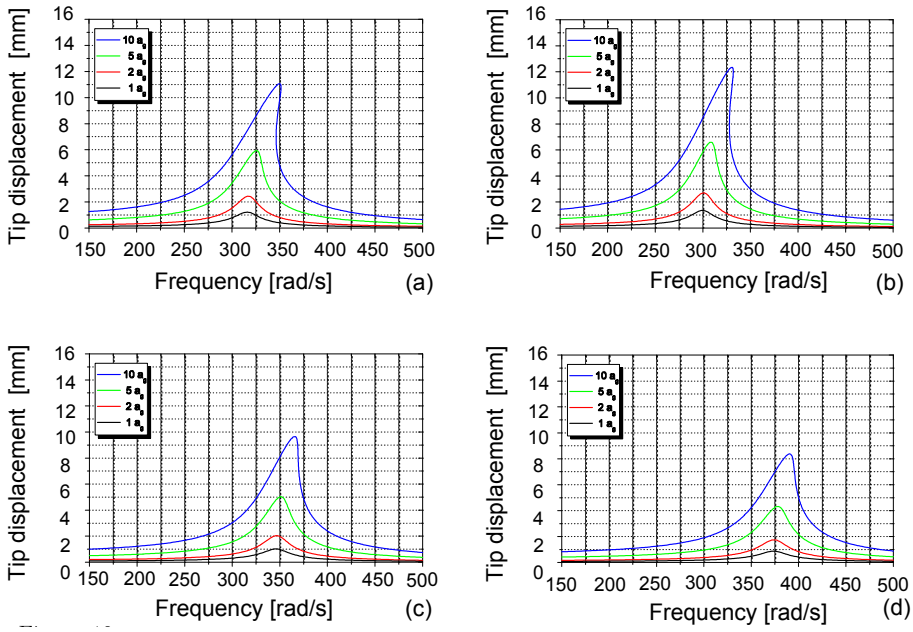

Figure 4.8: Device with rectangular cross-section: FRFs of the maximum tip displacement for base acceleration amplitudes ranging from $1a_g$ to $10a_g$, where a) $T_{PVDF} = T^0_{PVDF}$, b) $T_{PVDF} = 0.5T^0_{PVDF}$, c) $T_{PVDF} = 1.2T^0_{PVDF}$, d) $T_{PVDF} = 1.4T^0_{PVDF}$.

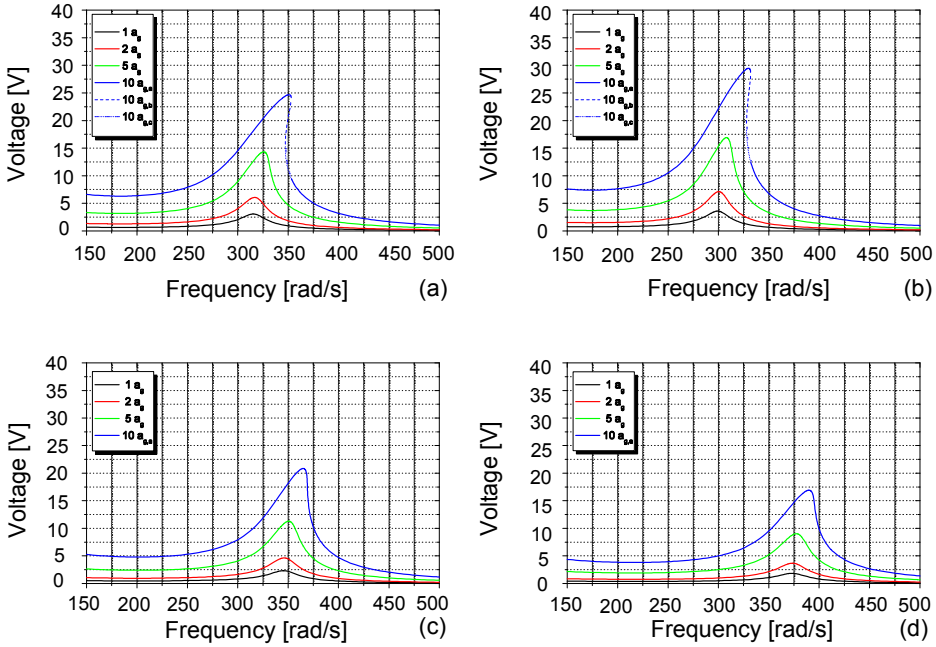

Figure 4.9: Device with rectangular cross-section: FRFs of the maximum voltage for base acceleration amplitudes ranging from $1a_g$ to $10a_g$, where a) $T_{PVDF} = T^0_{PVDF}$, b) $T_{PVDF} = 0.5T^0_{PVDF}$, c) $T_{PVDF} = 1.2T^0_{PVDF}$, d) $T_{PVDF} = 1.4T^0_{PVDF}$.

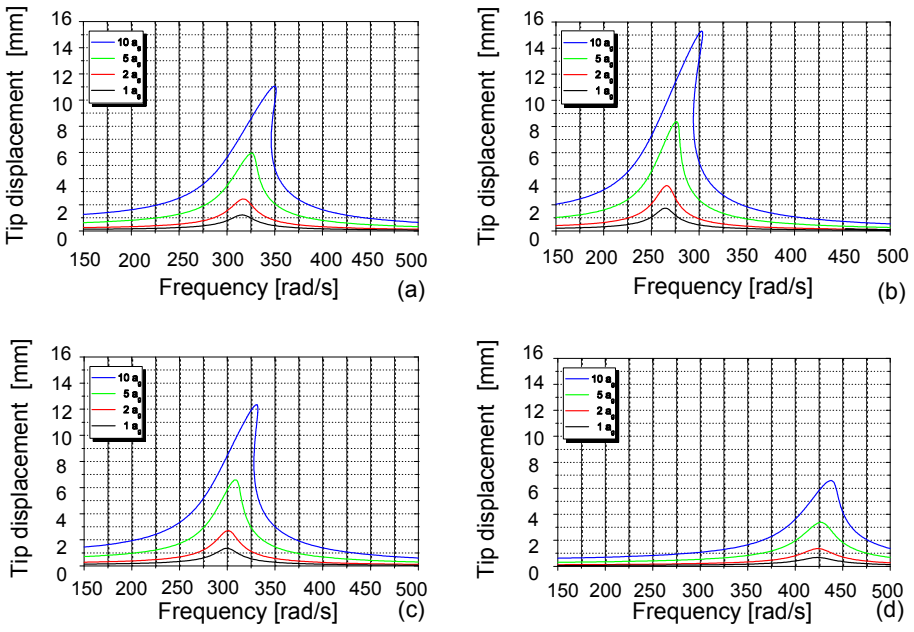

Figure 4.10: Device with rectangular cross-section: FRFs of the maximum tip displacement for base acceleration amplitudes ranging from $1a_g$ to $10a_g$, where a) $T_{mylar} = T^0_{mylar}$, b) $T_{mylar} = 0.8T^0_{mylar}$, c) $T_{mylar} = 0.9T^0_{mylar}$, d) $T_{mylar} = 1.2T^0_{mylar}$.

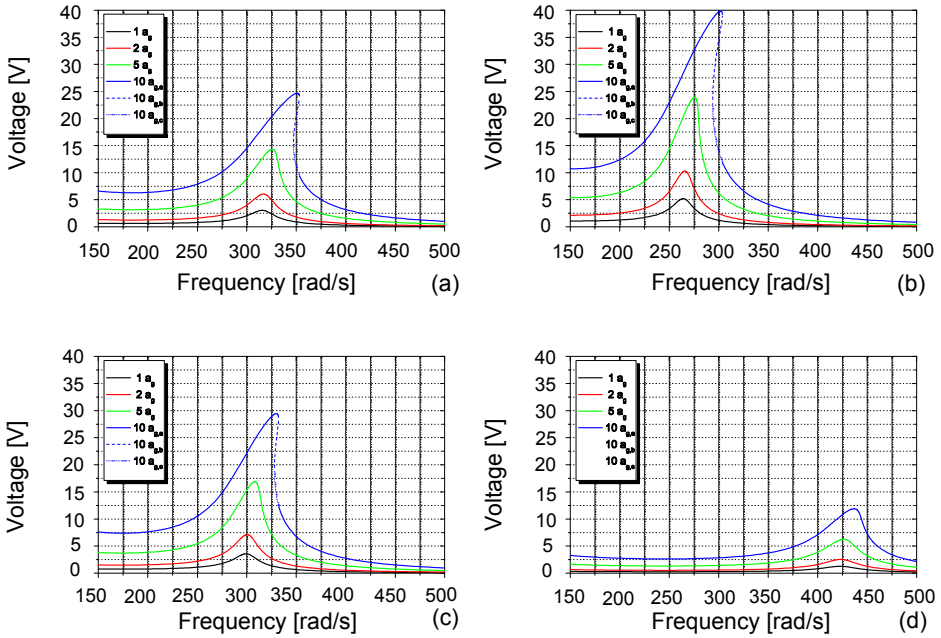

Figure 4.11: Device with rectangular cross-section: FRFs of the maximum voltage for base acceleration amplitudes ranging from $1a_g$ to $10a_g$, where a) $T_{mylar} = T^0_{mylar}$, b) $T_{mylar} = 0.8T^0_{mylar}$, c) $T_{mylar} = 0.9T^0_{mylar}$, d) $T_{mylar} = 1.2T^0_{mylar}$.

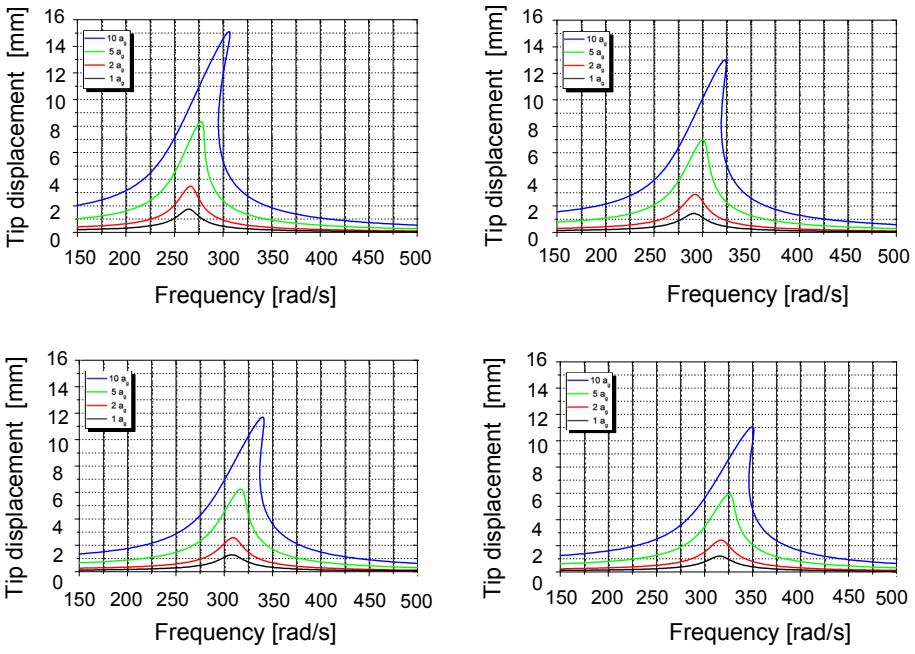

Figure 4.12: Device with T-shaped cross-section: FRFs of the maximum tip displacement for base acceleration amplitudes ranging from $1a_g$ to $10a_g$, where a) $Y_{PVDF} = Y^0_{PVDF}$, b) $Y_{PVDF} = 1.2Y^0_{PVDF}$, c) $Y_{PVDF} = 1.4Y^0_{PVDF}$, d) $Y_{PVDF} = 1.6Y^0_{PVDF}$.

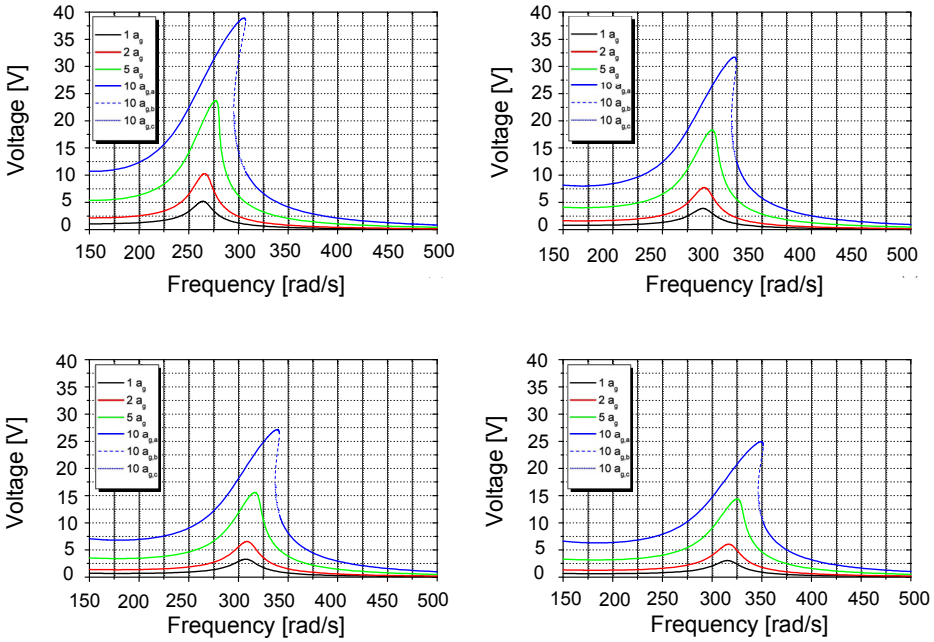

Figure 4.13: Device with T-shaped cross-section: FRFs of the maximum voltage for base acceleration amplitudes ranging from $1.a_g$ to $10a_g$, where a) $Y_{PVDF} = Y^0_{PVDF}$, b) $Y_{PVDF} = 1.2Y^0_{PVDF}$, c) $Y_{PVDF} = 1.4Y^0_{PVDF}$, d) $Y_{PVDF} = 1.6Y^0_{PVDF}$.

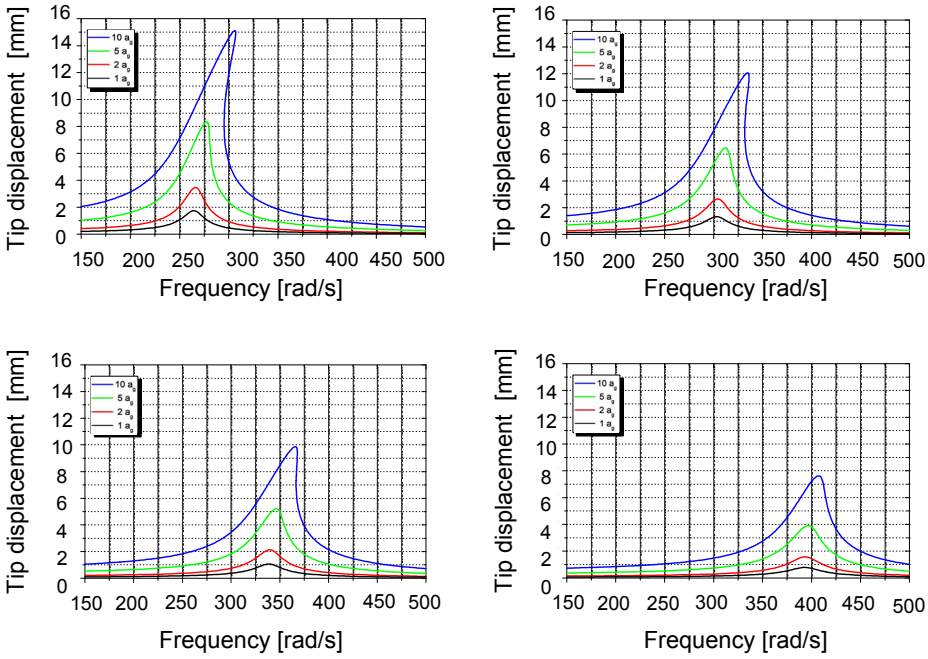

Figure 4.14: Device with T-shaped cross-section: FRFs of the maximum tip displacement for base acceleration amplitudes ranging from $1a_g$ to $10a_g$, where a) $T_{mylar} = T^0_{mylar}$, b) $T_{mylar} = 1.1T^0_{mylar}$, c) $T_{mylar} = 1.2T^0_{mylar}$, d) $T_{mylar} = 1.3T^0_{mylar}$.

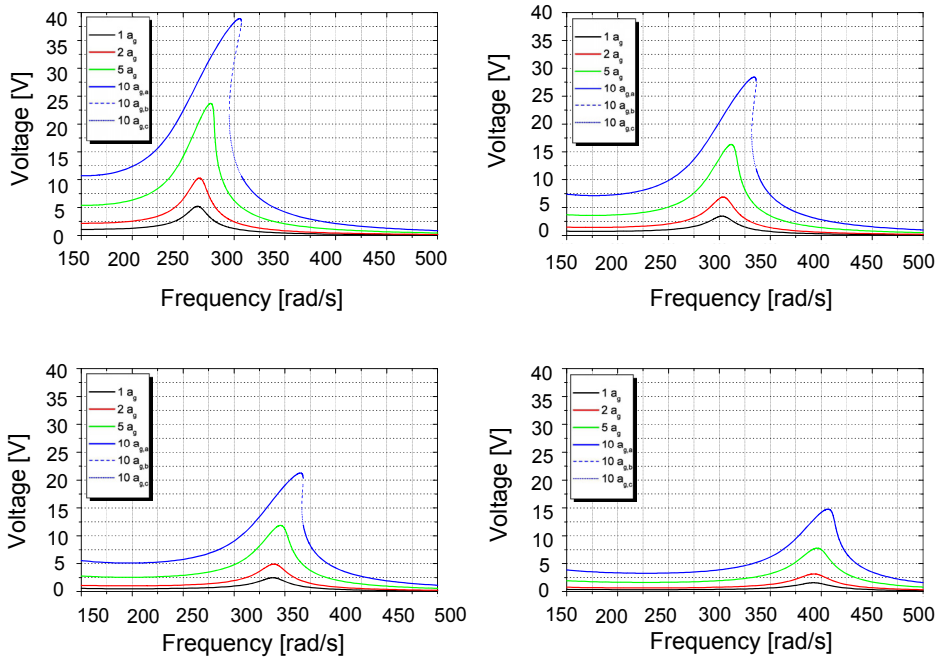

Figure 4.15: Device with T-shaped cross-section: FRFs of the maximum voltage for base acceleration amplitudes ranging from $1a_g$ to $10a_g$, where a) $T_{mylar} = T^0_{mylar}$, b) $T_{mylar} = 1.1T^0_{mylar}$, c) $T_{mylar} = 1.2T^0_{mylar}$, d) $T_{mylar} = 1.3T^0_{mylar}$.

where d_{31} is the piezoelectric coupling constant and h_b is the position of the bottom PVDF layer from the neutral axis. In (4.4), it results that $\theta_{r=1} = \theta$. Distance h_b is defined as $h_b = h_{pa} - T_{PVDF}$, where h_{pa} is the distance from the top of the PVDF layer to the neutral axis (112):

$$h_{pa} = \frac{T^2_{PVDF} + 2Y_R T_{mylar} T_{PVDF} + Y_R T^2_{PVDF}}{2\left(T_{mylar} + Y_R T_{PVDF}\right)} \ , \tag{4.26}$$

where $Y_R = Y_{mylar}/Y_{PVDF}$ is the ratio of the substrate Young's modulus (here assumed as made of mylar) to the Young's modulus of the PVDF material. T_{mylar} is the thickness of the supporting substrate.

Moreover, for a rectangular cross section, it results: $\theta = \tau$. As a consequence, the circuital component accounting for the coupling between mechanical and electrical ports in circuit 4.1 is equivalent to an ideal transformer with voltage ratio $\gamma^l = m\theta$. According to (72), the multi-morph structure concept has been used to physically and mathematically describe the equivalent stiffness of the piezoelectric energy harvester. A fixed-free cantilever configuration is assumed. Moreover, each multiple thin material film layer has length L width W and a thickness T_s. The same assumptions adopted for the PZT unimorph in section 3.4.2 are considered

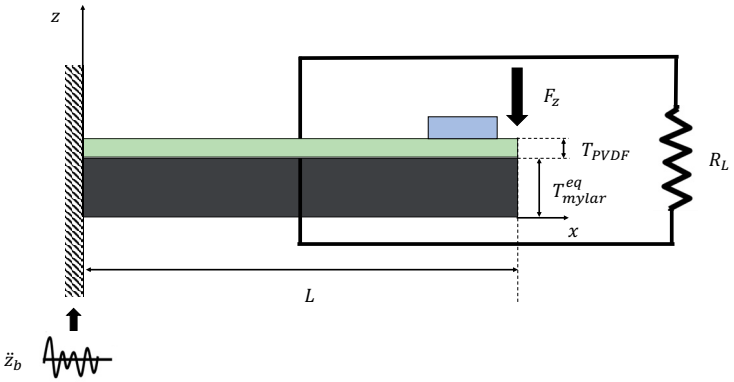

Figure 4.16: Device with rectangular cross-section: equivalent bi-layered configuration.

here: a) layer interfaces are smooth and continuous and do not slip with respect to each other; b) each layer is considered uniform with Youngs modulus Y_s, rotational inertial I_s and cross-sectional areas A_s=WT_s (where subscript s denotes the sth layer). The homogenized flexural rigidity about the neutral axis (YI) is given by (72): $YI = \sum_{s=1}^{N_{layer}} \left\{ A_s Y_s \left[(z_s - z_N)^2 + \frac{{T_s}^2}{12} \right] \right\}$, where N_{layer} is the number of layers considered (5 for the considered device), and $z_N = \sum_{s=1}^{N_{layer}} Y_s T_s z_s / \sum_{s=1}^{N_{layer}} Y_s T_s$ is the neutral axis position. z_s is the location of the axis of the sth layer with respect to an arbitrary reference. It is not necessary to use a FE discretization for each material layer. In fact, an equivalent mylar layer thickness (T^{eq}_{mylar}) is determined in such a way that the first resonance frequency, provided by experimental data ($\omega_1 \approx 316\, rad/sec$), is close to the one obtained by means of the homogenized stiffness. Even if each layer of the device can be explicitly accounted in the FE model, the use of an equivalent layer can result useful in order to reduce computational time in nonlinear analyses. Modeling thin layers, in fact, requires more refined meshes and might cause distortion phenomena of the elements at the interfaces between layers with different thicknesses. Fig. 4.16 and Fig. 4.17 report the equivalent device configuration considered for the FE model and a detail of the adopted mesh discretization, respectively.

Figure 4.18 reports the first four modal shapes and modal frequencies of the devices evaluated by FE analysis. The good agreement with experimental data reported in Fig. 4.23 confirms the validity of the simplifying approach.

Figure 4.19 compares the results of the large displacement analysis (performed by means of AceFEM and Comsol Multiphysics) with the experimental evidences provided in (69). The vertical tip displacements are normalized with respect to the

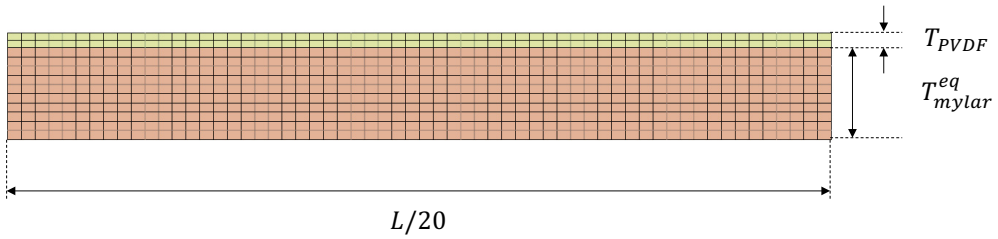

Figure 4.17: Device with rectangular cross-section: detail of the FE mesh discretization.

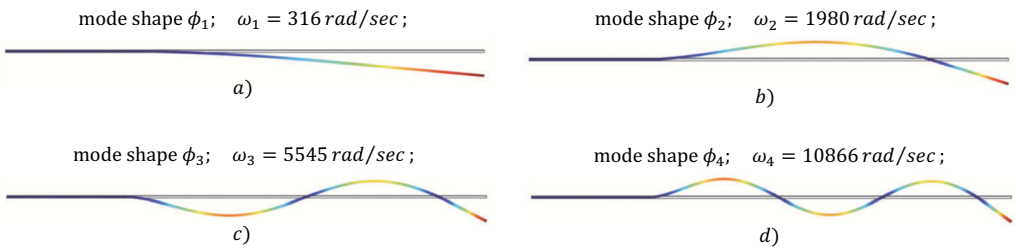

Figure 4.18: Device with rectangular cross-section: first four modal shapes and modal frequencies of the considered piezoelectric device.

beam length L while the load F_z is normalized with respect to the homogenized stiffness coefficient. Figure 4.19 shows a very good agreement between numerical predictions and experimental outcomes. Contour levels of the stress components σ_{yy} and deformed shape are shown in Fig. 4.20. Figure 4.21 shows the good agreement between the FE analysis and the approximation obtained by means of the analytical Duffing spring model.

The proposed approach has been further validated against new experimental data resulting from tests carried out on the considered device. The experimental testing equipment (which is sketched in Fig. 4.22) consists of a signal generator providing a controlled input voltage to the piezoelectric device and an analysis system with tools for signal processing and modal characterization. Modal data (i.e., natural frequencies and damping ratios) are extracted based on the SDOF curve-fitting of the FRF. The frequency response analysis is performed by evaluating the out-of-plane displacements of the piezoelectric cantilevers by a non-contact measurement system. An AC voltage signal, provided by the signal generator embedded into the vibrometer system, has been applied to the cantilever, thus resulting in the actuation and deflection of the tip. The cantilever is tested assuming a frequency sweep at a given voltage in order to measure the peak of the tip deflection. The measured first resonance frequency and damping ratio are 324 rad/sec (see Fig. 4.23) and

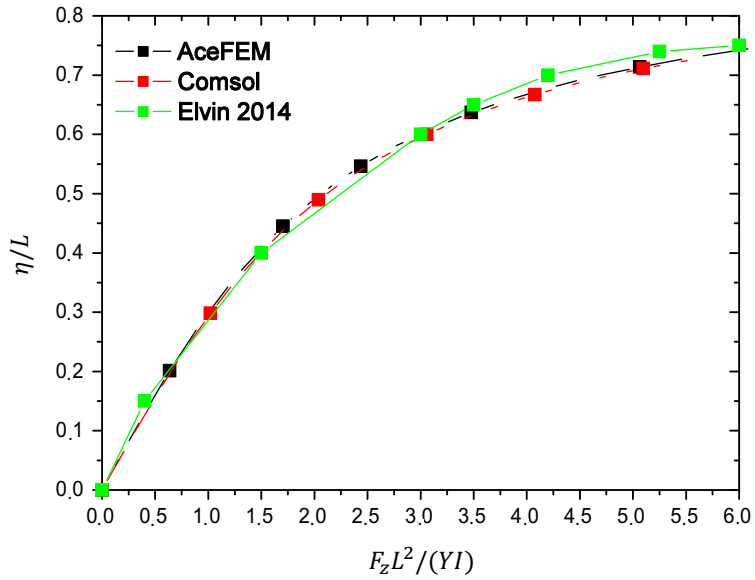

Figure 4.19: PVDF unimorph generator: normalized tip deflection δ_{tip} under a static loads. Comparison among FE solutions and experimental data.

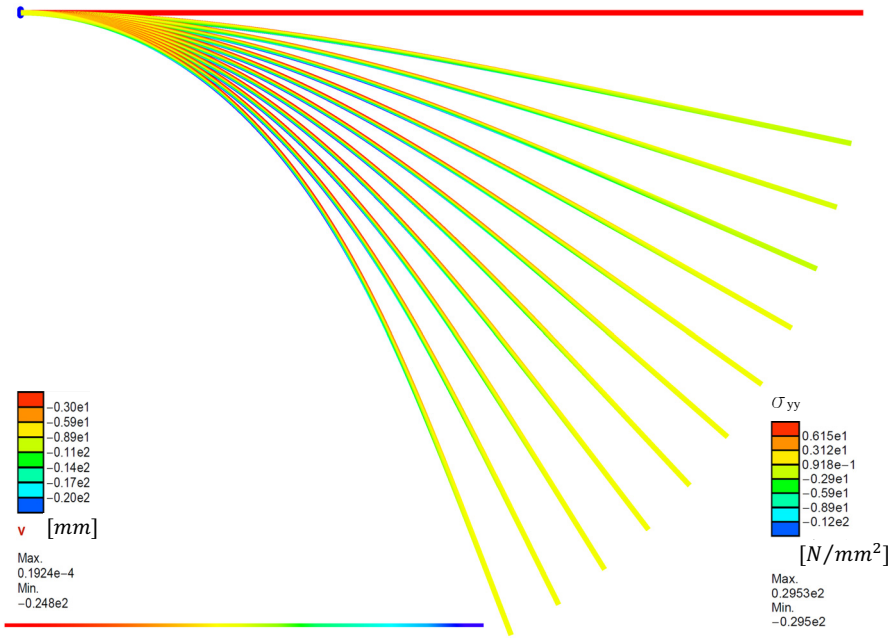

Figure 4.20: PVDF unimorph generator: contour levels of vertical displacement components and Cauchy stresses (color bars refer to the final load step).

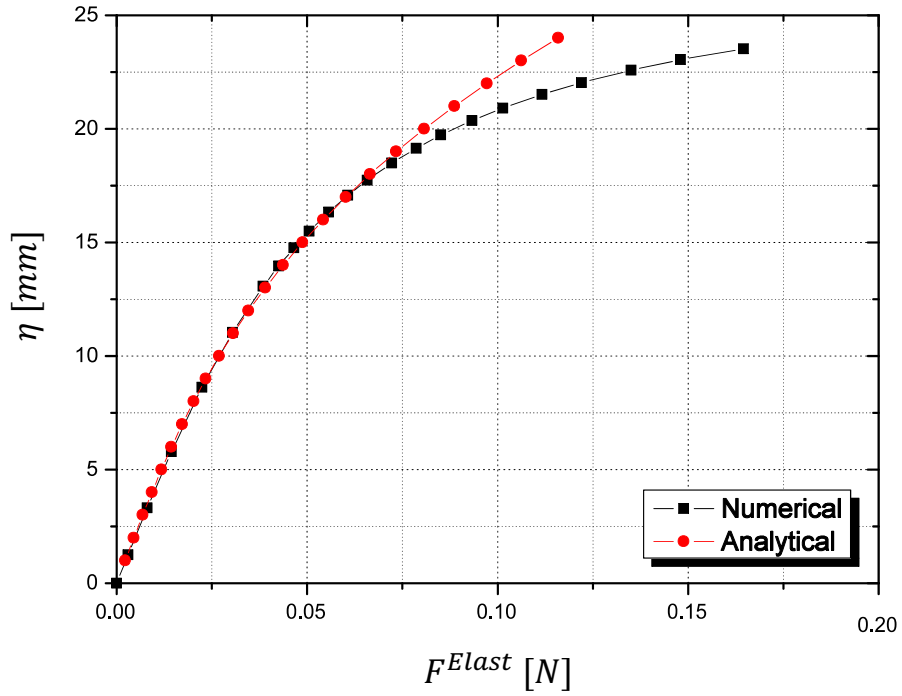

Figure 4.21: PVDF unimorph generator: FE-based capacity curves and analytical approximation.

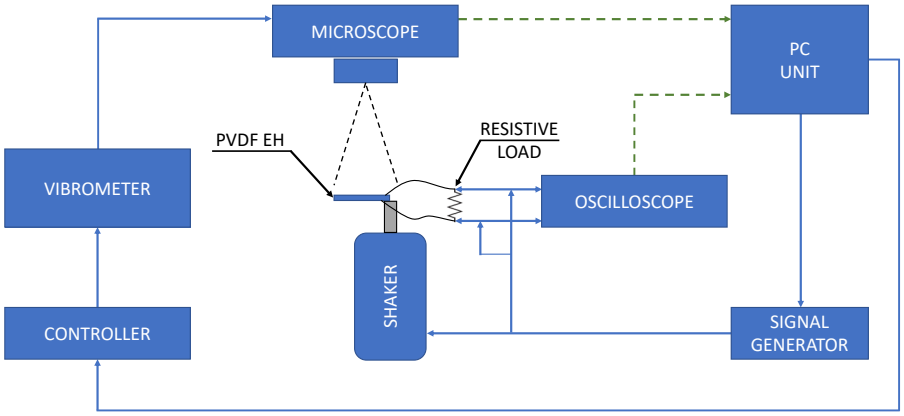

Figure 4.22: Block diagram of the experimental setup.

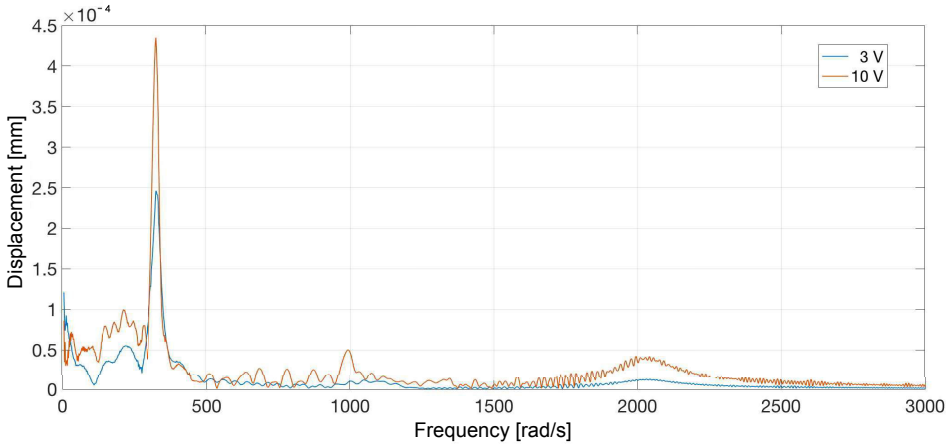

Figure 4.23: PVDF unimorph generator: experimental characterization of device natural frequencies for chirp signals of 3 V and 10 V.

4%, respectively. Moreover, two base acceleration time histories are considered for the experimental characterization of the device response under large strains. In particular, direct input accelerations - provided at the clamped end of the device by a shaker unit - are measured through a Laser Doppler Velocimeter (LDV) system by pointing the laser beam on the device clamped base. The harmonic dynamic inputs have amplitude equal to $3.7a_g$ and $10.5a_g$ while the frequency is 330 rad/sec. Magnitude spectra of exciting accelerations are provided in Fig. 4.24-a,b, along with magnitude spectra (Fig. 4.24-c,d) and time hystories (Fig. 4.24-e,f) of the measured output voltage. A $1\,M\Omega$ resistive load has been connected to the device electrodes for the considered test.

Time history plots reported in Fig. 4.24 show a comparison between the numerically predicted (red dashed curves) and experimental (blue solid curves) output voltages. After estimating parameters of the nonlinear spring through the comparison between the reduced-order model and the static FE problem solutions, equation set (4.4) is solved using a Runge–Kutta algorithm, providing numerical predictions of the tip displacement and/or velocity and the voltage on the electric load.

A good agreement between experimental evidences and numerical simulations can be observed, as confirmed by the results in Table 4.2.

Moreover, based on experimental evidences it is thus confirmed that for PVDF EHs a harmonic form can be assumed for tip displacement and output voltage waveforms in case of harmonic base accelerations. The corresponding amplitudes, whose analytical approximation is given by (4.17) and (4.22), have a nonlinear dependence with respect to the frequency of the input signal.

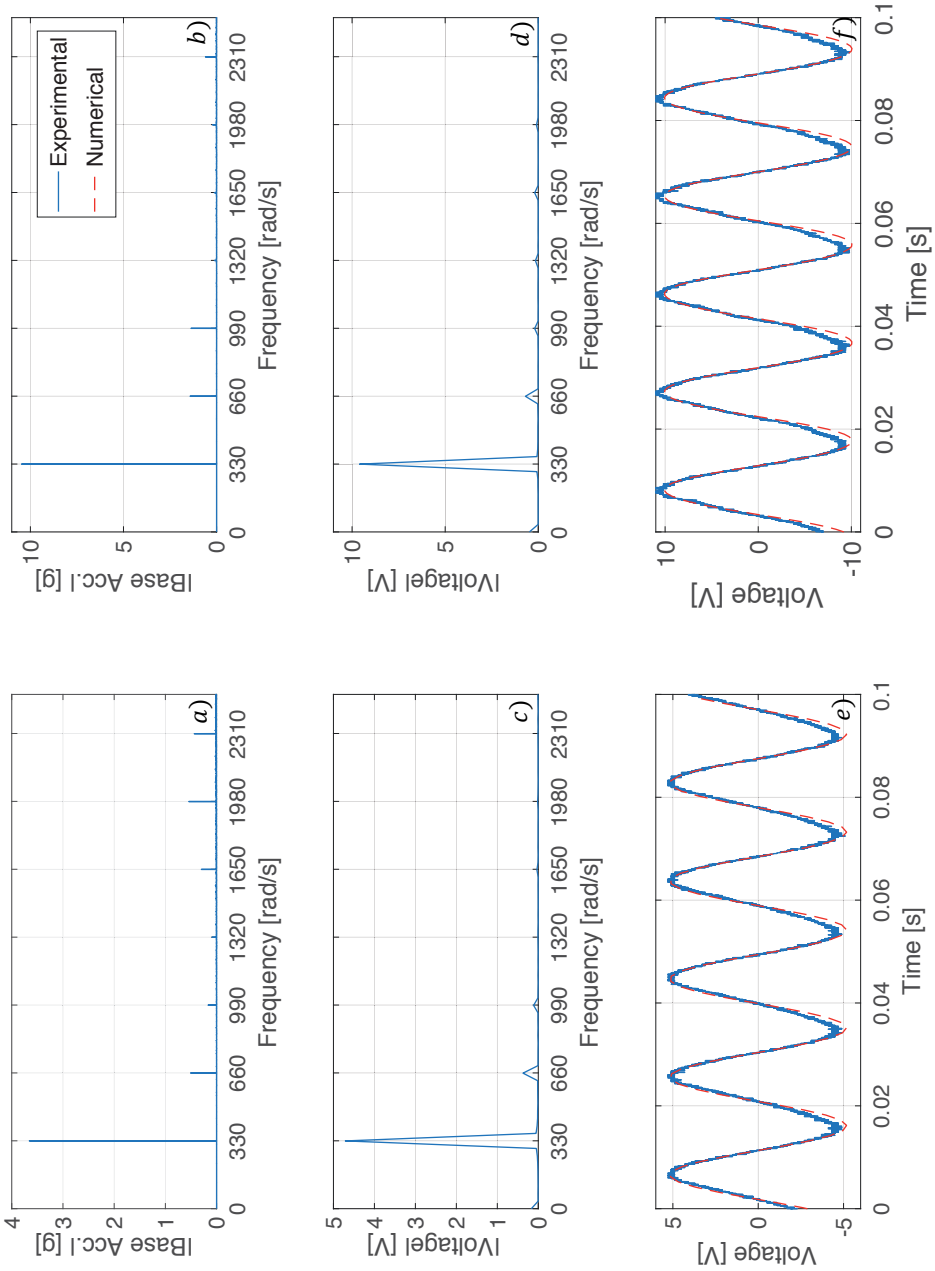

Figure 4.24: PVDF unimorph generator. FFT of $3.7a_g$ and $10.5a_g$ base accelerations (a-b); FFT of the measured output voltages (c-d); comparison among experimental (solid blue lines) and numerical (dashed red lines) output voltages for $3.7a_g$ and $10.5a_g$ base accelerations (e-f).

Table 4.2: Experimental vs numerical results

	Experimental voltage peak [V]	Numerical voltage peak [V]
$3.7a_g$	5.2	5.2
$10.5a_g$	10.3	10.1

4.8 Conclusion

In this chapter an innovative hybrid approach has been proposed for modeling the nonlinear dynamic response of piezoelectric cantilever beams.

Once the tip displacements are obtained as function of the load increments by means of a static nonlinear FE analyses, linear and nonlinear lumped coefficients of the spring element into the analytical Duffing model are calibrated in order to fit the reference nonlinear pushover curve. Finally, the nonlinear dynamic differential equations governing the response of the piezoelectric cantilever beam can be solved in order to estimate the frequency response functions of tip displacement and output voltage.

The attractive features of this computational procedure are twofold. From a numerical standpoint, the FE analysis is performed to solve a static problem, which is less time consuming than a dynamic problem.

Since the nonlinear behavior is reflected into the reduced-order model adopted for the dynamic analyses, through the comparison with FE-based capacity curves, devices with a larger bandwidth and better performances in the frequency range of interest can be fabricated. The experimental work needed for characterizing the device has been limited to the estimation of damping and natural frequencies of the device without nonlinear effects. It is not particularly time consuming and require ordinary laboratory facilities. A large parametric investigation has been also performed in order to assess the role of material and geometrical parameters on the nonlinear response of piezoelectric unimorphs for energy harvesting applications.

Reported results show that the proposed hybrid approach leads to satisfactory results while reducing the overall numerical and experimental efforts.

5

Conclusion

In this thesis, recent results on modeling the dynamic behavior of piezoelectric EHs are presented, with a major focus on two of the nonlinearity sources that can be identified for this kind of devices: hysteresis and geometric nonlinearities. Classical reduced-order modeling approaches have been enhanced by including effects of ferroelastic/ferroelectric hysteresis and large deformations, yielding to effective circuit representations that allow for an intuitive insight in the energy transduction process characterizing this kind of devices. Nonlinearity sources have been assessed in a separate way.

A physics based model has been employed in order to reproduce hysteretic dynamics of piezceramic single crystals. Through a multiscale approach, crystal mesoscopic evolution has been coupled to the dynamics of devices modeled as SDOF systems. Reported numerical investigations show that, even for low amplitudes of the input excitation, significant misprediction can result from ignoring material hysteresis. The physics-based feature of the proposed approach, allows for evaluating the role of crystal parameters on the device performances, providing an insight on how, through an engineered crystal design, material nonlinearities can be potentially exploited in order to improve generation performances.

Moreover, an effective hybrid computational framework is proposed with the aim of modeling geometric nonlinear effects on the response of flexible PVDF-based EHs under large deformations. The innovative strategy basically consists on performing a fully coupled multiphysics finite element (FE) analysis to evaluate the nonlinear static response of the device, so that an enhanced reduced-order model can be derived. Hence, the global dynamic response is formulated in the state-space using lumped coefficients enriched with the information derived from the FE simulations. Simulation results show that geometric nonlinearities results in a stiffening of the

devices considered as case studies, highlighting how the response bandwidth is a function of the input excitation amplitude. From a numerical standpoint, the proposed procedure - which has been validated against experimental evidences provided by other Researchers and new measures - is particularly attractive: even preserving a satisfactory accuracy, computational efforts are significantly reduced as FE analyses are performed for static problems while dynamic analyses are carried out through reduce-order models.

Future activities will be developed within two parallel work streams:

- improve multiscale models developed for PZT material nonlinearities by including polycrystalline behaviors;
- further validating the proposed approaches against experimental data.

Appendix A

Equivalence of proposed MsMs

Figure A.0.1 reports simulation results obtained assuming a $1g_{acc}$ sinusoidal base acceleration, in *near-resonance* condition, as input for the device.

Blue solid lines refer to the numerical integration of MsM (3.25). Red dashed line in Fig. A.0.1-c refers to the device output voltage determined by indirect calculation based on the application of the Kirchhoff's Voltage Law (KVL) to the equivalent lumped circuit in Fig. 3.12 (which is relative to the MsM (3.19)).

With reference to Fig. 3.12, by writing the KVL for the circuit loop connected to the mechanical port, the following expression of the device output voltage can be obtained:

$$v(t) = \frac{1}{\alpha^{MsM}} \left(-F_b + c_D \dot{\eta} + m\ddot{\eta} + \frac{A}{l_0 d}\eta - \frac{Af}{d} \right) , \tag{A.1}$$

where the evolution in time of quantities α^{MsM}, d, and f can be assumed the same as that provided by the numerical integration of MsM (3.25).

The same input quantities (F_b, $\dot{\eta}$) are considered applied to the mechanical port of both the models.

The perfect coincidence of curves reported in Fig. A.0.1-c confirms MsMs (3.19) and (3.25) equivalence in terms of input/output behavior.

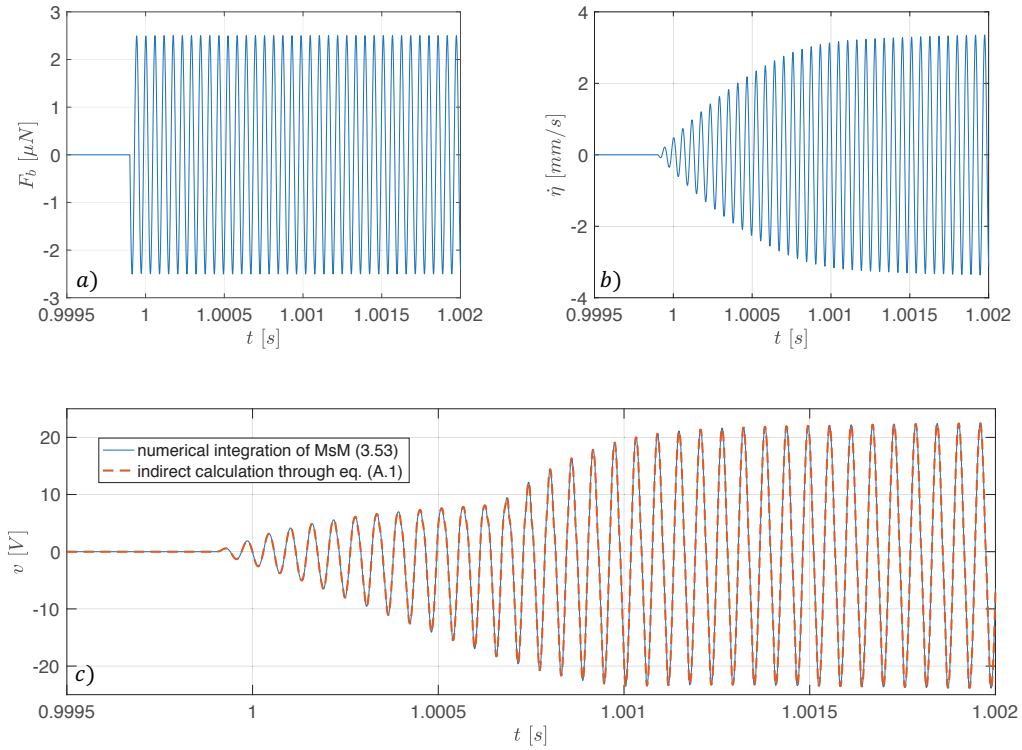

Figure A.0.1: Comparison between MsMs (3.19) and (3.25) responses: 1 g_{acc} input acceleration in *near-resonance* condition. Blue solid lines refer to numerical simulation of MsM (3.25). a) input force; b) rate of change of the system displacement; c) comparison between the output voltages provided by the two MsMs.

References

[1] Alexander York et al. **Experimental characterization and modeling of electro-mechanically coupled ferroelectric actuators**. 2008. ix, xv, 62, 63, 64, 65, 69, 70

[2] Howard Huff. *Into the nano era: Moore's law beyond planar silicon CMOS*, **106**. Springer Science & Business Media, 2008. 1

[3] Shashank Priya and Daniel J Inman. *Energy harvesting technologies*, **21**. Springer, 2009. 1

[4] Vasaki Ponnusamy. *Biologically-Inspired Energy Harvesting through Wireless Sensor Technologies*. IGI Global, 2016. 1

[5] Zhong Lin Wang and Jinhui Song. **Piezoelectric nanogenerators based on zinc oxide nanowire arrays**. *Science*, **312**(5771):242–246, 2006. 1

[6] Xudong Wang, Jinhui Song, Jin Liu, and Zhong Lin Wang. **Direct-current nanogenerator driven by ultrasonic waves**. *Science*, **316**(5821):102–105, 2007. 1

[7] Yong Qin, Xudong Wang, and Zhong Lin Wang. **Microfibre–nanowire hybrid structure for energy scavenging**. *Nature*, **451**(7180):809, 2008. 1

[8] J Hsin He, Cheng L Hsin, Jin Liu, Lih J Chen, and Zhong L Wang. **Piezoelectric gated diode of a single ZnO nanowire**. *Advanced Materials*, **19**(6):781–784, 2007. 1

[9] Chang Shi Lao, Qin Kuang, Zhong L Wang, Myung-Chul Park, and Yulin Deng. **Polymer functionalized piezoelectric-FET as humidity/chemical nanosensors**. *Applied physics letters*, **90**(26):262107, 2007. 1

[10] Youfan Hu, Yanling Chang, Peng Fei, Robert L Snyder, and Zhong Lin Wang. **Designing the electric transport characteristics of ZnO micro/nanowire devices by coupling piezoelectric and photoexcitation effects**. *ACS nano*, **4**(2):1234–1240, 2010. 1

[11] Youfan Hu, Yan Zhang, Yanling Chang, Robert L Snyder, and Zhong Lin Wang. **Optimizing the power output of a ZnO photocell by piezopotential**. *ACS nano*, **4**(7):4220–4224, 2010. 1

[12] Canan Dagdeviren. *Ferroelectric/piezoelectric flexible mechanical energy harvesters and stretchable epidermal sensors for medical applications*. PhD thesis, University of Illinois at Urbana-Champaign, 2015. 1

[13] Claudio Maruccio, Giuseppe Quaranta, Laura De Lorenzis, and Giorgio Monti. **Energy harvesting from electrospun piezoelectric nanofibers for structural health monitoring of a cable-stayed bridge**. *Smart Materials and Structures*, **25**(8):085040, 2016. 1, 98

[14] Maurizio Di Paolo Emilio. *Microelectronic circuit design for energy harvesting systems*. Springer, 2017. 1

[15] Tamara Bechtold, Gabriele Schrag, and Lihong Feng. *System-level Modeling of MEMS*. John Wiley & Sons, 2012. 1

[16] Jacob Fish. *Multiscale methods: bridging the scales in science and engineering*. Oxford University Press on Demand, 2010. 1

[17] Ercan M Dede, Jaewook Lee, and Tsuyoshi Nomura. *Multiphysics simulation: electromechanical system applications and optimization*. Springer, 2014. 1

[18] William BJ Zimmerman. *Multiphysics modeling with finite element methods*, **18**. World Scientific Publishing Company, 2006. 1

[19] Luciano Guerriero. *Lezioni di elettromagnetismo*. Adriatica, 1987. 11, 14, 18

[20] Manfred Kaltenbacher. *Numerical simulation of mechatronic sensors and actuators*, **2**. Springer, 2007. 17, 21, 24

[21] Alberto Carpintieri. *Scienza delle costruzioni*. Pitagora Editrice, 1992. 19

[22] Ferroelectrics Standards Committee of the IEEE Ultrasonics and Frequency Control Society. **IEEE Standard on Piezoelectricity**, 1987. 43, 44

[23] Jiashi Yang. *An introduction to the theory of piezoelectricity*, **9**. Springer Science & Business Media, 2004. 46, 50

[24] Vincent Piefort. *Finite element modelling of piezoelectric active structures*. PhD thesis, Ph. D. thesis. Bruxelles, Belgium: Université Libre de Bruxelles, Department for Mechanical Engineering and Robotics, 2001. 54, 56

[25] QM Zhang, WY Pan, SJ Jang, and LE Cross. **Domain wall excitations and their contributions to the weak-signal response of doped lead zirconate titanate ceramics**. *Journal of applied physics*, **64**(11):6445–6451, 1988. 62

[26] Sang-Joo Kim and Stefan Seelecke. **A rate-dependent three-dimensional free energy model for ferroelectric single crystals**. *International Journal of Solids and Structures*, **44**(3-4):1196–1209, 2007. 62, 68, 71

[27] SC Hwang, CS Lynch, and RM McMeeking. **Ferroelectric/ferroelastic interactions and a polarization switching model**. *Acta metallurgica et materialia*, **43**(5):2073–2084, 1995. 62

[28] M. Al Janaideh, S. Rakheja, and C. Y. Su. **Experimental characterization and modeling of rate-dependent hysteresis of a piezoceramic actuator**. *Mechatronics*, **19**:656–670, 2009. 63

[29] Xiaobo Tan and John S Baras. **Modeling and control of hysteresis in magnetostrictive actuators**. *Automatica*, **40**(9):1469–1480, 2004. 63

REFERENCES

[30] Isaak D Mayergoyz. *Mathematical models of hysteresis and their applications*. Academic Press, 2003. 63

[31] SR Viswamurthy and Ranjan Ganguli. **Modeling and compensation of piezoceramic actuator hysteresis for helicopter vibration control**. *Sensors and Actuators A: Physical*, **135**(2):801–810, 2007. 63

[32] X. Qingsong and T. Kok Kiong. *Advanced Control of Piezoelectric Micro-/Nano-Positioning Systems*. Springer International Publishing, 2016. 63

[33] X. Qingsong and L. Yangmin. **Dahl Model-Based Hysteresis Compensation and Precise Positioning Control of an XY Parallel Micromanipulator With Piezoelectric Actuation**. *Journal of Dynamic Systems Measurement and Control*, **132**, 2010. 63

[34] G. Song, J. Zhao, X. Zhou, and J. A. De Abreu-Garcia. **Tracking control of a piezoceramic actuator with hysteresis compensation using inverse Preisach model**. *IEEE/ASME Transactions on Mechatronics*, **10**:198–209, 2005. 63

[35] S. Mittal and C. Menq. **Hysteresis compensation in electromagnetic actuators through Preisach model inversion**. *IEEE/ASME Transactions on Mechatronics*, **5**(4):394–409, Dec 2000. 63

[36] Declan Hughes and John T Wen. **Preisach modeling of piezoceramic and shape memory alloy hysteresis**. *Smart materials and structures*, **6**(3):287, 1997. 63

[37] Vahid Hassani, Tegoeh Tjahjowidodo, and Thanh Nho Do. **A survey on hysteresis modeling, identification and control**. *Mechanical systems and signal processing*, **49**(1-2):209–233, 2014. 64

[38] Xuefeng Yang, Wei Li, Yuqiao Wang, Guo Ye, and Xiuping Su. **Hysteresis modeling of piezo actuator using neural networks**. In *Robotics and Biomimetics, 2008. ROBIO 2008. IEEE International Conference on*, pages 988–991. IEEE, 2009. 64

[39] Jung-Kyu N Park and Gregory N Washington. **Prediction of hysteretic effects in PZT stack actuators using a hybrid modeling strategy**. In *Smart Structures and Materials 2004: Modeling, Signal Processing, and Control*, **5383**, pages 48–60. International Society for Optics and Photonics, 2004. 64

[40] Miaolei Zhou, Shoubin Wang, and Wei Gao. **Hysteresis modeling of magnetic shape memory alloy actuator based on Krasnosel'skii-Pokrovskii model**. *The Scientific World Journal*, **2013**, 2013. 64

[41] Mei-Ju Yang, Chun-Xia Li, Guo-Ying Gu, and Li-Min Zhu. **A Modified Prandtl-Ishlinskii Model for Rate-dependent Hysteresis Nonlinearity Using m th-power Velocity Damping Mechanism**. *International Journal of Advanced Robotic Systems*, **11**(10):163, 2014. 64

[42] Mohammad Al Janaideh, Chun-Yi Su, and Subash Rakheja. **Development of the rate-dependent Prandtl–Ishlinskii model for smart actuators**. *Smart Materials and Structures*, **17**(3):035026, 2008. 64

[43] Donald Croft and Santosh Devasia. **Hysteresis and vibration compensation for piezoactuators**. *Journal of guidance, control, and dynamics*, **21**(5):710–717, 1998. 64

[44] R Ben Mrad and H Hu. **A model for voltage-to-displacement dynamics in piezoceramic actuators subject to dynamic-voltage excitations**. *IEEE/ASME transactions on mechatronics*, **7**(4):479–489, 2002. 64

[45] Shunli Xiao and Yangmin Li. **Modeling and High Dynamic Compensating the Rate-Dependent Hysteresis of Piezoelectric Actuators via a Novel Modified Inverse Preisach Model.** *IEEE Trans. Contr. Sys. Techn.*, **21**(5):1549–1557, 2013. 64

[46] Hewon Jung, Jong Youp Shim, and DaeGab Gweon. **Tracking control of piezoelectric actuators**. *Nanotechnology*, **12**(1):14, 2001. 64

[47] Wei Tech Ang, Francisco Alija Garmón, Pradeep K Khosla, and Cameron N Riviere. **Modeling rate-dependent hysteresis in piezoelectric actuators**. In *Proceedings 2003 IEEE/RSJ International Conference on Intelligent Robots and Systems (IROS 2003)(Cat. No. 03CH37453)*, **2**, pages 1975–1980. IEEE, 2003. 64

[48] R. C. Smith and Z. Ounaies. **A Domain Wall Model for Hysteresis in Piezoelectric Materials**. *Intelligent Material Systems and Structures*, **11**:62–79, 2000. 65

[49] Ralph C Smith, Stefan Seelecke, and Zoubeida Ounaies. **Free energy model for piezoceramic materials**. In *Smart Structures and Materials 2002: Modeling, Signal Processing, and Control*, **4693**, pages 183–191. International Society for Optics and Photonics, 2002. 65

[50] Ralph C Smith and Stefan Seelecke. **Energy formulation for Preisach models**. In *Smart Structures and Materials 2002: Modeling, Signal Processing, and Control*, **4693**, pages 173–183. International Society for Optics and Photonics, 2002. 65

[51] Ralph C Smith, Andrew Hatch, and Tathagata De. **Model development for piezoceramic nanopositioners**. In *Decision and Control, 2003. Proceedings. 42nd IEEE Conference on*, **3**, pages 2638–2643. IEEE, 2003. 65

[52] Ralph C Smith, Stefan Seelecke, Marcelo J Dapino, and Zoubeida Ounaies. **A unified model for hysteresis in ferroic materials**. In *Smart Structures and Materials 2003: Modeling, Signal Processing, and Control*, **5049**, pages 88–100. International Society for Optics and Photonics, 2003. 65

[53] Ralph C Smith, Stefan Seelecke, Zoubeida Ounaies, and Joshua Smith. **A free energy model for hysteresis in ferroelectric materials**. *Journal of intelligent material systems and structures*, **14**(11):719–739, 2003. 65

[54] Ralph C Smith, Andrew G Hatch, Binu Mukherjee, and Shifang Liu. **A homogenized energy model for hysteresis in ferroelectric materials: General density formulation**. *Journal of intelligent material systems and structures*, **16**(9):713–732, 2005. 65

[55] Ralph C Smith, Stefan Seelecke, Marcelo Dapino, and Zoubeida Ounaies. **A unified framework for modeling hysteresis in ferroic materials**. *Journal of the Mechanics and Physics of Solids*, **54**(1):46–85, 2006. 65

[56] M Achenbach and I Muller. **Simulation of material behavior of alloys with shape memory**. 1985. 65

[57] Manfred Achenbach. **A model for an alloy with shape memory**. *International Journal of Plasticity*, **5**(4):371–395, 1989. 65

[58] Ingo Müller and Stefan Seelecke. **Thermodynamic aspects of shape memory alloys**. *Mathematical and computer modelling*, **34**(12-13):1307–1355, 2001. 65

[59] Stefan Seelecke and Ingo Muller. **Shape memory alloy actuators in smart structures: Modeling and simulation**. *Applied Mechanics Reviews*, **57**(1):23–46, 2004. 65

[60] Alexander York and Stefan Seelecke. **An electromechanically coupled SDOF piezoelectric stack actuator model**. In *Modeling, Signal Processing, and Control for Smart Structures 2008*, **6926**, page 692608. International Society for Optics and Photonics, 2008. 65, 67, 68

[61] H Sahota. **Simulation of butterfly loops in ferroelectric materials**. *Continuum Mechanics and Thermodynamics*, **16**(1-2):163–175, 2004. 65

[62] Pasquale Montegiglio, Claudio Maruccio, Giuseppe Acciani, Gianluca Rizzello, and Stefan Seelecke. **Nonlinear multi-scale dynamics modeling of a piezoelectric energy harvester**. In *Environment and Electrical Engineering (EEEIC), 2018 IEEE 18th International Conference on*. IEEE, 2018. 73

[63] Pasquale Montegiglio, Claudio Maruccio, Giuseppe Acciani, Gianluca Rizzello, and Stefan Seelecke. **Nonlinear multi-scale dynamics modeling of a piezoelectric energy harvester**. 2018. 73

[64] Pasquale Montegiglio, Claudio Maruccio, and Giuseppe Acciani. **Nonlinear Physics-based Modeling of a Piezoelectric Energy Harvester**. *IFAC-PapersOnLine*, **51**(2):707–712, 2018. 73

[65] Xin Cui, Xia Ni, and Yan Zhang. **Theoretical study of output of piezoelectric nanogenerator based on composite of PZT nanowires and polymers**. *Journal of Alloys and Compounds*, **675**:306–310, 2016. 81

[66] A Erturk and DJ Inman. **Parameter identification and optimization in piezoelectric energy harvesting: analytical relations, asymptotic analyses, and experimental validations**. *Proceedings of the Institution of Mechanical Engineers, Part I: Journal of Systems and Control Engineering*, **225**(4):485–496, 2011. 82

[67] Koliann Mam, Michael Peigney, and Dominique Siegert. **Finite strain effects in piezoelectric energy harvesters under direct and parametric excitations**. *Journal of Sound and Vibration*, **389**:411–437, 2017. 88

[68] R. Andosca, T.G. McDonald, V. Genova, S. Rosenberg, J. Keatingd, C. Benedixen, and J. Sua. **Experimental and theoretical studies on MEMS piezoelectric vibrational energy harvesters with mass loading**. *Sensors and Actuators A*, **178**:76–87, 2012. 90

[69] Niell G Elvin and Alex A Elvin. **Large deflection effects in flexible energy harvesters**. *Journal of Intelligent Material Systems and Structures*, **23**(13):1475–1484, 2012. 93, 97, 105, 106, 110, 116

[70] S Adhikari, MI Friswell, and DJ Inman. **Piezoelectric energy harvesting from broadband random vibrations**. *Smart Materials and Structures*, **18**(11):115005, 2009. 97

[71] Mohammad I Younis. **Elements of Lumped-Parameter Modeling in MEMS**. In *MEMS Linear and Nonlinear Statics and Dynamics*, pages 97–153. Springer, 2011. 97

[72] Robert Andosca, T Gus McDonald, Vincent Genova, Steven Rosenberg, Joseph Keating, Cole Benedixen, and Junru Wu. **Experimental and theoretical studies on MEMS piezoelectric vibrational energy harvesters with mass loading**. *Sensors and Actuators A: Physical*, **178**:76–87, 2012. 97, 115, 116

[73] Sihong Zhao and Alper Erturk. **Electroelastic modeling and experimental validations of piezoelectric energy harvesting from broadband random vibrations of cantilevered bimorphs**. *Smart Materials and Structures*, **22**(1):015002, 2012. 97

[74] Mostafa RA Nabawy and William J Crowther. **Dynamic electromechanical coupling of piezoelectric bending actuators**. *Micromachines*, **7**(1):12, 2016. 97

[75] Mohammed F Daqaq, Ravindra Masana, Alper Erturk, and D Dane Quinn. **On the role of nonlinearities in vibratory energy harvesting: a critical review and discussion**. *Applied Mechanics Reviews*, **66**(4):040801, 2014. 97

[76] Samuel C Stanton, Clark C McGehee, and Brian P Mann. **Reversible hysteresis for broadband magnetopiezoelastic energy harvesting**. *Applied Physics Letters*, **95**(17):174103, 2009. 97

[77] Alper Erturk, J Hoffmann, and DJ Inman. **A piezomagnetoelastic structure for broadband vibration energy harvesting**. *Applied Physics Letters*, **94**(25):254102, 2009. 97

[78] AF Arrieta, P Hagedorn, Alper Erturk, and DJ Inman. **A piezoelectric bistable plate for nonlinear broadband energy harvesting**. *Applied Physics Letters*, **97**(10):104102, 2010. 97

[79] AJ Sneller, P Cette, and BP Mann. **Experimental investigation of a post-buckled piezoelectric beam with an attached central mass used to harvest energy**. *Proceedings of the Institution of Mechanical Engineers, Part I: Journal of Systems and Control Engineering*, **225**(4):497–509, 2011. 97

[80] Lihua Tang, Yaowen Yang, and Chee Kiong Soh. **Toward broadband vibration-based energy harvesting**. *Journal of intelligent material systems and structures*, **21**(18):1867–1897, 2010. 97

[81] Sergio P Pellegrini, Nima Tolou, Mark Schenk, and Just L Herder. **Bistable vibration energy harvesters: a review**. *Journal of Intelligent Material Systems and Structures*, **24**(11):1303–1312, 2013. 97

[82] RL Harne and KW Wang. **A review of the recent research on vibration energy harvesting via bistable systems**. *Smart materials and structures*, **22**(2):023001, 2013. 97

[83] K Das and RC Batra. **Pull-in and snap-through instabilities in transient deformations of microelectromechanical systems**. *Journal of Micromechanics and Microengineering*, **19**(3):035008, 2009. 97

[84] A Erturk and DJ Inman. **Broadband piezoelectric power generation on high-energy orbits of the bistable Duffing oscillator with electromechanical coupling**. *Journal of Sound and Vibration*, **330**(10):2339–2353, 2011. 97

[85] Helios Vocca, Igor Neri, Flavio Travasso, and Luca Gammaitoni. **Kinetic energy harvesting with bistable oscillators**. *Applied Energy*, **97**:771–776, 2012. 97

[86] Bruno Ando, Salvatore Baglio, Gaetano L'Episcopo, and Carlo Trigona. **Investigation on mechanically bistable MEMS devices for energy harvesting from vibrations**. *Journal of Microelectromechanical Systems*, **21**(4):779–790, 2012. 97

[87] Lars-Cyril Julin Blystad and Einar Halvorsen. **A piezoelectric energy harvester with a mechanical end stop on one side**. *Microsystem technologies*, **17**(4):505–511, 2011. 97

[88] Huicong Liu, Chengkuo Lee, Takeshi Kobayashi, Cho Jui Tay, and Chenggen Quan. **Investigation of a MEMS piezoelectric energy harvester system with a frequency-widened-bandwidth mechanism introduced by mechanical stoppers**. *Smart Materials and Structures*, **21**(3):035005, 2012. 97

[89] Cuong P Le, Einar Halvorsen, Oddvar Søråsen, and Eric M Yeatman. **Microscale electrostatic energy harvester using internal impacts**. *Journal of Intelligent Material Systems and Structures*, **23**(13):1409–1421, 2012. 97

[90] Philippe Basset, Dimitri Galayko, Francesco Cottone, Raphaël Guillemet, Elena Blokhina, Frédéric Marty, and Tarik Bourouina. **Electrostatic vibration energy harvester with combined effect of electrical nonlinearities and mechanical impact**. *Journal of Micromechanics and Microengineering*, **24**(3):035001, 2014. 97

[91] H Li, S Preidikman, B Balachandran, and CD Mote Jr. **Nonlinear free and forced oscillations of piezoelectric microresonators**. *Journal of Micromechanics and Microengineering*, **16**(2):356, 2006. 97

[92] L Gammaitoni, I Neri, and H Vocca. **Nonlinear oscillators for vibration energy harvesting**. *Applied Physics Letters*, **94**(16):164102, 2009. 97

[93] Son D Nguyen and Einar Halvorsen. **Nonlinear springs for bandwidth-tolerant vibration energy harvesting**. *Journal of Microelectromechanical Systems*, **20**(6):1225–1227, 2011. 97

[94] Pierre Ueberschlag. **PVDF piezoelectric polymer**. *Sensor review*, **21**(2):118–126, 2001. 97

[95] C Maruccio and L De Lorenzis. **Numerical homogenization of piezoelectric textiles with electrospun fibers for energy harvesting**. *Frattura ed Integrità Strutturale*, **8**(29):49–60, 2014. 98

[96] Luana Persano, Canan Dagdeviren, Claudio Maruccio, Laura De Lorenzis, and Dario Pisignano. **Cooperativity in the enhanced piezoelectric response of polymer nanowires**. *Advanced Materials*, **26**(45):7574–7580, 2014. 98

[97] Claudio Maruccio, Laura De Lorenzis, Luana Persano, and Dario Pisignano. **Computational homogenization of fibrous piezoelectric materials**. *Computational Mechanics*, **55**(5):983–998, 2015. 98

[98] Jan G Smits, Susan I Dalke, and Thomas K Cooney. **The constituent equations of piezoelectric bimorphs**. *Sensors and Actuators A: Physical*, **28**(1):41–61, 1991. 98

[99] Ali H Nayfeh, Mohammad I Younis, and Eihab M Abdel-Rahman. **Reduced-order models for MEMS applications**. *Nonlinear dynamics*, **41**(1-3):211–236, 2005. 98

[100] Micha Staworko and Tadeusz Uhl. **Modeling and simulation of piezoelectric elements-comparison of available methods and tools**. *Mechanics/AGH University of Science and Technology*, **27**(4):161–171, 2008. 98

[101] Yaowen Yang and Lihua Tang. **Equivalent circuit modeling of piezoelectric energy harvesters**. *Journal of intelligent material systems and structures*, **20**(18):2223–2235, 2009. 98

[102] Alper Erturk and Daniel J Inman. **An experimentally validated bimorph cantilever model for piezoelectric energy harvesting from base excitations**. *Smart materials and structures*, **18**(2):025009, 2009. 98, 99

[103] Michele Pozzi. **Impulse excitation of piezoelectric bimorphs for energy harvesting: a dimensionless model**. *Smart Materials and Structures*, **23**(4):045044, 2014. 98

[104] M.P.Tarcisio Silva, Marcel Clementino, Alper Erturk, and Carlos Jr De Maqui. **Equivalent electrical circuit framework for nonlinear and high quality factor piezoelectric structures**. *Mechanics*, **54**:133–143, 2018. 98

[105] Klaus-Jürgen Bathe and Sheryl Gracewski. **On nonlinear dynamic analysis using substructuring and mode superposition**. *Computers & Structures*, **13**(5-6):699–707, 1981. 98

[106] Inc. ADINA R&D. **ADINA theory and modeling guide**. *Report ARD 05-6*, 2005. 98

[107] Zu-qing Qu. *Model Order Reduction Techniques with Applications in Finite Element Analysis*. Springer Science & Business Media, 2004. 98

[108] Oliver Weeger, Utz Wever, and Bernd Simeon. **On the use of modal derivatives for nonlinear model order reduction**. *International Journal for Numerical Methods in Engineering*, **108**(13):1579–1602, 2016. 98

[109] Lynn D Gabbay, Jan E Mehner, and Stephen D Senturia. **Computer-aided generation of nonlinear reduced-order dynamic macromodels. I. Non-stress-stiffened case**. *Journal of Microelectromechanical Systems*, **9**(2):262–269, 2000. 98

[110] Jan E Mehner, Lynn D Gabbay, and Stephen D Senturia. **Computer-aided generation of nonlinear reduced-order dynamic macromodels. II. Stress-stiffened case**. *Journal of microelectromechanical systems*, **9**(2):270–278, 2000. 98

[111] ANSYS Mechanical APDL Coupled-Field. **Analysis Guide**. 2010. 98

[112] Alper Erturk and Daniel J Inman. **A distributed parameter electromechanical model for cantilevered piezoelectric energy harvesters**. *Journal of vibration and acoustics*, **130**(4):041002, 2008. 99, 110, 115

[113] Samuel C Stanton, Alper Erturk, Brian P Mann, and Daniel J Inman. **Nonlinear piezoelectricity in electroelastic energy harvesters: Modeling and experimental identification**. *Journal of Applied Physics*, **108**(7):074903, 2010. 99

[114] Claudio Maruccio, Giuseppe Quaranta, Pasquale Montegiglio, Francesco Trentadue, and Giuseppe Acciani. **A Two-Step Hybrid Approach for Modeling the Nonlinear Dynamic Response of Piezoelectric Energy Harvesters**. *Shock and Vibration*, **2018**, 2018. 101, 105

[115] Jiashi Yang. *An introduction to the theory of piezoelectricity*, **9**. Springer Science & Business Media, 2004. 101

[116] Gerd Brandstetter and Sanjay Govindjee. **Cyclic steady states of nonlinear electro-mechanical devices excited at resonance**. *International Journal for Numerical Methods in Engineering*, **110**(13):1227–1246, 2017. 102

[117] Paul Steinmann. **Computational nonlinear electro-elasticitygetting started**. In *Mechanics and electrodynamics of magneto-and electro-elastic materials*, pages 181–230. Springer, 2011. 102

[118] Joze Korlec and Peter Wriggers. *Automation of Finite Element Methods: Basic Equations of Continuum Mechanics*. Springer Science & Business Media, 2016. 102, 103, 105

[119] Richard H Enns and George C McGuire. *Nonlinear physics with Mathematica for scientists and engineers*. Springer Science & Business Media, 2012. 105

[120] Niell G Elvin, Nizar Lajnef, and Alex A Elvin. **Feasibility of structural monitoring with vibration powered sensors**. *Smart materials and structures*, **15**(4):977, 2006. 106

[121] Soon-Duck Kwon. **A T-shaped piezoelectric cantilever for fluid energy harvesting**. *Applied physics letters*, **97**(16):164102, 2010. 106